SLOPES OF THE SEA SURFACE DEDUCED FROM PHOTOGRAPHS OF SUN GLITTER

BY

CHARLES COX AND WALTER MUNK

UNIVERSITY OF CALIFORNIA PRESS
BERKELEY AND LOS ANGELES
1956

BULLETIN OF THE SCRIPPS INSTITUTION OF OCEANOGRAPHY
OF THE UNIVERSITY OF CALIFORNIA
LA JOLLA, CALIFORNIA

EDITORS: CLAUDE E. ZOBELL, ROBERT S. ARTHUR, DENIS L. FOX

Volume 6, No. 9, pp. 401–488, plates 10–12, 27 figures in text
Submitted by editors June 3, 1955
Issued September 25, 1956
Price, $1.75

UNIVERSITY OF CALIFORNIA PRESS
BERKELEY AND LOS ANGELES
CALIFORNIA

CAMBRIDGE UNIVERSITY PRESS
LONDON, ENGLAND

[CONTRIBUTIONS FROM THE SCRIPPS INSTITUTION OF OCEANOGRAPHY, NEW SERIES, NO. 859]

PRINTED IN THE UNITED STATES OF AMERICA

CONTENTS

SLOPES OF THE SEA SURFACE DEDUCED FROM PHOTOGRAPHS OF SUN GLITTER

BY

CHARLES COX AND WALTER MUNK

ABSTRACT

Part I: Experimental Method and Observations.—The distribution of brightness of sun glitter on the sea surface is interpreted in terms of the statistics of the sea-surface slope distribution. The method consists of two phases: (1) identifying, from the law of reflection, any point on the surface with the particular slope required to reflect the sun's rays toward the observer, and (2) interpreting the average brightness of the sea surface in the vicinity of this point in terms of the frequency with which this particular slope occurs. The computation of the probability of large (and infrequent) slopes is limited by the disappearance of the glitter into a background consisting of (1) sunlight scattered from particles beneath the sea surface, and (2) skylight reflected by the sea surface.

The method has been applied to aerial photographs taken near the Hawaiian Islands. Winds were measured from a vessel at the time and place of the aerial photographs, and cover a range from 1 to 14 m. sec.$^{-1}$ The logarithmic distribution of slopes has been tabulated for various wind speeds. A two-dimensional Gram-Charlier series is fitted to the data. As a first approximation the distribution is Gaussian and isotropic. The mean square slope (regardless of direction) increases linearly with the wind speed, reaching a value of $(\tan 16°)^2$ for a wind speed of 14 m. sec.$^{-1}$ The ratio of the crosswind to the up/downwind mean square slope component varies depending on the steadiness of the wind from 1.0 to 0.5. There is some skewness which increases with increasing wind speed. As a result the most probable slope at high winds is not zero but a few degrees, with the azimuth of ascent pointing downwind. The measured peakedness is near the limit of observational error and is such as to make the probability of very large and very small slopes greater than Gaussian. The effect of oil slicks covering an area of one-quarter square mile is to reduce the mean square slopes by a factor of two or three, to eliminate skewness, but to leave peakedness unchanged.

Part II: Interpretation.—An attempt is made to interpret the results given in Part I in terms of models having simple wave spectra. The observed nearly Gaussian distribution of slopes is inconsistent with a spectrum consisting of a few discrete frequencies, but can be accounted for by a continuous spectrum of arbitrary width or a large number of discrete frequencies. The observed skewness may be a nonlinear effect, and is not treated. The observed ratio between cross- and up/downwind slopes can be interpreted in terms of two wave "beams" intersecting at 70°, or a single wide beam subtending 130°. These values apply to the relatively short waves that contribute largely to the slope spectrum. The observed proportionality between mean square slope and wind speed follows from a spectrum proposed by Neumann on the basis of wave-amplitude observations, but yields a constant of proportionality too small by a factor of three. A spectrum proposed by Darbyshire cannot be reconciled with the observed slope distribution.

Measurements of curvature will provide a critical test of the high-frequency end of the spectrum. An extrapolation of the Neumann spectrum into the region of capillary waves predicts an r.m.s. curvature of 0.12 cm.$^{-1}$, independent of wind speed. The observed reduction in mean square slope by a slick may be accounted for by assuming that the slick forms an inextensible surface against which waves (Neumann spectrum) are dissipated by viscosity. Some difficulties of this interpretation are stated. The distribution of surface-particle acceleration is closely related to the distribution of slopes. The total mean square acceleration increases linearly with wind speed and reaches a value of $(0.4\ g.)^2$ at a wind speed of 14 m. sec.$^{-1}$

Part III: Application.—Measurements of the probability distribution of sea-surface slopes have made accessible to numerical treatment problems involving the interaction of short-wave radiation with a *roughened* sea surface. It is found that the refracted sun's glitter (as seen from beneath the surface) is scattered into a smaller solid angle but is about one thousand times more luminous (neglecting absorption) than the reflected glitter, and that, unlike the reflected glitter, it expands and dims as the sun sets. The albedo of a rough surface to direct sunlight is slightly larger at high sun angles, and substantially smaller at low sun angles, than the albedo of a flat surface. Accord-

ingly, more solar energy penetrates waters at high latitudes than had previously been estimated, and the amount of this additional energy depends upon wind speed. The luminosity of the sea surface due to skylight has been computed for various conditions. A rough surface is darker at the horizon than a smooth surface, thus enhancing the horizon contrast. The albedo of the sea surface to skylight varies from 5 to 10 per cent depending on the distribution of illumination from the sky; it is largest when the sea is flat calm. The roughening by a Beaufort 4 wind reduces the albedo by about 20 per cent. Finally, a discussion of the visibility of slicks is given. When illuminated with skylight, natural slicks, of a thickness small compared to a wave length of light, contrast with a clean sea surface most sharply when they are near the horizon. Freshly spread oil slicks, on the other hand, show more contrast directly beneath the observer.

ACKNOWLEDGMENTS

The research reported in this paper was made possible by the financial and material support of the Geophysical Research Directorate of the Air Force Cambridge Research Center. The writers are happy to record the spirit of coöperation of Michael Sbarra, Capt. USAF, and his officers and crew of the Air Force plane, and of Steacy Hicks and Robert Huffer and the crew aboard the *Reverie*. In Monterey, the plane was stationed at the Naval Auxiliary Air Station and the *Reverie* docked at the USCG Life Guard Station. Acknowledgment is due both activities for their friendly coöperation. In Hawaii, Mr. William Nielson, of the Hawaii Aeronautics Commission, was most helpful in arranging facilities for the plane. Here facilities for calibrating and processing the films were quickly set up in an abandoned hangar by Chief W. L. MacDonald, USN, and T/Sgt V. R. Cooke, USAF, who had joined the operation at NAAS, Monterey, and Hickam AF Base, Hawaii, respectively. Measurements of films and calculations of slope probabilities were carried out by Margaret DeSelle and Steacy Hicks.

PART I: EXPERIMENTAL METHOD AND OBSERVATIONS

1. Introduction

The purpose of this study was to make quantitative measurements pertaining to the roughness of the sea surface; in particular, to learn something concerning the distribution of slope at various wind speeds. This distribution plays an important part in the reflection and refraction of acoustic and electromagnetic radiation, and in the complex problem of wind stress on the water surface.

The method consists in photographing from a plane the sun's glitter pattern on the sea surface, and translating the statistics of the glitter into the statistics of the slope distribution. Winds were measured from a vessel at the time and place the photographs were taken. They ranged from 1 to 14 m. sec.$^{-1}$ Abbreviated accounts of this study appear in Cox and Munk (1954 *a*, *b*, and 1955).

If the sea surface were absolutely calm, a single, mirrorlike reflection of the sun would be centered at the *horizontal specular point*. In the usual case there are thousands of "dancing" high lights. At each high light there must be a water facet, possibly quite small, which is so inclined as to reflect an incoming ray from the sun toward the observer. The farther the highlighted facet is from the horizontal specular point, the larger must be this inclination. The width of the glitter pattern is therefore an indication of the maximum slope of the sea surface.

Spooner (1822) in a letter to Baron de Zach reports four measurements by this method in the Tyrrhenian Sea, all yielding maximum slopes of 25°. Hulburt (1934) demonstrates by this method that the maximum slope in the North Atlantic increased from 15° at a 3-knot wind to 25° at an 18-knot wind. Shuleikin (1941) took a long series of measurements over the Black Sea of the width of the "road to happiness" (a Russian synonym for the glitter pattern from the setting sun), and deduced that slopes up to 30° were not uncommon.

These measurements of maximum slope, so widely separated in space and time, are reasonably consistent. They do depend, however, on the manner in which the outer boundary of the glitter pattern is selected. This selection is apparently influenced by the brightness of the light source relative to the sky, and by the sensitivity of the eye. For otherwise the moon's glitter would not appear narrower than the sun's glitter under otherwise identical conditions. This difficulty may be avoided by computing the distribution of slopes from the measured variation of *brightness within the glitter pattern* (rather than computing maximum slopes from the outer boundaries). This method gives more information—and requires much more work.

The two principal phases are: (1) identifying, from geometric considerations, a point on the sea surface (as it appears on the photographs) with the particular slope required at this point for the reflection of sunlight into the camera, and (2) interpreting the average brightness of the sea surface (or darkening of the negative) at this point in terms of the frequency with which this particular slope occurs. By choosing many such points one finds the frequency distribution of slopes.

2. The Observations

The derivation of section **4** will show that the radiance of reflected sunlight from the sea surface is determined by the distribution of slopes, provided the light is reflected only once. To avoid multiple reflections, measurements were made only when the sun was high (only slopes greater than about one-half the angle of sun elevation can cause a second reflection). For a high sun the glitter pattern covers the surface to all sides of a point directly beneath the observer, and aerial observation is indicated.

2.1 *Aerial observations.*—A B-17G airplane was made available from the 3171st Electronics Research and Development Group, Griffiss Air Force Base, Rome, N.Y. Four K-17 (six-inch focal length) aerial cameras were mounted on a frame which could be lowered through the bomb bay and leveled during flight. They were wired for synchronous exposures. Two cameras pointed vertically downward; the other two pointed to port and were inclined downward at an angle of 30° with the horizontal. This allowed for a 25 per cent overlap between the vertical and tilted photographs (see, for example, pls. 10 and 11, 4 Sept. k). One of the vertical cameras and one of the tilted cameras took ordinary in-focus or *image* photographs, using "variable density minus blue" filters. At an altitude of 2,000 feet, two points on the sea surface, separated by more than 40 cm., are resolved on the image photographs. The two remaining cameras were deliberately set out of focus by removing the lens systems. The resulting "photometric" photographs (pl. 12) yield (by measurements of optical density) the sea-surface brightness and form the basis for computations of slope probabilities. In order to reduce unwanted background light, mostly blue

in color, glass sandwich filters containing Wratten gelatin A-25 absorbers were installed on these cameras.

During the photographic runs, the plane was steered by sun compass so that the azimuth of the tilted cameras was toward the sun. An attempt was made to avoid cloud shadows and atmospheric haze. In most cases the field of the cameras was sufficiently restricted to avoid these effects when the plane was flying at an altitude of 2,000 feet.

2.2 *Observations at sea.*—In order to correlate measurements of wind speed with slope distribution free from modifying effects of land, it was necessary to have meteorological records from a vessel near the location of the photographs. For this purpose a 58-foot schooner, the *Reverie*, was chartered and equipped with Bendix Friez Aerovane anemometers on the fore masthead (41 ft.) and bowsprit (10 ft.). At the time the aerial photographs were taken the vessel would heave to with the wind abeam, steadied by the sails. With this arrangement the error inherent in using cup-type anemometers on a rolling vessel was avoided. The output of the masthead anemometer, and the difference, masthead minus bowsprit, were smoothed by an R,C-filter with 18-second time constant, and recorded on two Esterline-Angus milliammeters. Wind direction was estimated by eye. For some of the earlier measurements we also attempted to raise and lower a hand anemometer with the movement of the boat and the waves so as to keep it three feet above the water surface. Other measurements included the air and water temperatures, and the wet and dry bulb temperatures.

One of the objects of this investigation was to study the effect of surface slicks. First an attempt to spray powdered detergent was made from the vessel, and later from the plane, but the slicks thus produced did not persist sufficiently. A satisfactory solution was to pump oil on the water, using a mixture consisting of 40 per cent used crankcase oil, 40 per cent diesel oil, and 20 per cent fish oil. With 200 gallons of this mixture a coherent slick 2,000 feet by 2,000 feet could be laid in 25 minutes, provided the wind did not exceed 20 miles an hour.

2.3 *Location of observations.*—During July, 1951, observations were taken offshore from Monterey, California, where a variety of wind conditions could be expected. Unfortunately the number of clear days was even smaller than that given on climatological charts, and only two successful flights were completed.

By the end of July the sun elevation at noon was approaching the minimum requirement of 55° (to photograph plane's shadow; see sec. **3**), and it was decided to move the plane and vessel to Hawaii. In this area one can select radically different wind conditions by moving short distances. The island of Maui was chosen because the region surrounding this island is the least clouded. Also, the harbor and airport facilities are conveniently near to one another. Conditions were excellent, and all observations were taken during the period 25 August to 25 September, 1951.

3. The Geometry of Reflection

The geometry of reflection has been considered by Minnaert (1942) and Van Wieringen (1947), with special emphasis on circular waves, and also by Hulburt (1934) and by Eckart (1946). Here we shall require a systematic development which

can be readily expanded into the second order calculations of the next section. A slope vector may be defined with the components (fig. 1)

$$z_x = \partial z/\partial x = \sin\alpha \tan\beta, \qquad z_y = \partial z/\partial y = \cos\alpha \tan\beta\,, \tag{3–1}$$

where α is the azimuth of ascent (clockwise from the sun) and β is the tilt. (In geologic literature the attitude of a surface is described by its dip and strike. The former is numerically equal to the inclination β; the latter is measured 90° to the left of the azimuth of ascent α.) Unit vectors **n**, **i**, and **r**, normal to the surface (positive

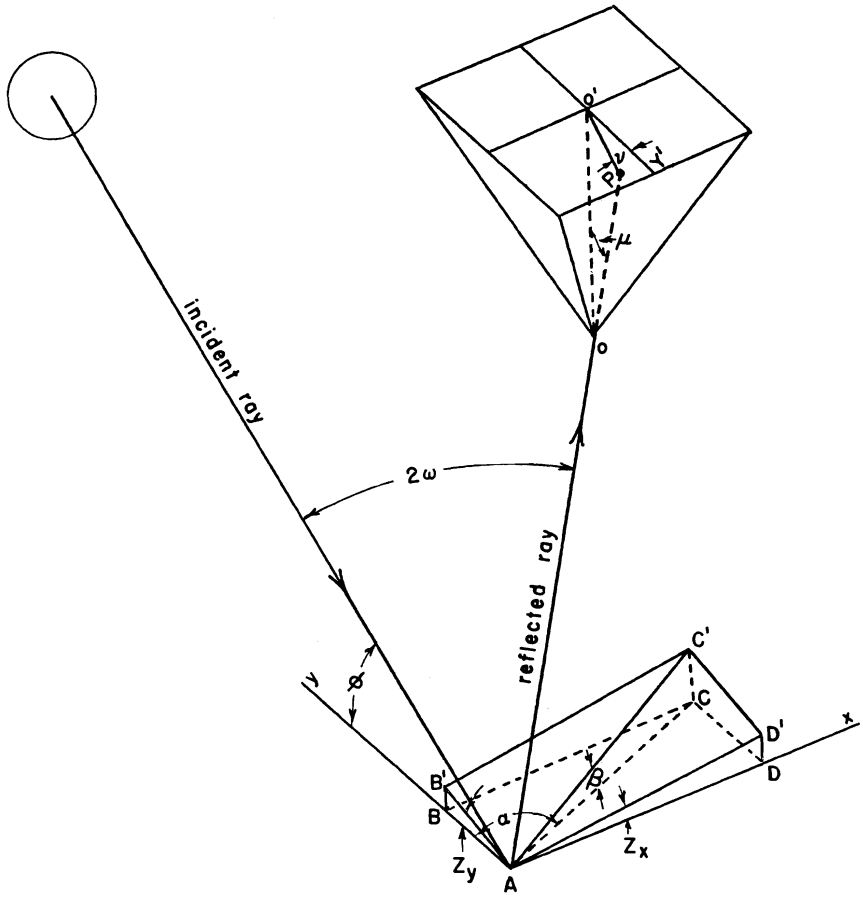

Fig. 1. The coördinate system is centered at the sea surface, with the z-axis vertically upward (not shown) and the y-axis drawn horizontally toward the sun. The incident ray is reflected at A and forms an image at P on a horizontal photographic plate. Points $A\ B\ C\ D$ define a horizontal plane through A and $A\ B'\ C'\ D'$, the plane tangent to the sea surface. The tilt, β, is measured in the direction AC of steepest ascent, and this direction makes an angle α clockwise from the sun. OO' is parallel to the z-axis and $O'Y'$ to the (negative) y-axis.

upward), along the incident ray, and along the reflected ray, respectively, have the components

$$\left.\begin{aligned} \mathbf{n} &= (-\sin\alpha\sin\beta, \quad -\cos\alpha\sin\beta, \quad \cos\beta)\,, \\ \mathbf{i} &= (\ 0, \qquad\qquad -\cos\phi, \qquad -\sin\phi)\,, \\ \mathbf{r} &= (-\sin\nu\sin\mu, \quad -\cos\nu\sin\mu, \quad \cos\mu)\,. \end{aligned}\right\} \tag{3-2}$$

According to the law of reflection, the vector difference between unit vectors along the reflected and incident rays must lie along the surface normal; thus

$$\mathbf{r} - \mathbf{i} = (2\cos\omega)\mathbf{n}\,, \tag{3-3}$$

where $2\cos\omega$ is the proportionality constant. Comparing the dot product of (3–3) with $\mathbf{r}$ and $\mathbf{i}$, respectively, yields

$$\mathbf{n}\cdot\mathbf{r} = -\mathbf{n}\cdot\mathbf{i} = \cos\omega = \cos\beta\sin\phi - \cos\alpha\sin\beta\cos\phi\,. \tag{3-4}$$

Clearly ω is the angle of incidence or reflection (fig. 1). Combining (3–2) and (3–3) yields the grid relations

$$\left.\begin{aligned} \cos\mu &= 2\cos\beta\cos\omega - \sin\phi\,, \\ \cot\nu &= \cot\alpha - \tfrac{1}{2}\csc\alpha\csc\beta\sec\omega\cos\phi\,. \end{aligned}\right\} \tag{3-5}$$

In terms of other parameters the grid relations can become surprisingly complicated. In fact, Shuleikin (1941) considered the computation of such grids as "incommodious" and constructed them experimentally by projecting onto a screen the rays from an artificial "sun" reflected from a mirror of appropriate slope.

For any chosen orientation of the camera the angles μ, ν can be readily converted to film coördinates, and lines of constant α and β constructed (see pls. 10–12). The grids are independent of the height of the camera, but depend on the solar elevation ϕ. The effect of the setting sun is to concentrate the pattern along a narrow street (pl. 10).

3.1 *Correction for roll, pitch, and yaw.*—All photographs have been corrected for the roll (left wing down), pitch (nose down), and yaw (turn to port) of the plane. With some care in flying, these angles can all be kept to within a few degrees. The correction then consists of a translation of the grid so that the horizontal specular point on the grid coincides with that on the photograph, and of a rotation so that the line $\alpha = 0$ points toward the sun. The translation and rotation are uniquely determined from the positions on the photographs of the plane's shadow (clearest on pl. 12, upper right) and of the horizon, allowance having been made for the depression of the horizon due to the earth's curvature.

The following discussion applies to a nominally vertical camera and a tilted camera nominally inclined 30° from the horizontal and pointed to port. The small angles (in radians), roll, pitch, and yaw, can be determined from the coördinates

m^s, n^s of the plane's shadow on the vertical photograph, together with the mean horizon n^h, and the difference Δn^h of the horizon at the right edge minus the horizon at the left edge measured on the tilted photograph. These coördinates are measured with respect to fiducial marks fixed to the cameras (arrow-shaped images barely visible on pls. 10–12); m is positive in the direction of flight, n is positive at right angles to port.

Let the camera focal length be f. Then the desired relations are

$$\left.\begin{aligned} f \cdot \text{roll} &= \frac{3}{4} n^h - \frac{1}{4}\sqrt{3}\, f + .009\, f\sqrt{\frac{h}{1000}} \\ &= n^s \sin^2\phi + f \sin\phi \cos\phi \\ f \cdot \text{pitch} &= \frac{1}{4}\sqrt{3}\, f\, \Delta n^h / m_o \\ f \cdot \text{yaw} &= (f \cdot \text{pitch} - m^s) \tan\phi \end{aligned}\right\} \qquad \textbf{(3.1–1)}$$

where the expression $.009\, f\sqrt{h/1000}$ allows for the depression of the horizon due to the earth's curvature when flying at an elevation of h feet (note grid horizons above actual horizons on pl. 10), and where m_o is the total width of the photograph.

To a first order we may correct for these terms by displacing the vertical grid by m_v, n_v, and the tilted grid by m_t, n_t, where

$$\left.\begin{aligned} m_v &= f \cdot \text{pitch}\,, & m_t &= \tfrac{1}{2} f \cdot \text{pitch} + \tfrac{1}{2}\sqrt{3} \cdot \text{yaw}, \\ n_v &= f \cdot \text{roll} \cdot \csc^2\phi\,, & n_t &= f \cdot \text{roll} \cdot \sec^2(\phi - 30^\circ), \end{aligned}\right\} \qquad \textbf{(3.1–2)}$$

so that the horizontal specular point on the grid coincides with that on the photograph; and by rotating the grids clockwise through the angles

$$\chi_v = \text{yaw}\,, \qquad \chi_t = \tfrac{1}{2}\,\text{yaw} - \tfrac{1}{2}\sqrt{3}\,\text{pitch}\,, \qquad \textbf{(3.1–3)}$$

so that $\alpha = 0$ on the grids point toward the sun.

A further correction may have to be made if the photograph is not taken for the exact value of ϕ for which the grids were drawn (5°, 10°, 15°, · · ·, 90°), but exceeds these by $\delta\phi$. This is done by writing: "roll $- \delta\phi$" for "roll" in (**3.1**–2).

These corrections have been made in placing the grids on the photographs shown in the plates.

4. Surface Radiance

Up to now the ordinary "in focus," or image, photographs have been considered. These photographs show the presence of whitecaps, slicks, and cloud shadows. They also provide the basis for correcting for the roll, pitch, and yaw of the plane. Simultaneously with the tilted and vertical image photographs, and covering the identical fields of view, the sea surface was photographed with two additional cameras

from which lenses had been removed. (Compare pl. 11, upper right, with pl. 12, upper left.) The resulting out-of-focus photographs, or *photometric photographs*, provide the basis for computing frequency distributions of slope.

At the horizontal specular point the sea surface is apt to be so bright as to be blinding to the eye, whereas at some distance from this point the surface is much darker. The principal reason for this variation is that the gentle slopes (which are required for high lights near the horizontal specular point) occur more frequently than the steep slopes. On the *photometric photographs* the glitter pattern appears, therefore, as a round blob with a bright core (on the positive print) and gradually diminishing intensity to the outside. The density of the blob (on the negative) is then measured with a densitometer at points corresponding to the intersection of appropriate grid lines.

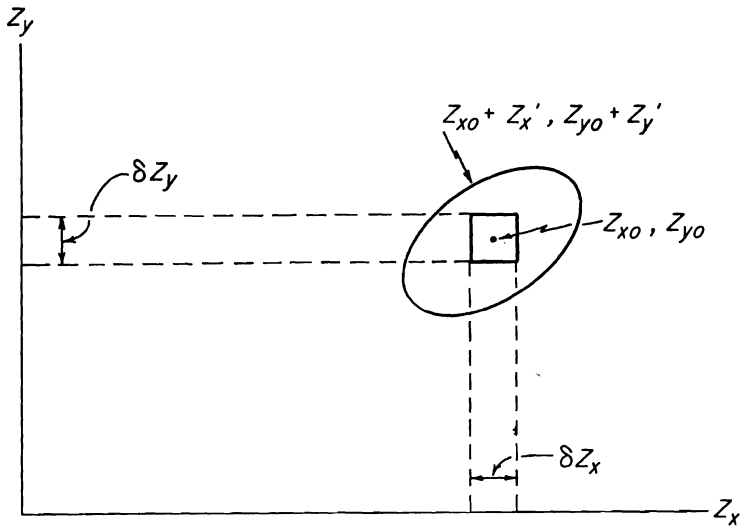

Fig. 2. The tolerance ellipse.

But there are other factors, in addition to the slope distribution, which help determine the density of the photograph. These are (1) the tolerance of slopes for the occurrence of a high light at a fixed point, as related to the finite size of the sun; (2) the dependence of the coefficient of reflectivity of the water surface on the angle of incidence; (3) the ratio of sea-surface area to the corresponding area on the photograph, for different points on the photograph; (4) the variable sensitivity of the camera to light from various directions; and (5) the dependence of the film density on the exposure. These factors will now be considered.

4.1 *The tolerance ellipse.*—Let the point z_{xo},z_{yo} on a z_x,z_y-diagram (fig. 2) represent the required slope at x_o,y_o on the sea surface in order that a light beam from the sun's center striking this point be reflected into the camera. For x_o,y_o to be a high light for a point source of light on the sun's periphery, the values z_{xo} and z_{yo} must vary by small quantities z_x' and z_y'. As the light source moves about the sun's periphery, it will trace an ellipse centered at z_{xo},z_{yo} on the z_x,z_y-diagram. This ellipse defines a tolerance in possible values of z_x,z_y for a high light at x_o,y_o.

The tolerance of slopes is found rather simply for a reflecting facet of zero nominal tilt. Equation (3–2) for a ray from the center of the sun reduces to

$$\left.\begin{aligned} \mathbf{n}_o &= (0, \quad 0, \quad 1), \\ \mathbf{i}_o &= (0, \quad -\sin\omega_o, \quad -\cos\omega_o), \\ \mathbf{r}_o &= (0, \quad -\sin\omega_o, \quad \cos\omega_o), \end{aligned}\right\} \tag{4.1–1}$$

for this special case. Next consider a ray from any other point of the sun. It will be reflected from such a point of the highlighted area that the reflected ray will be sensibly parallel to $\mathbf{r}_o$. The parallelism follows because the angular size of a high light as seen by an aerial observer is negligibly small compared with the angular size of the sun. The unit vectors appropriate for this off-axis reflection are, to the first order of small quantities,

$$\left.\begin{aligned} \mathbf{n}' &= (-z_x', \quad -z_y', \quad 1), \\ \mathbf{i}' &= (\theta', \quad -\sin\omega_o - \omega'\cos\omega_o, \quad -\cos\omega_o + \omega'\sin\omega_o), \\ \mathbf{r}' &= \mathbf{r}_o, \end{aligned}\right\} \tag{4.1–2}$$

where θ', ω' are (small) angular components of the origin of the ray relative to the center of the sun (fig. 3), and z_x', z_y' are (small) slope components of the sea surface

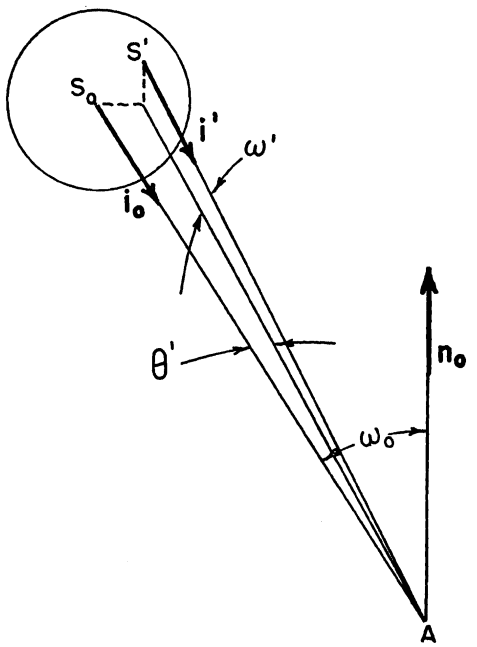

Fig. 3. A horizontal high light is centered at A, with surface normal $\mathbf{n}_o$. S_o is the center and S' an arbitrary point on the sun. Angular component ω' is measured in the vertical plane including S' and $\mathbf{n}_o$, and θ' is measured normal to the vertical plane.

at the place of reflection. From the law of reflection, (**3**–3), one finds

$$\mathbf{r}' - \mathbf{i}' = 2[\cos\omega_o + \delta(\cos\omega)]\,\mathbf{n}',$$

where $\delta(\cos\omega)$ is the (small) change in the constant of proportionality. Neglecting products of small quantities this yields

$$z_x' = (2\cos\omega_o)^{-1}\,\theta', \quad z_y' = -\tfrac{1}{2}\omega'. \tag{**4.1**–3}$$

The area of the tolerance ellipse is $\Delta_t = \int\int dz_x'\,dz_y'$, the integral being taken over all slopes which can reflect the sun. Substituting from (**4.1**–3) this becomes

$$\Delta_t = \tfrac{1}{4}\sec\omega_o \iint_{sun} d\theta'\,d\omega' = \tfrac{1}{4}\pi\epsilon^2\sec\omega_o\,, \tag{**4.1**–4}$$

where $\epsilon = 16.0'$ is the angular radius of the sun.

Equation (**4.1**–4) represents the tolerance of slopes for a horizontal facet or, equally well, for a tilted facet if one measures the slope components z_x', z_y' with respect to a tilted coördinate system (x', y' plane tangent to facet). To find the tolerance area with respect to an *untilted* system (x,y plane horizontal) one derives the relation between slope components in a tilted and horizontal system of coördinates:

$$dz_x\,dz_y = \frac{\partial(z_x,z_y)}{\partial(z_x',z_y')}\,dz_x'\,dz_y'\,,$$

where $\dfrac{\partial(z_x,z_y)}{\partial(z_x',z_y')} = \sec^3\beta_o$ is the Jacobian of the transformation to the first order and β_o is the tilt at the center of the high light. Consequently

$$\Delta_t = \tfrac{1}{4}\pi\epsilon^2\sec^3\beta_o\sec\omega_o \tag{**4.1**–5}$$

is the general formula for the area of the tolerance ellipse.

4.2 *The scattering cross section.*—The tolerance ellipse relates the likelihood of the occurrence of a certain slope to the likelihood, P, for a high light to occur, in a certain area. Suppose we wish to find $p(z_{xo},z_{yo})\delta z_x\delta z_y$, the chance that the slopes fall in the interval $z_{xo} \pm \tfrac{1}{2}\delta z_x, z_y \pm \tfrac{1}{2}\delta z_y$ (fig. 2; see sec. **4.1**). Here p is the *probability distribution* function. The likelihood of slopes occurring within the tolerance ellipse of area $\Delta_t(z_{xo},z_{yo})$ centered at z_{xo},z_{yo} may be found by integrating p over the tolerance ellipse. But since Δ_t is very small, the relation becomes

$$P(z_{xo},z_{yo}) = p(z_{xo},z_{yo})\,\Delta_t(z_{xo},z_{yo}) \tag{**4.2**–1}$$

to a good approximation. Thus if P can be measured, p can be readily computed.

The determination of P is a matter of some difficulty. One method would consist of recording the fraction of time, P, during which x_o,y_o is a high light, but this is difficult to accomplish from a plane. A measurement that comes closer to being

feasible is the determination of the fraction of horizontal area in the immediate vicinity of x_o,y_o that is highlighted during a very brief interval. This fraction is again equal to P, provided that in this vicinity all points have equal a priori probabilities of attaining a given slope. This provision excludes the edge of slicks, or regions where winds change rapidly. Of course one finds only a "sample estimate" of the probability because the "vicinity" is of limited area. The sample estimate becomes practically indistinguishable from the true probability, provided the observer is sufficiently high that the "vicinity" of x_o,y_o includes an area larger in linear dimensions than the wave length of the longest ocean swell present. Consequently the term "probability" will be used in the following discussion even though only the sample estimate of probability is measured.

Yet not even the fractional area that is highlighted can be measured directly from the photographs. In the first place, the individual glitters are too small to be resolved on the aerial photographs; what appears as an isolated high light is actually a cluster of several hundred tiny glitters, each perhaps a fraction of a millimeter in diameter. In the second place, the photographic image of a cluster is, because of its high intensity, many times larger than the image that would be obtained with a perfect optical system.

However, by means of the out-of-focus, or density, photographs we can determine the *average* radiance over an area which includes many clusters of high lights. But the required quantity is the fractional area that is highlighted. Fortunately, the radiance and the fractional area are proportional, and the latter can be computed from the former.

Let Δ_h designate the area of a single high light projected onto a horizontal plane; then $\Delta_h \sec \beta$ will be the actual area on the (sloping) sea surface, and $\Delta_h \sec \beta \cos \omega$ the projection onto a plane normal to the incident rays. Let δH be the irradiance at the sea surface from a small surface element on the sun. The incident flux upon the high light from this element is $\delta H \Delta_h \sec \beta \cos \omega$. The reflected flux is

$$\rho(\omega)\delta H\ \Delta_h \sec \beta \cos \omega,$$

where ρ is the reflection coefficient; it is radiated into a solid angle $\pi\epsilon^2$, the solid angle subtended by the sun. This result follows by reciprocity, as we have already shown that a bundle of parallel rays from the camera to the periphery of the high light will be reflected around the periphery of the sun. Hence the intensity of the reflected beam (in power per unit solid angle) equals $\Delta_h\rho\ (\delta H/\pi\epsilon^2) \sec \beta \cos \omega$. Since the camera aperture lies within the solid angle $\pi\epsilon^2$ regardless of the location of the element on the sun's surface, we can sum surface elements and replace δH by H, so that

$$J = \Delta_h \sec \beta\ \rho(\omega) \frac{H}{\pi\epsilon^2} \cos \omega \qquad (4.2\text{–}2)$$

is the reflected radiant intensity from *one* high light. This result follows also from the general theorem that the incident and reflected powers per unit area per unit solid angle are equal for a perfect reflector. From a horizontal unit area of sea surface containing many such high lights and yet sufficiently small so that α, β can be con-

sidered constant from high light to high light, the reflected radiant intensity is

$$N \cos \mu = P J , \qquad (\mathbf{4.2}\text{–}3)$$

since P represents the fraction of surface that is highlighted under the assumption previously stated. Combining (**4.1**–5) and (**4.2**–1, –2, –3) yields the desired relation

$$p = \frac{4}{\rho} \cos^4 \beta \frac{N}{H} \cos \mu . \qquad (\mathbf{4.2}\text{–}4)$$

The quantity N is the radiance of the sea surface in the line of sight, and the ratio $(N \cos \mu)/H$ has been called by Eckart the "scattering cross section for unit solid angle per unit area of sea surface." Eckart (1953) has calculated this quantity (with some approximations) for the scattering of sound waves of length not necessarily short compared to the height of sea-surface roughness elements. For the limiting case of short-wave radiation he obtains essentially $p = 4(N \cos \mu)/H$.

4.3 *The reflection coefficient.*—The reflection coefficient $\rho(\omega)$ for unpolarized light at a dielectric interface is given by Fresnel's formula

$$2\rho(\omega) = \sin^2(\omega - \omega_r) \csc^2 (\omega + \omega_r) + \tan^2 (\omega - \omega_r) \cot^2 (\omega + \omega_r) \qquad (\mathbf{4.3}\text{–}1)$$

where ω_r is defined by $\sin \omega = n \sin \omega_r$ and n is the ratio of indexes of refraction across the interface. For uncontaminated sea water $n = 1.338$, yielding $\rho(\omega) =$ .020, .021, .060, and 1.00 for $\omega = 0°$, 30°, 60°, and 90°.

In the presence of slicks (pl. 12) these values have to be somewhat modified. The artificial slicks laid by the boat consisted of a mixture of crankcase oil, sardine oil, and kerosene. For orientation, we consider monodecane with the refractive index 1.42. The reflection at normal incidence is $\rho(0) = (n - 1)^2/(n + 1)^2$. This gives $\rho_1(0) = .030$ for air-monodecane, and $\rho_2(0) = .001$ for the monodecane-water interface.

It is found that the thickness of the artificial slicks was of the order of several wave lengths of light, and about a thousand times the thickness of a monomolecular layer. Assuming that both faces of the oil layer reflect light according to Fresnel's law, the complete reflection coefficient (taking into account multiple reflections but disregarding interference effects) equals $\rho_1 + \rho_2(1 - \rho_1)^2(1 - \rho_1\rho_2)^{-1}$ for normal incidence. This gives .031 for monodecane, as compared to .020 for an uncontaminated water surface. The computed increase in reflectivity is in general agreement with the observed increase over artificial slicks.

Natural slicks are probably much thinner, perhaps only a few molecules thick. (Preliminary measurements by Kittredge indicate monomolecular slicks.) The effect on the reflection of light should then be negligible, and (**4.3**–1) should apply, with $n = 1.338$. This has been confirmed by photometric measurements at normal incidence.

4.4 *Photographic photometry.*—The remaining problem is to relate the sea-surface radiance N to the film density D. There are some difficulties in the use of aerial cameras for sensitometry.

The photometric cameras had apertures of 1.7 cm. A point source (or any high light) at a large distance from the camera then has a nearly circular image with a diameter of about 1.7 cm. This size fulfills the following conditions: (1) it is large compared to the average distance between high lights, so that the high lights blend into one another and the grayness of the negative is not too spotty; (2) it is large compared to the size of the measuring aperture of the densitometer; (3) it is sufficiently small that the computed probability distribution of slopes is not appreciably "smeared out."

Suppose s is the distance from the highlighted area (OA in fig. 1; see sec. **3**), d is the diameter of the aperture, and λ the angle between the principal axis of the camera and the reflected ray ($\lambda = \mu$ for an exactly vertical camera [fig. 1]). The solid angle subtended by the aperture is $\frac{1}{4}\pi d^2 s^{-2} \cos\lambda$. Then since $N \cos\mu$ is the flux of radiation from a unit sea surface into a unit solid angle,

$$\tfrac{1}{4}\pi d^2 s^{-2} \tau(\lambda)\ (\cos\lambda) N \cos\mu$$

is the corresponding flux into the photosensitive emulsion.

The transmission $\tau(\lambda)$ allows for (1) the reflection of the incoming rays by the outer face of a filter and (2) by the inner face; (3) absorption of flux in the filter; (4) reflection by the gelatin on the photographic plate; and (5) the vignetting effect resulting from the finite width of the aperture. The index of refraction of glass and the gelatin is 1.52, and hence each of the effects (1), (2), and (4) is proportional to $1 - \rho(\lambda)$ where $\rho(\lambda)$ is Fresnel reflectivity. Altogether the intensity is therefore reduced by a factor $[1 - \rho(\lambda)]^3$.

The absorption of energy by the red filter consists first of a constant term involving the absorption of solar power for wave lengths less than 580 mμ. Of the energy in the band 580 mμ to 660 mμ, 20 per cent is absorbed for rays at normal incidence and 24 per cent for rays traveling obliquely through the filter to the corner of the photograph. Wave lengths greater than 660 mμ are unimportant since the film is not sensitive to them.

The vignetting effect was computed from the dimensions of the aperture. The computation was checked by measuring the deviation from a circle of an image formed by a point source. All these effects combined result in a ratio $\tau(45°)/\tau(0°) = 0.81$ between the transmission at the extreme corner of the photograph and that at the center.

The product of flux and exposure time gives the luminescent energy reaching a unit film area during the entire exposure from a unit area of sea surface. Altogether this unit area of film receives energy from Δ_u unit areas of sea surface, amounting to

$$E = \tfrac{1}{4} t \Delta_u \pi d^2 s^{-2} \tau(\lambda)\, N \cos\lambda \cos\mu \qquad (\mathbf{4.4}\text{–}1)$$

units of luminescent energy in an exposure of duration t. It can be shown that $\Delta_u = s^2 f^{-2} \cos^3\lambda \sec\mu$, where f is focal length, and therefore

$$N = C\tau^{-1} E(D) \sec^4\lambda\,, \qquad (\mathbf{4.4}\text{–}2)$$

where $C = 4f^2/(\pi d^2 t)$.

The photometric photographs were placed over the appropriate grids (translated and rotated to allow for roll, pitch, and yaw), and the intersections for every ten degrees of α and five degrees of β marked on the films. Additional intersections were marked for low winds and slick sea surface. The density D at each marked position was measured by a Welch "Densichron." The reproducibility of these measurements was $\pm.02$ in density.

Additional measurements of density were made on each set of photometric photographs at corresponding points of the overlapping regions between the tilted and vertical films. Comparison of these pairs of densities was the basis for adjusting the calibrations for tilted and vertical films to common (but still arbitrary) units.

The exposure $E(D)$ was determined from the density D of the film by comparison with the density produced by a light of known intensity. Because of the failure of the reciprocity law, the calibration exposure had to be the same as the exposure on the flights. The calibration light source consisted of a concave diffusing surface (from a Federal 4″ x 5″ cold light enlarger) illuminated by thirty-nine incandescent bulbs arranged in a ring within the periphery of the diffusing surface. The calibrating light was passed through a Wratten A-25 filter in order to restrict the wavelength range to that of the photometric photographs. (Sunlight reflected from white blotting paper gave similar results.) Before falling on the photographic films the light source was intercepted by an optical wedge (a modified Eastman Kodak projection print scale) with eleven steps of differing transmission ranging from 100 to 3.7 per cent. Because the densitometer did not give a sufficiently accurate measure of diffuse transmittivity, the transmission of each step of this wedge had been measured by the following absolute method: A surface of uniform brightness illuminated successively seven graded apertures through a Wratten A-25 filter. At a distance great compared to the diameter of the largest aperture, the luminescent energy per unit area from each was then proportional to the area of the aperture. This light exposed successive regions on a strip of super XX aero film through the optical wedge. The exposure times were held constant. After uniform development of the strip, the densities of the seventy-seven step images were measured with a Welch "Densichron" capable of readings reproducible within .01 in density. A plot of the "Densichron" density of the successive images of one particular step in the optical wedge was made against the log of aperture area. Corresponding curves were drawn for the other steps of the optical wedge. The eleven curves were similar, and displaced relative to one another along the log-area axis. The antilog of the displacement between two such curves is the ratio of the transmission of the two steps in the optical wedge. Since the absolute transmission of one step was known to be 100 per cent, the absolute transmission of all steps became known.

The range of light intensities (100 to 3.7) from a single calibration was extended by making several exposures with differing voltages on the incandescent lamps. Curves of D versus log E were drawn for each exposure and fitted together by comparison of the overlapping range of densities. In this way a calibration range of light intensities of 1,000 to 1 was obtained.

Calibrations were made before and after each flight. The roll film (super XX with 9″ x 9″ negatives) was developed in motor-driven tanks using D-76 developer. On a roll containing only calibration exposures it was found that the slopes, γ, of the

D-log E curves varied by less than 3 per cent except for exposures within 12 feet of the end of the roll. Consequently, leaders of this length were left on the ends of all photometric photograph rolls. Sets of calibration exposures were made at the beginning and end of each roll and at intervals within the roll so that there were never more than fifteen photometric photographs between calibrations. Because of various malfunctions of the developing machines, the various calibrations on one roll gave values of γ varying by as much as 10 per cent. The development of the photometric photographs was carried out to a γ of about 0.8. With this development the film was able to register light whose intensity varied over a range of more than 1,000 to 1.

4.5 *Relationship between probability and film densities.*—Equation (**4.2**–4) expresses the slope probability p as a function of surface radiance N, and (**4.4**–2) relates N to the film density D. These are the desired relationships. For the special case of the sun overhead and the camera *exactly* vertical, $\phi = 90°$, $\mu = \lambda = 2\beta$, and $p \sim \cos^4 \beta \sec^3 \mu E$, or $p \sim (1 + \mu^2 + \cdots) E$ for the probability distribution of small slopes. This linear relation (to a first order) between probability and exposure indicates the inherent soundness of the present method.

5. Background Radiation

In addition to the reflection of the sun's rays from the sea surface, there are two other distinct sources of radiation: (1) the skylight reflected at the sea surface, and (2) the sunlight scattered by particles beneath the sea surface. These provide the "background" against which the sun's glitter is measured.

On calm days, the scattered sunlight and reflected skylight are of roughly equal intensity directly beneath the plane. In this region it is difficult to recognize the configuration of the sea surface outside the glitter pattern for two reasons: (1) the scattered light is nearly independent of the presence of waves; and (2) the sky reflection shows little contrast on different sides of waves because the reflected parts of the sky dome are about equally bright and the coefficient of reflection varies little from that for normal incidence. The skylight predominates at greater distances. One qualitative indication of the scattered sunlight is the existence of the plane's shadow outside the limits of the glitter pattern (pl. 12, upper right, within white cross).

Rough estimates can be made of the skylight (see sec. **19**). On the basis of this and a comparison with the observed background radiation on a calm day, an estimate of the scattered sunlight is found. Fortunately, the ratio of signal to background can be made fairly large by the use of a red filter, because sunlight is white and the skylight and scattered light are blue. Near the horizontal specular point the ratio varies from 500:1 on a smooth sea to 15:1 on a very rough sea. But in computing the probability of the large (and infrequent) slopes, an essential limitation is imposed by the disappearance of the glitter radiation into the background of the reflected skylight and scattered sunlight.

5.1 *Reflected skylight.*—It may be shown (sec. **19**), on the assumption that light has exactly one reflection at the sea surface, that the radiance of the sea surface due to reflected skylight is

$$N' = \sec \mu \iint N_s \, \rho(\omega) \cos \omega \sec \beta \, \rho(z_x, z_y) \, dz_x \, dz_y \, ,$$

the limits of integration being such that all visible slopes are included. Here N_s is the radiance of that part of the sky reflected in an element of sea surface inclined with the components z_x, z_y.

The procedure for evaluating the integral is as follows: We anticipate (sec. **11**) that to a first order slopes are normally distributed and independent of wind direction according to $p = (\pi\sigma^2)^{-1} \exp [-(z_x^2 + z_y^2)/\sigma^2]$ where σ is the r.m.s. slope regardless of direction. As a rough approximation the sky dome is assumed uniform,

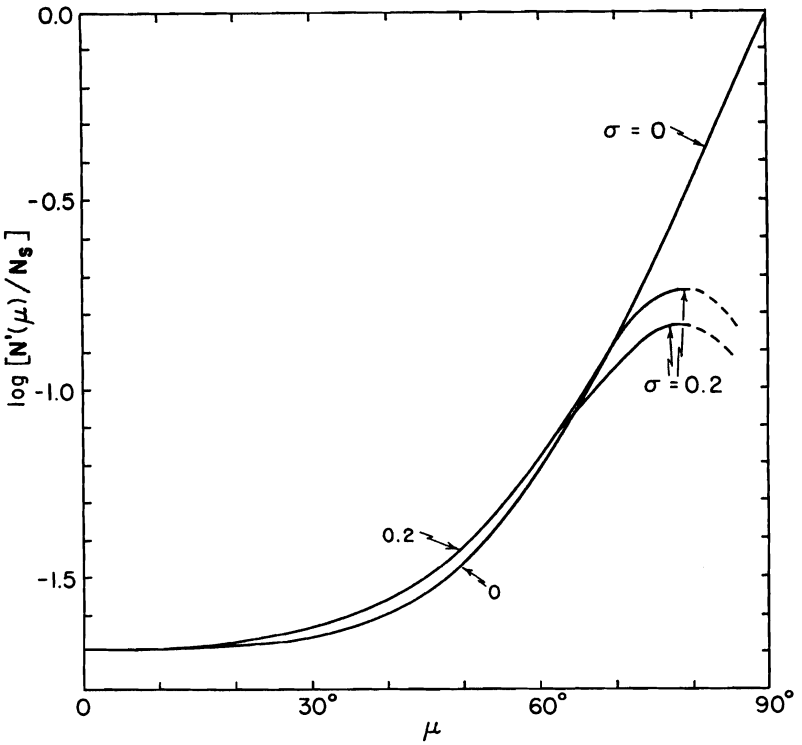

Fig. 4. The radiance (in arbitrary units) of a smooth sea surface ($\sigma = 0$) and a rough sea surface ($\sigma = 0.2$), according to (**18**–10) as described in section **19**. The two branches of the latter curve for large μ correspond to two extreme assumptions regarding multiple reflections.

i.e., N_s = constant. The resulting variation of sea-surface radiance, with viewing angle, is shown in figure 4 for two values of the r.m.s. slope. The upper branch of the curve $\sigma = 0.2$ is the one corresponding to the calculation thus far. Because some of the radiation from the region near the horizon will have been weakened by multiple reflections, this curve represents an upper limit to the skylight. The lower branch of the curve shows the radiation to be expected if none of the multiply reflected rays were to be received. The true radiance is expected to lie between the two branches.

In figures 5 and 6 curves of $N' \cos \mu$ are plotted against some experimental valsue for a calm and a moderately rough sea, respectively. On the calm day the reflected skylight can account for only slightly more than half of the background intensity near $\mu = 0$.

5.2 *The scattered sunlight.*—The above discrepancy is assumed to be due to scat-

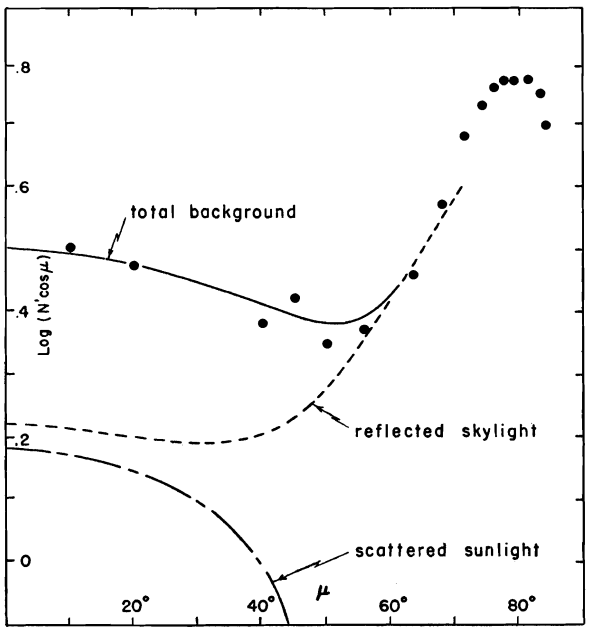

Fig. 5. The solid circles show the measured background on a very calm day (3 Sept. j, σ = .091; see pl. 11, upper left) when the glitter pattern was confined to a small portion of the photograph. This background is due partly to reflected skylight, partly to scattered sunlight, as shown.

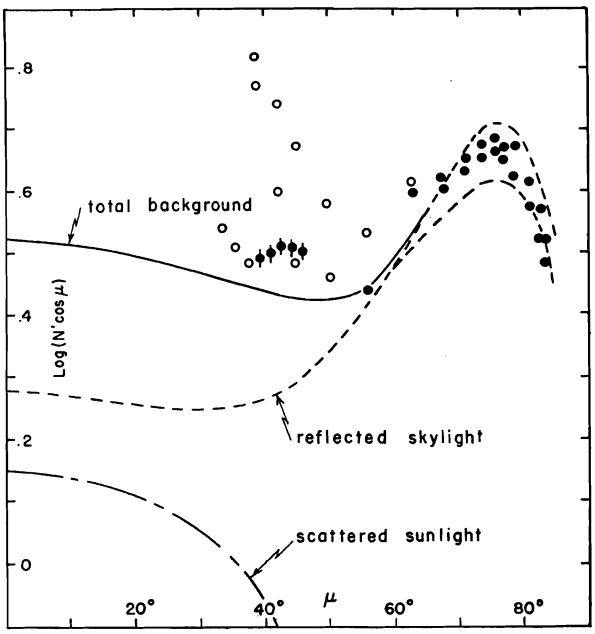

Fig. 6. The background radiation in arbitrary units on a moderately rough day (4 Sept. k, σ = .13; see pl. 10, upper left; 11, upper right). The solid circles correspond to measurements outside the glitter pattern. The open circles contain some glitter radiation and lie, therefore, above the background curve. Circles with the vertical line correspond to measurements on the vertical photograph, the other circles to measurements on tilted photograph.

tered light from within the water. Qualitative evidence for the importance of scattered sunlight is given by the appearance of the plane's shadow outside the glitter. Within the shadow the background radiance is reduced because of the absence of back-scattered light, whereas the reflected skylight is not appreciably diminished.

An empirical relationship for the scattered sunlight as a function of μ was obtained by subtracting from the total measured background that amount due to the reflected skylight (fig. 5). Two particular photographs (3 Sept. j, pl. 11, upper left; 4 Sept. e, pl. 12, upper right) were chosen because the glitter was the smallest on record, and there was adequate space on the photographs to measure the background outside the glitter. It is found that the scattered sunlight is strongest directly beneath the plane ($\mu = 0$), and decreases with increasing μ more rapidly than $\cos \mu$ but less rapidly than $\cos^2 \mu$. A comparison of the photographs for 3 Sept. j and 4 Sept. e shows that the scattered sunlight is proportional to irradiance of the sun, as might be expected.

5.3 *Correction for background.*—In the following procedure for allowing for skylight and scattered sunlight it will be assumed that the empirical law for the scattered sunlight is independent of the roughness of the sea surface, but depends only on the irradiance from the sun, H. Measurements of the glitter (uncorrected for skylight) are used to determine σ and H to a first approximation. Using this value of H, the curve for the scattered sunlight is drawn (fig. 6). Then measurements on the tilted photograph of skylight intensity from regions outside the glitter (fig. 6, solid circles) are used to fix the sky intensity. By means of the curves of figure 4, sky reflection is extrapolated to $\mu = 0$ using the appropriate value of σ. The curves for scattered sunlight and reflected skylight are then combined to give the total background as function of μ. Finally, this background radiance is subtracted from the observed radiance to yield the radiance due to reflected sunlight alone.

On photographs taken at high wind speeds, the glitter pattern covers the entire field of view of both tilted and vertical cameras. Intensities from regions where the glitter reflection is weak give a basis for finding an upper limit to the background light. In all cases it has been found that the upper limit of the ratio of total background intensity to sun intensity varies by less than 30 per cent. The indication then is that the upper limit of the background is not far in excess of the real background.

6. Statistics of Slope Distribution

The log of the unnormalized probability (corrected for background) at the various α,β-grid intersections has been tabulated for each set of photographs. A typical set of measurements—not the best—is shown in figure 10 (sec. **8.1**) and will be used as an example in the following discussion.

Rather than presenting tabulated values, it is more compact to present the results in analytical form as a function of wind speed, and thus bring out the essential physical content. In this way the experimental error is also subdued. A reasonable approach is to make use of the fact that the distribution is close to Gaussian. By representing the data as a Gram-Charlier series, we can develop the deviation from the normal distribution in a systematic manner. These deviations represent skewness and peakedness and therefore have a simple physical interpretation.

6.1 *Gaussian distribution.*—A possible distribution for the two variables z_x,z_y is

$$p_o = M \exp \{ -\tfrac{1}{2}[a_{xx}(z_x - \bar{z}_x)^2 + a_{xy}(z_x - \bar{z}_x)(z_y - \bar{z}_y) + a_{yy}(z_y - \bar{z}_y)^2] \}, \qquad (6.1\text{–}1)$$

where $\bar{z}_x,\bar{z}_y$ are the mean values of z_x and z_y respectively, and M is the constant of normalization. The requirement for a Gaussian distribution is that $a_{xy}^2 \leqq 4a_{xx}a_{yy}$. From various studies it is known that over an area whose linear dimensions are much greater than the longest ocean wave length, the mean slope is of order 10^{-5} or less. Thus $\bar{z}_x = \bar{z}_y = 0$ with negligible error. Furthermore, by a suitable rotation of the x, y coördinate system along which the components z_x,z_y are measured, it is always possible to make $a_{xy} = 0$. The slope components $z_{x'},z_{y'}$ along these "principal axes," x', y', are distributed according to

$$p_o = M \exp\left\{ -\frac{1}{2}\left[\left(\frac{z_{x'}}{\sigma_c}\right)^2 + \left(\frac{z_{y'}}{\sigma_u}\right)^2\right]\right\} = (2\pi\ \sigma_c\sigma_u)^{-1} \exp\left[-\tfrac{1}{2}(\xi^2 + \eta^2)\right], \qquad (6.1\text{–}2)$$

where σ_c,σ_u are r.m.s. slope components along the principal axes x',y'. (It will be shown that x' and y' can be taken crosswind and upwind, respectively, hence the notation σ_c,σ_u.) $M = (2\pi\sigma_c\sigma_u)^{-1}$ normalizes p_o; and ξ, η are "standardized" slope components $z_{x'}/\sigma_c$, $z_{y'}/\sigma_u$.

6.2 *Gram-Charlier series.*—The Gram-Charlier series, which generalizes the Gaussian distribution, is

$$p = (2\pi\ \sigma_c\sigma_u)^{-1} \exp\{-\tfrac{1}{2}(\xi^2 + \eta^2)\} \sum_{i=0}^{\infty}\sum_{j=0}^{\infty} (-1)^{i+j} \frac{c_{ij}}{i!j!} H_i(\xi)H_j(\eta) \qquad (6.2\text{–}1)$$

where $H_n(x)$ is the nth Hermite polynomial

$$\left.\begin{aligned} H_n(x) &= x^n - \frac{n(n-1)}{2} x^{n-2} + \frac{n(n-1)(n-2)(n-3)}{2\cdot 4} x^{n-4} - \cdots ; \\ H_o(x) &= 1 ; \quad H_1(x) = x ; \quad H_2(x) = x^2 - 1 ; \\ H_3(x) &= x^3 - 3x ; \quad H_4(x) = x^4 - 6x^2 + 3 ; \cdots \end{aligned}\right\} \qquad (6.2\text{–}2)$$

and the coefficients c_{ij} are to be determined. The polynomials have the property that

$$(\sqrt{2\pi}\ n!)^{-1} \int_{-\infty}^{\infty} H_n(x)H_m(x)\ e^{-x^2/2}\ dx = \begin{cases} 0 & \text{if } n \neq m \\ 1 & \text{if } n = m\ . \end{cases} \qquad (6.2\text{–}3)$$

The probability distribution is to have the three following properties:

It is to be normalized:

$$\iint_{-\infty}^{\infty} p\ dz_{x'}\ dz_{y'} = 1\ . \qquad (6.2\text{–}4)$$

The mean values $\bar{z}_{x'}$ and $\bar{z}_{y'}$ are to be zero:

$$\bar{z}_{x'} = \iint_{-\infty}^{\infty} z_{x'}\, p\, dz_{x'}\, dz_{y'} = 0\ ; \qquad \bar{z}_{y'} = \iint_{-\infty}^{\infty} z_{y'}\, p\, dz_{x'}\, dz_{y'} = 0\ . \tag{6.2-5}$$

The mean square slopes are to be σ_c^2 and σ_u^2:

$$\sigma_c^2 = \iint_{-\infty}^{\infty} z_{x'}^2\, p\, dz_{x'}\, dz_{y'}\ ; \qquad \sigma_u^2 = \iint_{-\infty}^{\infty} z_{y'}^2\, p\, dz_{x'}\, dz_{y'}\ . \tag{6.2-6}$$

Applying these requirements to (**6.1**–1 and –3) fixes five of the c_{ij}'s as follows:

$$1 = \iint p\, dz_{x'}\, dz_{y'} = \sigma_c\sigma_u \iint p\, d\xi\, d\eta = c_{00}\ . \tag{6.2-4a}$$

$$0 = \iint z_{x'}\, p\, dz_{x'}\, dz_{y'} = \sigma_c^2\sigma_u \iint \xi\, p\, d\xi\, d\eta$$

$$= \sigma_c^2\sigma_u \iint H_1(\xi)\, p\, d\xi\, d\eta = c_{10}\ . \tag{6.2-5a}$$

Similarly, $c_{01} = 0$.

$$\sigma_c^2 = \sigma_c^3\sigma_u \iint \xi^2 p\, d\xi\, d\eta = \sigma_c^3\sigma_u \iint [H_2(\xi) + 1]\, p\, d\xi\, d\eta$$

$$= \sigma_c^2(c_{00} + c_{20}) = \sigma_c^2(1 + c_{20})\ . \tag{6.2-6a}$$

Therefore $c_{20} = 0$. Similarly, $c_{02} = 0$.

The probability distribution can now be written

$$p = (2\pi\, \sigma_c\sigma_u)^{-1} \exp\left[-\tfrac{1}{2}(\xi^2 + \eta^2)\right] \Big\{ 1 - \frac{1}{6} c_{30}(\xi^3 - 3\xi) - \frac{1}{2} c_{21}(\xi^2 - 1)\eta$$

$$- \frac{1}{2} c_{12}\, \xi(\eta^2 - 1) - \frac{1}{6} c_{03}(\eta^3 - 3\eta) + \frac{1}{24} c_{40}(\xi^4 - 6\xi^2 + 3) + \frac{1}{6} c_{31}(\xi^3 - 3\xi)\eta$$

$$+ \frac{1}{4} c_{22}(\xi^2 - 1)(\eta^2 - 1) + \frac{1}{6} c_{13}\, \xi(\eta^3 - 3\eta) + \frac{1}{24} c_{04}(\xi^4 - 6\xi^2 + 3) + \cdots \Big\}\ . \tag{6.2-7}$$

The terms indicated will be sufficient provided the probability distribution is close to Gaussian and provided large values of ξ and η are excluded.

Two empirical results may be anticipated: (1) one of the principal axes (say y') points upwind; (2) there is no asymmetry crosswind. In the present notation

$c_{30} = c_{12} = c_{31} = c_{13} = 0$, since each of these coefficients multiplies an odd function of ξ. With these simplifications, the distribution function is derived in its final form:

$$p = (2\pi\sigma_c\sigma_u)^{-1} \exp\left[-\tfrac{1}{2}(\xi^2+\eta^2)\right]\left\{1 - \frac{1}{2}c_{21}(\xi^2-1)\eta - \frac{1}{6}c_{03}(\eta^3-3\eta)\right.$$

$$\left. + \frac{1}{24}c_{40}(\xi^4-6\xi^2+3) + \frac{1}{4}c_{22}(\xi^2-1)(\eta^2-1) + \frac{1}{24}c_{04}(\eta^4-6\eta^2+3)\right\}. \qquad \textbf{(6.2–8)}$$

7. Method for Evaluating Coefficients in the Distribution Function

To evaluate the constants σ_c, σ_u, c_{21}, c_{03}, c_{40}, c_{22}, c_{04} from the tabulated values of $\log p(\alpha, \beta)$, one must take into account (1) that the tabulated values are in terms of x,y and (**6.2**–8) in terms of x',y'; (2) that the tabulated values are in logarithmic

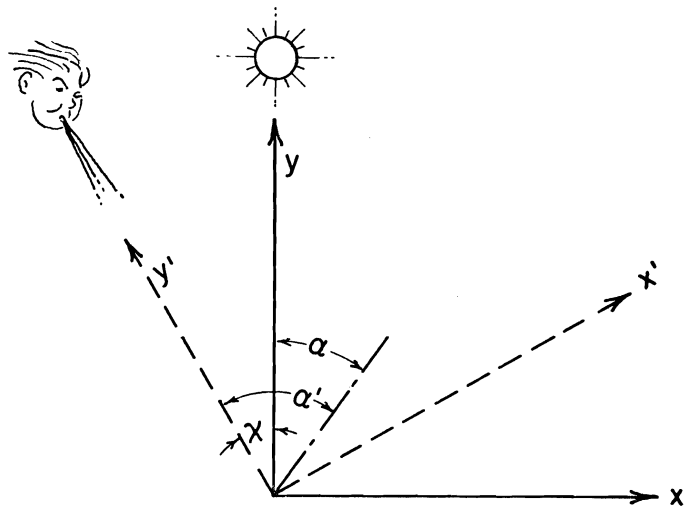

Fig. 7. Notation for rotation of coördinate system from solar (x,y) system to principal axes (x',y'). It is found that y'-axis points upwind.

form and the equation in nonlogarithmic form; and (3) that information concerning the very infrequent, very large slopes was limited by background.

7.1 *Rotation.*—The wind system x',y' is rotated relative to the "solar system" x,y (fig. 1; see sec. **3**) through an angle χ. Hence (fig. 7)

$$\alpha' = \alpha + \chi\,, \qquad \textbf{(7.1–1)}$$

$$\left.\begin{aligned} \xi &= z_{x'}/\sigma_c = (m/\sigma_c)\sin\alpha'\,, \\ \eta &= z_{y'}/\sigma_y = (m/\sigma_u)\cos\alpha'\,, \end{aligned}\right\} \qquad \textbf{(7.1–2)}$$

where $m = \tan\beta = (z_x^2 + z_y^2)^{\frac{1}{2}}$. With these substitutions (**6.2**–8) becomes

$$\left.\begin{aligned} p &= (2\pi\,\sigma_c\sigma_u)^{-1}(1+t)\,\exp\left\{\frac{m^2}{4}\left[-\left(\frac{1}{\sigma_c^2}+\frac{1}{\sigma_u^2}\right)+\left(\frac{1}{\sigma_c^2}-\frac{1}{\sigma_u^2}\right)\cos 2\alpha'\right]\right\}, \\ t &= \frac{1}{8}(c_{40}+2c_{22}+c_{04}) - \frac{m^2}{8}\left[\frac{c_{40}}{\sigma_c^2}+c_{22}\left(\frac{1}{\sigma_c^2}+\frac{1}{\sigma_u^2}\right)+\frac{c_{04}}{\sigma_u^2}\right] + m^4\mathbf{a}_o'' \\ &\quad + m(\mathbf{a}_1 + m^2\mathbf{a}_1')\cos\alpha' \\ &\quad + \frac{1}{8}m^2\left[\frac{c_{40}}{\sigma_c^2}+c_{22}\left(\frac{1}{\sigma_c^2}-\frac{1}{\sigma_u^2}\right)-\frac{c_{04}}{\sigma_u^2}+8\,m^2\mathbf{a}_2'\right]\cos 2\alpha' \\ &\quad + m^3\mathbf{a}_3\cos 3\alpha' + m^4\mathbf{a}_4\cos 4\alpha', \end{aligned}\right\} \quad (7.1\text{–}3)$$

where

$$\mathbf{a}_o = \frac{1}{8}(c_{40}+2c_{22}+c_{04}) - \log(2\pi\,\sigma_c\sigma_u), \quad (7.1\text{–}4a)$$

$$\mathbf{a}_o' = \frac{1}{4}\left(\frac{1}{\sigma_c^2}+\frac{1}{\sigma_u^2}\right)+\frac{1}{8}\left[\frac{c_{40}}{\sigma_c^2}+c_{22}\left(\frac{1}{\sigma_c^2}+\frac{1}{\sigma_u^2}\right)+\frac{c_{04}}{\sigma_u^2}\right], \quad (7.1\text{–}4b)$$

$$\mathbf{a}_o'' = \frac{1}{64}\left(\frac{c_{40}}{\sigma_c^4}+\frac{2c_{22}}{\sigma_c^2\sigma_u^2}+\frac{c_{04}}{\sigma_u^4}\right), \quad (7.1\text{–}4c)$$

$$\mathbf{a}_1 = \frac{c_{03}+c_{21}}{2\sigma_u}, \quad (7.1\text{–}4d)$$

$$\mathbf{a}_1' = \frac{1}{8\sigma_u}\left(\frac{c_{21}}{\sigma_c^2}+\frac{c_{03}}{\sigma_u^2}\right), \quad (7.1\text{–}4e)$$

$$\mathbf{a}_2 = \frac{1}{4}\left(\frac{1}{\sigma_c^2}-\frac{1}{\sigma_u^2}\right)+\frac{1}{8}\left[\frac{c_{40}}{\sigma_c^2}+c_{22}\left(\frac{1}{\sigma_c^2}-\frac{1}{\sigma_u^2}\right)-\frac{c_{04}}{\sigma_u^4}\right], \quad (7.1\text{–}4f)$$

$$\mathbf{a}_2' = \frac{1}{4}\left(\frac{c_{40}}{\sigma_c^2}-\frac{c_{04}}{\sigma_u^2}\right), \quad (7.1\text{–}4g)$$

$$\mathbf{a}_3 = \frac{1}{8\sigma_u}\left(\frac{c_{21}}{\sigma_u^2}-\frac{c_{03}}{3\sigma_u^2}\right), \quad (7.1\text{–}4h)$$

$$\mathbf{a}_4 = \frac{1}{192}\left(\frac{c_{40}}{\sigma_c^4}-\frac{6c_{22}}{\sigma_c^2\sigma_u^2}+\frac{c_{04}}{\sigma_u^4}\right). \quad (7.1\text{–}4i)$$

The coefficients $\mathbf{a}_o$, $\mathbf{a}_o'$ do not appear in (**7.1**–3), but are defined for later reference.

7.2 *Relations between logarithmic and nonlogarithmic distributions.*—The data are tabulated in terms of log p, whereas (**7.1**–3) is in terms of p. There are two alternate approaches. One is to take the antilogarithms of the tabulated values, compute the

appropriate moments, and thus evaluate the coefficients in (**7.1**–3). The other approach is to derive an analytical expression for $\log p$ from (**7.1**–3) and to fit it to the tabulated values. Either way, the principal difficulty is how to fill in for those values of slope that are either below background or not covered by the photographs. The latter method, though less conventional, appears to be more satisfactory, since the empirical data can be nicely fitted to a simple analytical expression (sec. **8**).

Accordingly, $\log p$ is to be found from (**7.1**–3). If $t < 1$, then

$$\log t = t - \tfrac{1}{2} t^2 + \tfrac{1}{3} t^3 - \cdots .$$

Keeping only the terms up to $\cos 4\alpha'$ and disregarding powers of m larger than the fourth, the expansion takes the form

$$\log p = a_o - a_o' m^2 + a_o'' m^4 + m(a_1 + a_1' m^2) \cos \alpha' + m^2(a_2 + a_2' m^2) \cos 2\alpha' + a_3 m^3 \cos 3\alpha' + a_4 m^4 \cos 4\alpha' . \qquad (7.2\text{–}1)$$

In section **8** the a's will be evaluated from the empirical data, and it will be shown that the data are adequately represented by (**7.2**–1).

The problem is to compute the σ's and c's in (**6.2**–8) from the a's in (**7.2**–1). If the slope distribution were very close to Gaussian, i.e., $t \ll 1$ and $\log (1 + t) \approx t$, then, and then only, the coefficients in (**7.2**–1) are defined by the boldface coefficients in (**7.1**–4). In this case the five coefficients σ_c, σ_u, c_{40}, c_{22}, c_{04} could be evaluated from (**7.1**–4b, –4c, –4f, –4g, –4i). However, the errors inherent in this approximation are of the order of 10 per cent, and the data admit greater accuracy.

7.3 *The "incomplete" variances.*—A more accurate procedure is to derive formulas for computing σ_c and σ_u in terms of the second moment of p. The probability distribution can be written in the form

$$p = \exp (a_o + \Phi) , \qquad (7.3\text{–}1)$$

where e^{a_o} is a coefficient allowing for normalization and $\Phi(\alpha', m)$ the distribution function, represented by all but the first term on the right side of (**7.2**–1). This formula, although adequate within the range of observed slopes, cannot be adequate for very large slopes, since a_o'' is observed to be positive and the expression diverges as m approaches ∞.

The unknown parameter a_o can be eliminated in the following manner:

$$\left.\begin{aligned} 1 &= \iint_{-\infty}^{\infty} p \, dz_x \, dz_y = e^{a_o} I_o(\infty) , \\ \sigma_c^2 &= e^{a_o} I_1(\infty) = I_1(\infty)/I_o(\infty) , \end{aligned}\right\} \qquad (7.3\text{–}2)$$

where

$$I_o(M) = \int_o^M \int_{-\pi}^{\pi} m \, e^{\Phi} \, dm \, d\alpha' , \quad I_1(M) = \int_o^M \int_{-\pi}^{\pi} m^3 \sin^2 \alpha' \, e^{\Phi} \, dm \, d\alpha' . \qquad (7.3\text{–}3)$$

If $\Phi(\alpha',m)$ were known for all m (which it is not), then the integrals $I(\infty)$ could be evaluated and σ_c computed from (**7.3**–2). Actually Φ is known only for slopes up to some maximum value M_m. One can therefore compute only the "incomplete" variance

$$\sigma_c^2(M_m) = I_1(M_m)/I_o(M_m)$$

which will be somewhat less than $\sigma_c^2(\infty) = \sigma_c^2$ since the very infrequent, very large slopes have been neglected. However, there must be some value of slope, M_o, sufficiently large so that $\sigma_c^2(M_o)$ has sensibly reached its maximum value and no longer increases with M. There is no need to carry the integrations beyond this point.

Figure 8 shows a plot of the incomplete variances as a function of the dimensionless slope parameter $a_o'M^2$, according to (**7.3**–4 and –5), to be derived later. The

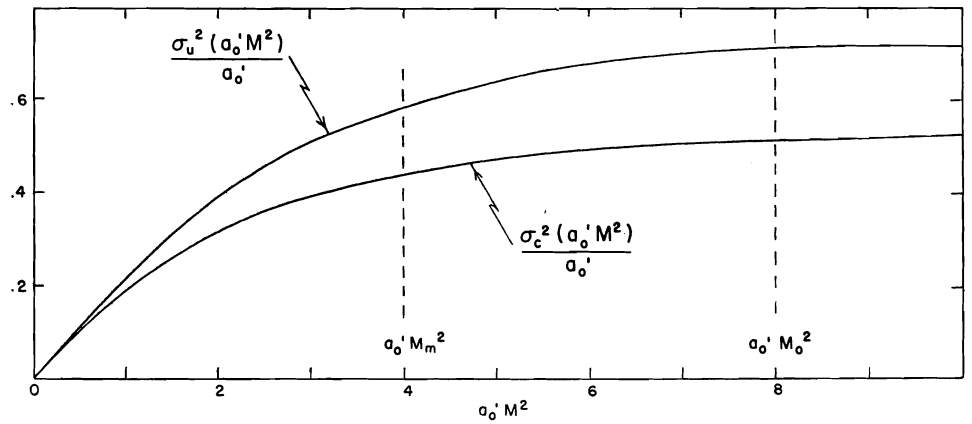

Fig. 8. Incomplete variances as functions of dimensionless slope parameter $a_o'M^2$. Based on composite of all analyzed data (clean sea surface).

curves represent a composite of all analyzed data. The empirical data extend to $a_o'M_m^2 \approx 4$, and it is apparent that the curves have not yet leveled off. If it is assumed, without further evidence, that the empirical formula (**7.2**–1) can be applied to slopes 40 per cent in excess of M_m, it is found that for $a_o'M^2 = 8$, curves have become virtually level at a value about one-fourth higher than for $a_o'M^2 = 4$. The procedure to be followed is to compute the incomplete variance for $a_o'M^2 = 4$ and then to allow for a blanket increase of 22 per cent in σ_c^2, 23 per cent in σ_u^2 for the uncontaminated surface; and 20 per cent in σ_c^2 and σ_u^2 for the slick surface.

7.31 *Formulas for incomplete variances.*—The integrands of I_o and I_1 are me^{Φ} and $m^3 \sin^2 \alpha' e^{\Phi}$ respectively, where Φ equals all but the first term in the expression for $\log p$ (**7.2**–1). The terms in $\cos \alpha'$, $\cos 3\alpha'$, and $\cos 4\alpha'$ contribute less than 2 per cent to these integrals and can be neglected. The remaining expressions are simplified by using the integral definitions

$$\pi J_o(z) = \int_o^{\pi} \exp(-i\,z\cos u)\,du\,, \quad \pi J_1(z) = -i\int_o^{\pi} \cos u \exp(-i\,z\cos u)\,du\,,$$

for the Bessel functions of the first kind, and zero and first order, respectively. One obtains

$$I_o(M) = 2\pi \int_o^M m \exp(-a_o' m^2 + a_o'' m^4) J_o[-i(a_2 m^2 + a_2' m^4)]\, dm ,$$

$$I_1(M) = \pi \int_o^M m^3 \exp(-a_o' m^2 + a_o'' m^4)\{J_o[-i(a_2 m^2 + a_2' m^4)] - J_1[-i(a_2 m^2 + a_2' m^4)]\}\, dm .$$

The product $\exp(a_o'' m^4)$ times the Bessel functions can be expanded in a convergent power series in m^2, and integrated term by term. Using the notation

$$K_n(x) = \int_o^x u^n e^{-u}\, du = n!\left[1 - e^{-x}\left(\frac{1}{0!} + \frac{x}{1!} + \cdots + \frac{x^n}{n!}\right)\right]$$

and denoting $K_n(a_o' M^2)$ simply by K_n with the argument understood, one finds

$$I_o = \pi\left\{K_o + \left(b_o'' + \frac{1}{4} b_2^2\right) K_2 + \frac{1}{2} b_2 b_2' K_3 + \left[\frac{1}{4} b_2^2 b_o'' + \frac{1}{4}(b_2')^2 + \frac{1}{2}(b_o'')^2 + \frac{1}{64} b_2^4\right] K_4 + \cdots\right\} , \quad \textbf{(7.3–4)}$$

$$\left.\begin{matrix} I_1 \\ I_1' \end{matrix}\right\} = \frac{\pi}{2a_o'^2}\left\{K_1 \mp \frac{1}{2} b_2 K_2 + \left(b_o'' + \frac{1}{4} b_2^2 \mp \frac{1}{2} b_2'\right) K_3 + \left(\frac{1}{2} b_2 b_2' \mp \frac{1}{2} b_2 b_o'' \mp \frac{1}{16} b_2^3\right) K_3 + \cdots\right\} , \quad \textbf{(7.3–5)}$$

where

$$\left.\begin{aligned} b_o'' &= a_o''/(a_o')^2 , & b_2 &= a_2/a_o' , \\ b_1 &= a_1/(a_o')^{1/2} , & b_2' &= a_2/(a_o')^2 , \\ b_1' &= a_1'/(a_o')^{3/2} , & b_3 &= a_3/(a_o')^{3/2} , \\ & & b_4 &= a_4/(a_o')^2 \end{aligned}\right\} \quad \textbf{(7.3–6)}$$

are dimensionless ratios of the power-series coefficients. The lower signs in the equation for I_1 refer to an integral I_1', which has the same relation to σ_u^2 as I_1 has to σ_c^2. The coefficients b_1, b_1', b_3, b_4, are introduced here for later reference.

According to figure 9 the coefficients b_o'', b_2, and b_2' do not vary systematically with wind speed, and we shall replace them by their mean values, +.040, +.20, −.022, for clean surface, and +.039, +.09, −.011, for slick surface, in order to check the adequacy of the number of terms in (**7.3**–4) and (**7.3**–5). In the case of the maximum observed slopes, for which the series converge the slowest, the argument

of the K_n functions is $a_o'M_m^2 = 4$. For a clean water surface, terms in the curly braces are

$$.982 + .079 - .008 + .013 + (-.006),$$

$$.909 - .161 + .213 - .065 + (.053 - .011),$$

$$.909 + .161 + .136 + .023 + (.020 - .002).$$

Values in parentheses refer to expansions beyond that given in (**7.3**–4) and (**7.3**–5). The upper line refers to (**7.3**–4); the lower two lines refer respectively to the upper and lower sign in (**7.3**–5). Convergence using the data for slick surfaces is equally rapid. Evidently the expansion has been carried to a sufficient number of terms.

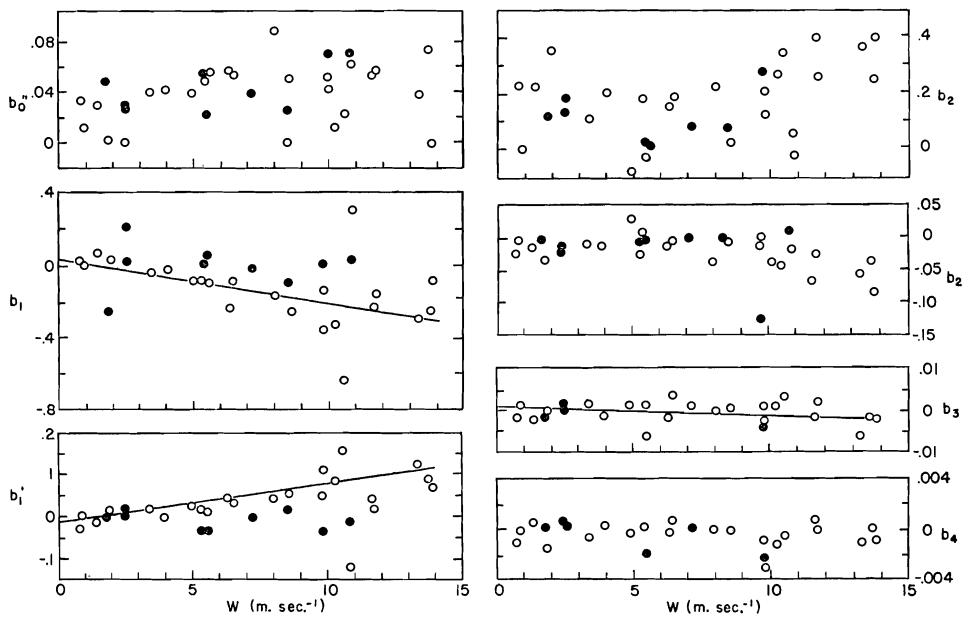

Fig. 9. Logarithmic distribution coefficients defined by (**7.2**–1) and (**7.3**–6) as functions of wind speed. Open circles refer to clean surface, solid circles to slick surface. The regression lines shown for b_1, b_1', b_3, were computed as described in section **9.2** for clean surface.

8. Evaluation of Coefficients in Logarithmic Distribution

In this section a harmonic analysis of the tabulated data is used to determine the angle of rotation from the "solar system" to the principal axes, and the a's of (**7.2**–1).

8.1 *Evaluation of* χ.—It will be seen from figure 10 that a Fourier analysis of the curves β = constant will have a pronounced second harmonic. This feature is used to determine the orientation χ of the principal axes. Suppose (sec. **5.7**) log p can be adequately represented by the series

$$A_o + A_1 \cos\alpha + B_1 \sin\alpha + A_2 \cos 2\alpha + B_2 \sin 2\alpha + \cdots + B_2 \sin 4\alpha \qquad (\mathbf{8.1}\text{–}1)$$

for a constant value of β. Rotating according to (**7.1**–1) we have

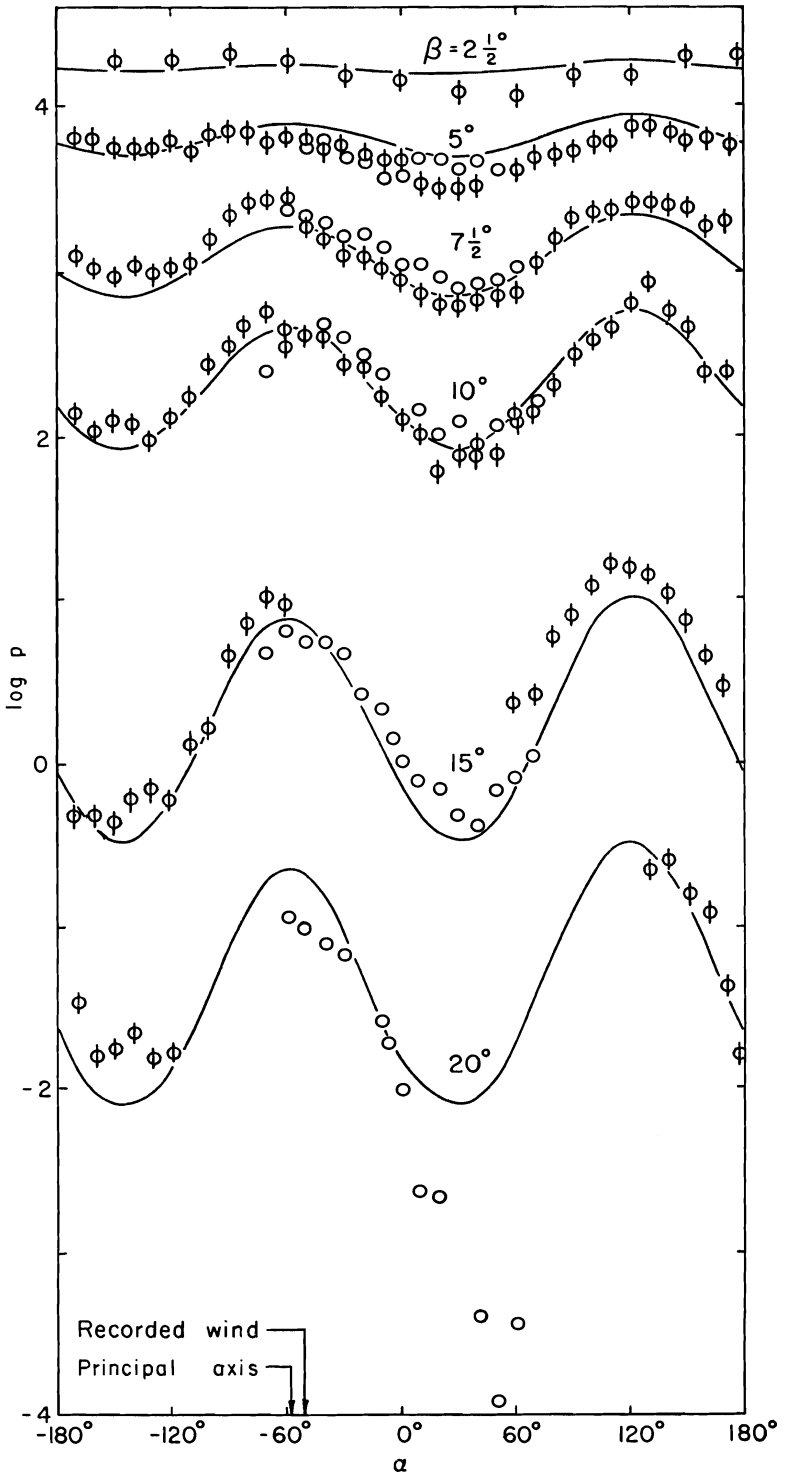

Fig. 10. Logarithm of unnormalized probability p as a function of azimuth α relative to sun, for indicated values of slope angle β. Open circles indicate data from tilted camera; barred circles, vertical camera. All measurements from photographs 4 Sept. k. Curves are drawn according to (**7.2**–1) using the coefficients listed in section **8.2**. The position of the principal y'-axis is indicated relative to recorded wind direction.

$$\log p = \cdots + A_2 \cos 2(\alpha' - \chi) + B_2 \sin 2(\alpha' - \chi + \cdots$$

$$= \cdots + (A_2 \cos 2\chi - B_2 \sin 2\chi) \cos 2\alpha' + (A_2 \sin 2\chi + B_2 \cos 2\chi) \sin 2\alpha' + \cdots.$$

By setting

$$\tan 2\chi = -B_2/A_2 \qquad \textbf{(8.1–2)}$$

we eliminate the term in sin $2\alpha'$. In practice the value of χ is taken as the average obtained from the curves $\beta = 2\frac{1}{2}°$, 5°, 10°, 15°, and 20°. Referred to the coördinate system rotated through this mean angle χ it is found (1) that the coefficients of sin $2\alpha'$ are reduced to "noise level" for *all* values of β; (2) that the amplitudes of the terms in sin α', sin $3\alpha'$, and sin $4\alpha'$ are likewise reduced to noise level; and (3) that the rotated y'-axis points nearly into the direction of the observed wind (fig. 11)

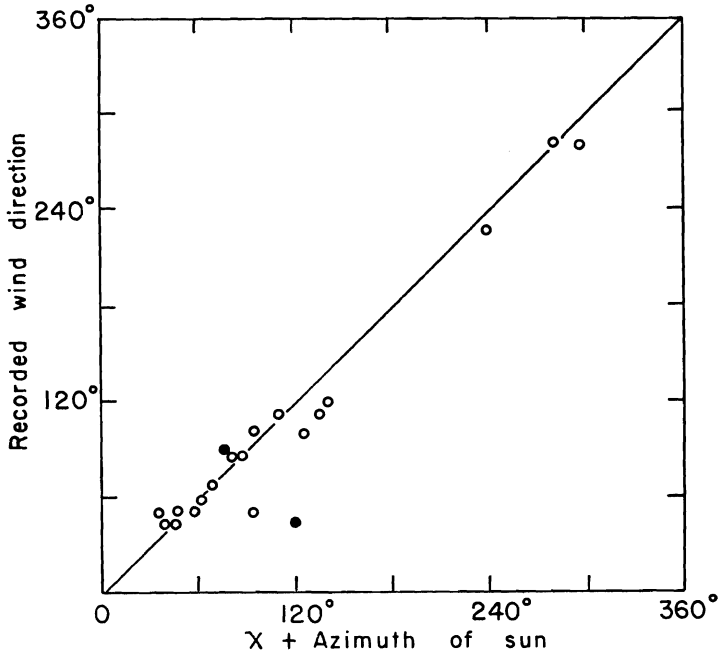

Fig. 11. Relation of the true bearing of principal y'-axis, χ plus azimuth of sun, relative to recorded wind direction. Open circles refer to clean sea surface; solid to slick surface.

except for some data from slick sea surface. The conclusions are (1) that the principal axes are in the direction of the wind and crosswind; (2) that there is no asymmetry crosswind.

The angle χ according to (**8.1**–2) is indeterminate by 180°. However, the observed wind direction agreed closely enough with one of the principal directions so that there was no difficulty in placing the positive y'-axis toward the wind. For nine photographic sets, 3 Sept. t, 4 Sept. y, 6 Sept. c, 10 Sept. k, 10 Sept. m, 10 Sept. r, 11 Sept. e, 11 Sept. f, and 13 Sept. e, the 2α terms were too small to determine χ, and the principal axes were oriented according to the observed wind direction. The observed wind direction and the bearing of the positive y'-axis (χ + sun azimuth) are summarized in table 1 (sec. **11.1**).

8.2 *The power-series coefficients.*—In terms of the x', y'-system the observed values are then adequately represented by the cosine series

$$\log p = A_o' + A_1' \cos \alpha' + A_2' \cos 2\alpha' + A_3' \cos 3\alpha' + A_4' \cos 4\alpha' , \qquad (8.2\text{–}1)$$

where $A_n' = A_n \cos n\chi - B_n \sin n\chi$. This is of the form assumed in the analytic development (**7.2**–1). On comparison

$$\begin{aligned} A_o' &= a_o - a_o' m^2 + a_o'' m^4 , \\ A_1' &= (a_1 + a_1' m^2) m , \\ A_2' &= (a_2 + a_2' m^2) m^2 , \\ A_3' &= a_3 m^3 , \\ A_4' &= a_4 m^4 . \end{aligned} \qquad (8.2\text{–}2)$$

The coefficients a_o', a_o'', etc., are then evaluated from the slopes and intercepts of the functions $(A_o' - a_o)m^{-2}$, $A_1'm^{-1}$, $A_2'm^{-2}$, etc., plotted against m^2. For the example 4 Sept. k the values are

$$\begin{aligned} a_o' &= 74.2, \quad a_1 = -0.28, \quad a_2 = 15, \quad a_3 = -0.52 , \\ a_o'' &= 230, \quad a_1' = 0.0, \quad a_2' = -69, \quad a_4 = 1.57 . \end{aligned}$$

The coefficient a_o is arbitrary. Figure 12 shows the comparison between the observed values of $\log p$ and those computed from (**7.2**–1), again based on the above values. Table 1 (sec. **11.1**) contains the values of the coefficients for all analyzed photographs.

9. Mean Square Slopes, Skewness, and Peakedness

In this section the coefficients in the distribution function

$$p = (2\pi\sigma_c\sigma_u)^{-1} \exp\left[-\tfrac{1}{2}(\xi^2 + \eta^2)\right] \left\{ 1 - \frac{1}{2} c_{21}(\xi^2 - 1)\eta - \frac{1}{6} c_{03}(\eta^3 - 3\eta) \right. \qquad (6.2\text{–}8)$$
$$\left. + \frac{1}{24} c_{40}(\xi^4 - 6\xi^2 + 3) + \frac{1}{4} c_{22}(\xi^2 - 1)(\eta^2 - 1) + \frac{1}{24} c_{04}(\eta^4 - 6\eta^2 + 3) \right\}$$

of the "standardized" cross- and upwind slope components

$$\xi = z_{x'}/\sigma_c , \qquad \eta = z_{y'}/\sigma_u$$

are derived from the power-series coefficients evaluated in section **8.2**.

9.1 *Mean square slopes.*—The mean square slope components, crosswind and

up/downwind, were computed for each set of photographs according to the formulas

$$\sigma_c^2 = \left\{ \begin{matrix} 1.22 \\ \\ 1.20 \end{matrix} \right\} I_1(4)/I_o(4) \ , \qquad \sigma_u^2 = \left\{ \begin{matrix} 1.23 \\ \\ 1.20 \end{matrix} \right\} I_1'(4)/I_o(4)$$

where the functions $I(a_o'M^2)$ are given by (**7.3**–4, –5), and the factors $\left\{ \begin{matrix} 1.22 \\ 1.20 \end{matrix} \right\}, \left\{ \begin{matrix} 1.23 \\ 1.20 \end{matrix} \right\}$ allow for the lack of information concerning large and infrequent slopes (sec. **7.3**). The upper number applies to a clean water surface and the lower to a slick surface.

Values are summarized in table 1 (see sec. **11.1**). Figure 13 shows a plot of the mean square slope components, and of the mean square slope $\sigma_c^2 + \sigma_u^2$ (regardless of direction), as functions of the wind speed W(in m. sec.$^{-1}$) recorded at 41 feet above

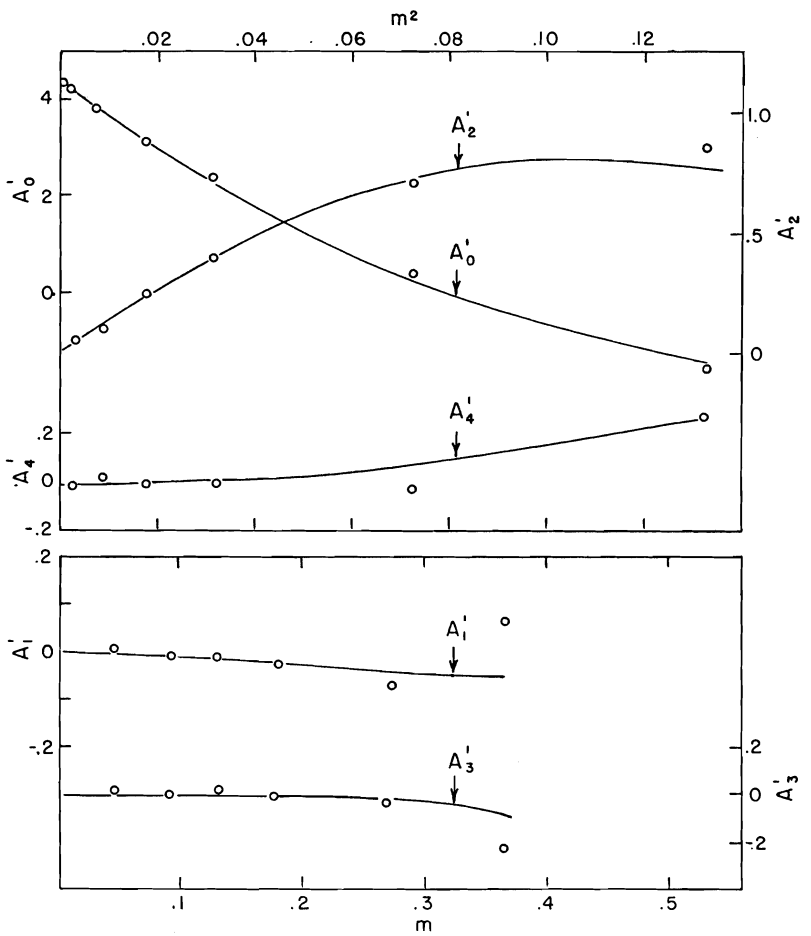

Fig. 12. Observed and computed values of Fourier coefficients as functions of slope, m. Data from photographs 4 Sept. k.

sea level. The regression lines and correlation coefficients r have been computed by the method of least squares:

$$\text{clean surface} \begin{cases} \sigma_c^2 = .003 + 1.92 \times 10^{-3} W \pm .002 & r = .956 \\ \sigma_u^2 = .000 + 3.16 \times 10^{-3} W \pm .004 & r = .945 \\ \sigma_c^2 + \sigma_u^2 = .003 + 5.12 \times 10^{-3} W \pm .004 & r = .986 \end{cases}$$

$$\text{slick surface} \begin{cases} \sigma_c^2 = .003 + 0.84 \times 10^{-3} W \pm .002 & r = .78 \\ \sigma_u^2 = .005 + 0.78 \times 10^{-3} W \pm .002 & r = .70 \\ \sigma_c^2 + \sigma_u^2 = .008 + 1.56 \times 10^{-3} W \pm .004 & r = .77 \end{cases}$$

The values preceded by ($\pm$) are the standard deviations of the differences between observed values and corresponding values computed according to the regression lines. In computing the regression lines each point is weighted according to the total number of densitometer readings on which it is based.

One point at $\sigma_c^2 = .0152$, $\sigma_u^2 = .0153$, $W = .89$ m. sec.$^{-1}$ (3 Sept. t) was omitted in the calculation. The deviation of the $\sigma_c^2 + \sigma_u^2$ value from the regression line is six times the standard deviation. Clearly some special conditions must apply to this observation. An examination of the wind record on 3 Sept. reveals that the wind was quite variable at the place where this observation was taken and was as high as 4.5 m. sec.$^{-1}$ only ten minutes before the photographs were taken. Quite possibly the wind speed at the vessel, which was just outside the glitter, was markedly lower than within the glitter area itself.

9.2 *Skewness.*—The determination of the skewness coefficients c_{21}, c_{03}, depends critically on the alignment of grid and photograph (sec. **3.1**) and hence the accuracy to which the corrections for the pitch, roll, and yaw of the plane have been made. Under the circumstances equations (**7.1**–4) are sufficiently accurate for determining the coefficients.

Equations (**7.1**–4d, –4e, –4h) form an overdetermined system for c_{21} and c_{03}. Eliminating the two coefficients from the three equations yields the relation

$$a_1 + (\sigma_c^2 + 3\sigma_u^2)a_1' - 3(\sigma_c^2 - \sigma_u^2)a_3 = 0\,, \qquad (\mathbf{9.2}\text{–}1)$$

which is equivalent to the requirement that the average slope be zero. Multiplying by $(a_o')^{-\frac{1}{2}}$ and using the definitions (**7.3**–6) give the equivalent relation

$$b_1 + a_o'(\sigma_c^2 + 3\sigma_u^2)b_1' - 3a_o'(\sigma_c^2 - \sigma_u^2)b_3 = 0\,. \qquad (\mathbf{9.2}\text{–}2)$$

The dimensionless b coefficients have standard deviations independent of wind speed and are therefore the appropriate coefficients in computing the regression lines.

It is seen from figure 14 that the products $a_o'\sigma_c^2$ and $a_o'\sigma_u^2$ do not vary systematically with wind speed. Replacing these products by their average values $0.52 \pm .05$ and $0.72 \pm .04$ (for uncontaminated sea surface) yields

$$b_1 + 2.68b_1' + 0.60b_3 = 0\,. \qquad (\mathbf{9.2}\text{–}3)$$

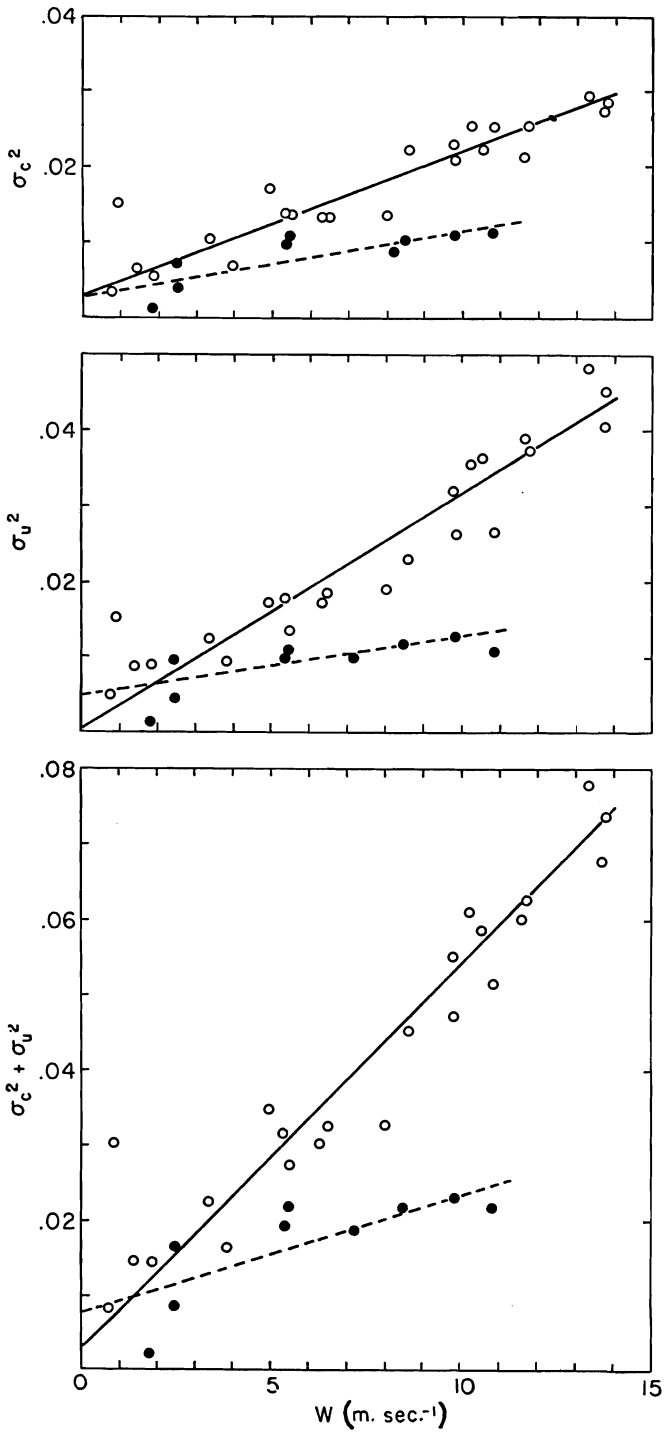

Fig. 13. Mean square slope components and their sum as functions of the wind speed W measured 41 ft. above sea level. The plot includes all analyzed data for clean sea surfaces (open circles) and slick surfaces (solid circles). Continuous lines are regression lines for clean surfaces; dashed lines for slick surfaces.

The procedure is to compute the least square regression of the b's on wind speed, with the added requirement that they must satisfy condition (**9.2**–3) of zero mean slope.

The relations are

$$b_1 = .03 - 2.4 \times 10^{-2}W \pm .10$$
$$b_1' = -.01 + 0.9 \times 10^{-2}W \pm .03$$
$$b_3 = .001 - .02 \times 10^{-2}W \pm .002\,.$$

The regression lines are shown on figure 9 (sec. **7.31**). Two clean water points deviate widely at about 11 m. sec.$^{-1}$. One point has low statistical weight because part of

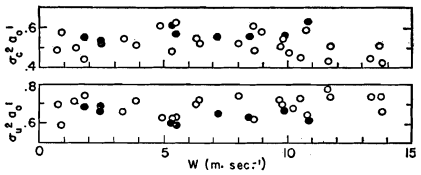

Fig. 14. The products $a_o'\sigma_c^2$ and $a_o'\sigma_u^2$ as functions of the wind speed W measured 41 ft. above sea level. Open circles refer to clean surface; solid circles to slick surface.

the slope field was obscured by a slick; the other is based on one photograph, 17 Sept. A, for which the sun was 10° lower than for any other analyzed photograph.

It follows from (**7.1**–4e, –4h) that

$$c_{21} = 2(a_o')^{3/2}\sigma_c^2\sigma_u(3b_3 - b_1'), \quad c_{03} = -6(a_o')^{3/2}\sigma_u^3(b_3 + b_1')\,, \qquad (\mathbf{9.2}\text{–}4)$$

whence

$$c_{21} = 0.01 - 0.86 \times 10^{-2}W \pm .03, \quad c_{03} = 0.04 - 3.3 \times 10^{-2}W \pm .12 \qquad (\mathbf{9.2}\text{–}5)$$

for uncontaminated water.

In the presence of slicks, the scatter of points is too great to evaluate the dependence on wind speed, if any. Setting $a_o'\sigma_c^2 = 0.55 \pm .03$ and $a_o'\sigma_4^2 = 0.62 \pm .04$, the mean values are

$$b_1 = +0.02 \pm .11; \quad b_1' = -0.006 \pm .017; \quad b_3 = -0.001 \pm .002 \qquad (\mathbf{9.2}\text{–}6)$$
$$c_{21} = 0.00 \pm .02; \quad c_{03} = 0.02 \pm .05\,.$$

9.3 *Peakedness.*—The computed values depend critically on the correction for background light (sec. **5**). Within the accuracy of the measurements, b_o'', b_2', and b_4 are independent of wind speed (fig. 9; see sec. **7.31**) and have the mean values

clean surface: $b_o'' = 0.040 \pm .021$; $b_2' = -0.022 \pm .023$; $b_4 = -0.0004 \pm .0008$

slick surface: $0.039 \pm .017$; $-0.011 \pm .029$; $-0.0003 \pm .0010$.

The peakedness coefficients are then found with sufficient accuracy from (**7.1**–4c, –4g, –4i). With the help of (**7.3**–6) the required expressions are

$$c_{40} = 24(\sigma_c^2 a_o')^2(b_o'' - b_2' + b_4)\,,$$
$$c_{22} = 8(\sigma_c^2 a_o')(\sigma_u^2 a_o')(b_o'' - 3b_4)\,,$$
$$c_{04} = 24(\sigma_u^2 a_o')^2(b_o'' + b_2' + b_4)\,.$$

Using mean values for all quantities on the right, the result is

clean surface: $c_{40} = 0.40 \pm .23$; $c_{22} = 0.12 \pm .06$; $c_{04} = 0.23 \pm .41$

slick surface: $0.36 \pm .24$; $0.10 \pm .05$; $0.26 \pm .31$

10. Experimental Errors and Effects of Fluctuating Winds

In this section we shall consider the causes and expected magnitudes of (1) experimental errors and (2) unavoidable effects of fluctuating atmospheric conditions. These causes bring about random effects which show up in observational scatter, and systematic effects which do not.

10.1 *Random errors.*—In the preceding section the standard deviations of the individual observation *from* the regression lines (for the mean square slopes and skewness) or *from* the mean values (for peakedness) have been included. The standard deviation *of* the mean observed peakedness is $n^{-\frac{1}{2}}$ times this value, where n is the number of observations.

Imperfections in the developing of the films result in errors in the photographic γ (sec. **4.4**), and these errors cause roughly proportional errors in the mean square slopes of about ± 5 per cent. This accounts for most of the observed scatter of $\sigma_c^2 + \sigma_u^2$, but not for the scatter of σ_c^2 or σ_u^2 alone (sec. **10.3**).

A more important source of error arises in the subtraction of background light. It will be recalled that the sky intensity curves were fitted to the reflected light just outside the glitter pattern (sec. **5.3**). This fitting is critically affected by the low intensity "toe" of the D-log E calibration of the photographic film and also by cloud reflections and other unknown factors. This is probably the principal cause of the scatter in peakedness. Variation in wind speed may also introduce scatter (sec. **10.3**). Imperfect control for roll, pitch, and yaw by a fraction of a degree will introduce an error in skewness of the order of the scatter in skewness. Where the glitter is partly in a slick and partly out of a slick the principal source of error in the skewness results from an imperfect separation of the data into these two categories.

Errors resulting from reduction of glitter intensity due to cloud shadows have been avoided by study of the image photographs. At high wind speeds the problem of whitecaps requires special consideration. The location of whitecaps was noted on the image photographs, and the corresponding dark spots on the photometric photographs have been omitted from the measurements. At high winds this is troublesome, and one is likely to overestimate the frequency of high slopes. For some purposes it might have been more useful to determine the slope distribution regardless of whether such slopes are or are not related to whitecaps. Our method is not capable of doing this because of multiple reflection of light from foam bubbles.

10.2 *Systematic errors.*—Two complicating circumstances which have not been considered are (1) the presence of steep valleys in the sea surface which are hidden from the direct view of the camera or from the rays of the sun (this accounts for the fact that one rarely sees distant trees, dunes, or ships reflected in the sea; the reason, as pointed out by Minnaert [1940], is that "at a great distance one sees only the sides of waves turned toward us . . . . This makes it seem as if we saw all the objects . . . reflected in a slanting mirror"; for the same reason, the reflection of low, distant clouds is displaced toward the horizon); and (2) the occurrence of multiple reflections. By neglecting these complications we introduce systematic errors into any computation involving slopes steeper than one-half the elevation of the sun. We have on the whole avoided such errors by confining our measurements to sun elevations above 55°.

A minor source of systematic error results from certain mathematical approximations in section **7**. These affect only skewness and peakedness. The major source of systematic errors is the assumption of a uniformly bright sky dome in the background correction (sec. **5.1**). Without a further study of the variation in skylight it is impossible to estimate errors arising from this assumption. For high sun it seems reasonable that any deviations from uniformity depend to a great extent on angular distance from the sun. In this case the resulting errors in mean square slope and skewness are small, but it is not impossible that this systematic error may be largely responsible for the calculated values of peakedness. However, peakedness is to be expected, on theoretical grounds, from two causes: the deviation of waves of finite amplitude from sinusoidal shape, and the variability of wind speed.

10.3 *Variability of wind.*—Variability of wind direction and speed has systematic effects on the slope distribution, and because the variability of the wind field is itself a changeable quantity, it causes scatter of the data.

In order to demonstrate the systematic effects, we suppose that for an ideally constant wind the slope distribution is Gaussian:

$$p_o = (2\pi\sigma_{co}\sigma_{uo})^{-1} \exp\left[-\tfrac{1}{2}(z_x'/\sigma_{co})^2 - \tfrac{1}{2}(z_y'/\sigma_{uo})^2\right] . \qquad (\mathbf{10.3}\text{–}1)$$

Suppose the wind direction fluctuates, but that the wind speed remains constant. As a result, there will be superposition of many distributions, (**10.3**–1) having principal axes y' pointed in the various directions of the wind. It may be shown that such a combined distribution is still Gaussian and has one of its principal axes aligned with the mean wind direction:

$$p = (2\pi\sigma_c\sigma_u)^{-1} \exp\left[-\tfrac{1}{2}(z_x/\sigma_c)^2 - \tfrac{1}{2}(z_y/\sigma_u)^2\right] . \qquad (\mathbf{10.3}\text{–}2)$$

For the limiting case of a vanishing variability in direction

$$\sigma_c = \sigma_{co}, \qquad \sigma_u = \sigma_{uo} .$$

For the other limiting case of large variability, the slopes are isotropic, $\sigma_c = \sigma_u$. Furthermore, it may be shown that $\sigma_c^2 + \sigma_u^2$ is independent of the direction vari-

ability, and hence equals $\sigma_{co}^2 + \sigma_{uo}^2$. Therefore

$$\sigma_c^2 = \sigma_u^2 = \tfrac{1}{2}(\sigma_{co}^2 + \sigma_{uo}^2)$$

for the isotropic case.

Actual values of the ratio σ_c^2/σ_u^2 should therefore fall between the extreme values $\sigma_{co}^2/\sigma_{uo}^2$ for the steadiest winds, and unity for very unsteady winds. The lowest observed value is from the observation 28 Aug. b, $\sigma_c^2/\sigma_u^2 = 0.54$. The highest values for clean water are from 3 Sept. q, 3 Sept. t, 4 Sept. y, 11 Sept. e: $\sigma_c^2/\sigma_u^2 = 0.986 \pm .008$. For slick surfaces the ratios are on the average higher than for clean water. Mean values are 0.75 and 0.86 for clean and slick surfaces respectively.

Consider next the effect of a variability in wind speed, but with the wind direction remaining constant. This may result in peakedness. Again let p_o and p represent the probabilities due to steady and variable winds. Furthermore, suppose that the number of gusts having wind speeds between W and $W + dW$ is proportional to

$$p_W\, dW = (\sqrt{2\pi}\,\sigma_W)^{-1} \exp(-\tfrac{1}{2}t^2/\sigma_W^2)\, dW \qquad \textbf{(10.3–3)}$$

with $t = W - \overline{W}$ designating the variation from the mean wind $\overline{W}$, and σ_W the standard deviation. We assume $\sigma_W \ll \overline{W}$. If the dimensions of each gust are adequate to generate slopes according to (**10.3**–2) with the r.m.s. slope components $\sigma_c = cW^{\frac{1}{2}}$, $\sigma_u = uW^{\frac{1}{2}}$, and if the dimensions of the glitter are adequate to sample a representative number of gusts, then $p = \int p_W p_o dW$ is the probability of slopes as measured in the glitter. An appropriate expansion is

$$p_W p_o = (2\pi)^{-3/2}(cu\overline{W}\sigma_W)^{-1}\left\{1 + (t/\overline{W})[-1 + \tfrac{1}{2}(\xi_o^2 + \eta_o^2)]\right.$$

$$\left. + (t/\overline{W})^2\left[1 - (\xi_o^2 + \eta_o^2) + \frac{1}{8}(\xi_o^2 + \eta_o^2)^2\right] + \cdots\right\}$$

$$\cdot \exp\{-\tfrac{1}{2}[\xi_o^2 + \eta_o^2 + (t/\sigma_W)^2]\}\,,$$

whence

$$p = (2\pi cu\overline{W})^{-1} \exp[-\tfrac{1}{2}(\xi_o^2 + \eta_o^2])$$

$$\cdot\left\{1 + (\sigma_W/\overline{W})^2\left[1 - (\xi_o^2 + \eta_o^2) + \frac{1}{8}(\xi_o^2 + \eta_o^2)^2\right] + \cdots\right\}, \qquad \textbf{(10.3–4)}$$

where $\xi_o = z_{x'}/c\overline{W}^{\frac{1}{2}}$, $\eta_o = z_{y'}/u\overline{W}^{\frac{1}{2}}$, and $c^2\overline{W}$, $u^2\overline{W}$ are the mean square components to the present approximation. On comparison with the Gram-Charlier series (**6.2**–8) it is apparent that the variability in wind speed introduces peakedness in the form

$$c_{40} = 3\,c_{22} = c_{04} = 3\,\sigma_W^2/\overline{W}^2\,. \qquad \textbf{(10.3–5)}$$

The measured peakedness is not inconsistent with (**10.3**–5), yielding an adjusted

value of $\frac{1}{8}(c_{40} + 3c_{22} + c_{04}) = 0.36$. Thus a standard deviation in wind speed of about one-third the mean wind speed could generate the observed peakedness.

11. Discussion and Summary

The Gram-Charlier distribution function (**6.2**–8)

$$p = (2\pi\sigma_c\sigma_u)^{-1} \exp\left[-\tfrac{1}{2}(\xi^2 + \eta^2)\right]\left\{1 - \frac{1}{2}c_{21}(\xi^2 - 1)\eta - \frac{1}{6}c_{03}(\eta^3 - 3\eta)\right.$$

$$\left. + \frac{1}{24}c_{40}(\xi^4 - 6\xi^2 + 3) + \frac{1}{4}c_{22}(\xi^2 - 1)(\eta^2 - 1) + \frac{1}{24}c_{04}(\eta^4 - 6\eta^2 + 3)\right\}$$

gives an adequate description of the measured probability density of the "standardized" cross- and up/downwind slope components $\xi = z_{x'}/\sigma_c$, $\eta = z_{y'}/\sigma_u$. The measurements are valid for slope components $z_{x'}$, $z_{y'}$ up to two and one-half times their r.m.s. values σ_c,σ_u. There is no information on larger (and less frequent) slopes because of the limitations imposed by background radiation. With $m = \tan\beta$ designating the slope regardless of direction, and the angle of ascent measured to the right of the wind, it follows that

$$p\,dz_{x'}\,dz_{y'}; \quad m\,p\,d\alpha'\,dm; \quad p\tan\beta\sec^2\beta\,d\alpha'\,d\beta$$

are the probability densities of slope within the limits

$$z_x \pm \tfrac{1}{2}dz_{x'}, z_{y'} \pm \tfrac{1}{2}dz_{y'}; \quad \alpha' \pm \tfrac{1}{2}d\alpha', m \pm \tfrac{1}{2}dm; \quad \alpha' \pm \tfrac{1}{2}d\alpha', \beta \pm \tfrac{1}{2}d\beta,$$

respectively.

The distribution function p is illustrated in figure 15. The mean square slope, regardless of direction $\sigma_c^2 + \sigma_u^2$, increases linearly with wind speed, reaching a value of $(\tan 15.9°)^2$ for a wind speed of 14 m. sec.$^{-1}$ measured at 41 feet elevation. The crosswind component σ_c^2 and up/downwind component σ_u^2 each increase linearly with wind speed, but the correlation is poorer because the variability in wind direction affects them separately but does not affect their sum.

The principal axes are found to be oriented with the wind. The up/downwind mean square slope components are somewhat larger than the crosswind components. The ratio σ_c^2/σ_u^2 varies from 1.0 to 0.54, with a mean value of 0.75 for all photographs. For the slick surface the mean value is 0.86. This large variability is far in excess of experimental error. It is probably the result of differences, from one instance to the next, in the *variability* of the wind direction. Steady winds would lead to small values in σ_c^2/σ_u^2 whereas gusty winds would increase this ratio to somewhere near unity.

The skewness coefficients c_{21} and c_{03} of the Gram-Charlier series decrease with increasing wind speed from nearly zero at very low winds to $c_{21} = -.11$, $c_{03} = -.42$, at 14 m. sec.$^{-1}$ At the higher wind speeds the most probable azimuth of ascent for low slopes is directed downwind, whereas for very large slopes ($|\eta| \gtrsim 2$) it is directed upwind. The principal source of error results from imperfect correction for the roll,

pitch, and yaw of the plane. The peakedness coefficients c_{04}, c_{22}, c_{40}, are such as to make the very large and very small slopes more probable than for a Gaussian distribution.

The effect of oil slicks covering an area of roughly one-fourth square mile is to reduce the mean square slope (regardless of direction) by a factor of two to three, to eliminate skewness, but to leave peakedness unchanged.

Numerical results are summarized in table 1.

11.1 *Comparison with Duntley.*—Duntley (1950) has measured the surface slope components on Lake Winnipesaukee, New Hampshire, by recording electrically the

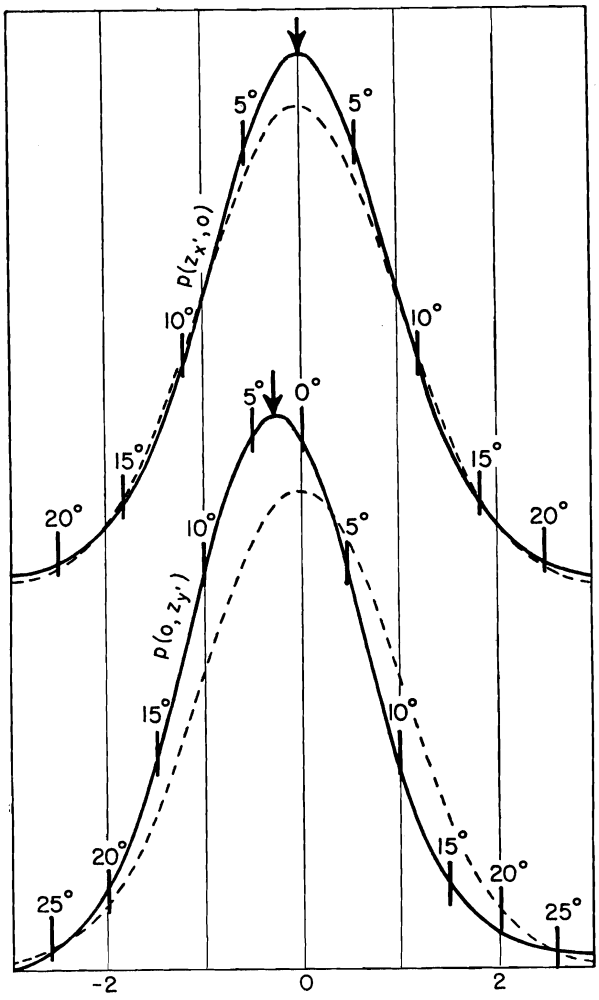

Fig. 15. Principal sections through the probability distribution surface $p(z_x',z_y')$. The upper curves are along the crosswind axis x', the lower curves along the upwind axis y'. The solid curves refer to the observed distribution, the dashed to a Gaussian distribution of equal mean square slope components. The thin vertical lines show the scale for the standardized slope components $\xi = z_x'/\sigma_c$ and $\eta = z_y'/\sigma_u$. The vertical scale depends on wind speed. The heavy vertical segments show the corresponding tilts $\beta = 5°, 10°, \ldots 25°$, for a wind speed of 10 m. sec.$^{-1}$; the skewness shown in the lower curve is computed for this wind speed. The modes are marked by arrows.

difference in immersion of pairs of thin vertical wires passing through the water surface. The wires were oriented to give simultaneous measurements of up/downwind and crosswind components. The separation between the wires was on different occasions 25 mm. and 9 mm.; consequently, the measurements refer to the average value of slope over these distances.

The analysis of Duntley's records of slope components *vs.* time was performed by counting the number of times, $n_{x'}$, $n_{y'}$, the trace crossed given values of $z_{x'}$, $z_{y'}$. It was found that these numbers could be represented approximately by

$$n_{x'} = n_c \exp\left[-\tfrac{1}{2}(z_{x'}/s_c)^2\right], \qquad n_{y'} = n_u \exp\left[-\tfrac{1}{2}(z_{y'}/s_u)^2\right], \qquad \textbf{(11.1–1)}$$

where n_c and n_u are the number of crossings of the zero slope axes; and s_c, s_u are constants depending on wind speed according to

$$s_c^2 = 5.5 \times 10^{-3} W, \qquad s_u^2 = 8.2 \times 10^{-3} W \qquad \textbf{(11.1–2)}$$

where W is measured in m. sec.$^{-1}$ The constants of proportionality have been corrected to an anemometer elevation of 41 feet above sea level.

On the assumption that the observed slope is due to the linear superposition of waves from a large number of random sources, Rice (1944) has shown that the distribution of slopes is Gaussian and

$$s_c = \sigma_c, \qquad s_u = \sigma_u . \qquad \textbf{(11.1–3)}$$

Comparison of Duntley's results with ours shows that (1) both investigations are consistent with a nearly Gaussian distribution of slopes; (2) both investigations indicate a linear increase of the mean square slope with wind speed; (3) the average value for the ratio σ_c^2/σ_u^2 is 0.67 for Duntley and 0.75 in our investigation; (4) the actual values for the mean square slopes are larger by a factor of 2.5 in Duntley's measurements than in ours. Possible explanations are the generation of short ripples by the wires themselves (fish line problem) as a consequence of the orbital movement of water past the wires, and reflection of waves by the wire support mechanism.

11.2 *Comparison with Schooley.*—Schooley's (1954) method consisted of measuring the highlighted area on *resolved* photographs of the reflection of an artificial light source over a river. At medium wind speeds the agreement of the two sets of data is satisfactory, although the ratio σ_c^2/σ_u^2 is somewhat lower in Schooley's data. For the highest and lowest wind speeds, Schooley's slope values are significantly smaller than ours (fig. 16).

The smaller ratio σ_c^2/σ_u^2 may well be the result of a smaller variability of wind direction. Schooley's photographs were made from a bridge over the Anacostia River; consequently the glitter pattern covered a very much smaller area in his photographs than in ours, and correspondingly would be expected to sample a smaller variability in wind.

The low values of the mean square slope components at very low winds in the river may easily be due to contamination of the river surface. At moderate winds,

TABLE 1

Photograph designation*	Time†	Location of cameras			Position of sun		Wind			Temperature		Humidity (per cent)	Significant waves		
		N. lat.	W. long.	Height (ft.)‡	Altitude	Azimuth	Speed (m. sec.$^{-1}$)		Direction (true)	Sea surface (° C.)	Air at 2 m. (° C.)		Height (ft.)	Period (sec.)	Direction (true)
							41 ft.‡	9 ft.‡							
28 Aug. b.....	1106	21°01.8′	156°45.8′	900	67°20′	119°	11.6	9.6	060°	26.15°	28.0°	69	3.5	4	...
28 Aug. p.....	1336	20°59.0′	156°44.0′	2,000	70°10′	236°	13.3	11.0	050°	26.4°	27.75°	69	6	5	056°
28 Aug. u.....	1403	20°58.2′	156°43.3′	2,000	64°30′	246°	13.8	11.6	050°	26.3°	27.5°	65	6	5	056°
28 Aug. v.....	1403	20°58.2′	156°43.3′	2,000	64°30′	246°	13.7	11.5	050°	26.3°	27.5°	65	6	5	056°
3 Sept. j.....	1157	20°39.5′	156°46.6′	2,000	75°10′	150°	.72	.45	050°	26.51°	29.0°	58	1.5	3	059°
3 Sept. q.....	1330	20°39.5′	156°46.6′	2,000	69°50′	230°	8.58	7.11	120°	26.49°	28.75°	61	2	3	101°
3 Sept. t.....	1357	20°39.5′	156°46.6′	2,140	64°30′	242°	.89	.54	180°	26.51°	29.0°	58	..	..	...
4 Sept. e.....	1126	20°40.2′	156°40.3′	2,000	70°10′	131°	1.79	.49	045°	25.90°	27.2°	69	1	2	120°
4 Sept. k.....	1158	20°39.0′	156°40.0′	1,950	75°00′	152°	3.93	3.58	100°	26.10°	27.9°	67	1	2	100°
4 Sept. n.....	1257	20°39.5′	156°36.9′	2,000	74°30′	209°	8.00	6.62	100°	26.20°	28.0°	69	2	3	106°
4 Sept. r.....	1324	20°40.0′	156°39.3′	2,000	70°30′	228°	6.30	5.27	111°	26.20°	28.0°	67	4	3	106°
4 Sept. v.....	1327	20°40.0′	156°39.3′	1,000	70°00′	230°	6.44	5.4	111°	26.20°	28.0°	67	4	3	106°
4 Sept. y.....	1353	20°39.5′	156°36.9′	1,900	65°00′	241°	4.92	4.07	110°	26.20°	28.0°	69	4	3	100°
5 Sept. b.....	1058	20°40.5′	156°35.7′	1,950	64°50′	121°	1.83	1.43	280°	26.6°	27.0°	68	3	4	160°
5 Sept. g.....	1124	20°40.1′	156°35.4′	1,950	70°00′	131°	1.39	.58	280°	26.7°	27.1°	67	3	4	104°
5 Sept. j.....	1354	20°46.8′	156°40.3′	2,050	64°30′	240°	3.35	2.99	225°	27.09°	27.0°	65	5	4	140°
6 Sept. c.....	1048	20°58.5′	156°45.3′	1,000	62°40′	120°	10.8	9.12	045°	25.95°	27.2°	69	4	4	045°
6 Sept. k.....	1124	20°58.0′	156°44.5′	2,000	69°10′	135°	10.2	8.85	045°	25.99°	27.2°	71	4	4	045°
6 Sept. q.....	1237	20°57.5′	156°44.0′	2,000	75°20′	195°	11.7	9.92	045°	26.3°	27.2°	69	5	4	045°
10 Sept. k	1328	20°40.0′	156°38.3′	1,800	67°50′	225°	8.45	7.24	130°	26.60°	26.8°	81	3	3	090°
10 Sept. m....	1333	20°40.0′	156°38.3′	900	67°00′	228°	7.15	6.00	130°	26.60°	26.8°	81	3	3	090°
10 Sept. r.....	1347	20°39.7′	156°39.3′	2,000	64°20′	232°	5.32	4.47	120°	26.59°	27.2°	76	3	3	090°
11 Sept. e.....	1317	20°45.5′	156°41.8′	1,000	69°20′	220°	5.45	3.75	210°	27.2°	27.3°	71	2	3	120°
11 Sept. f.....	1317	20°45.5′	156°41.8′	1,000	69°20′	220°	5.45	3.75	210°	27.2°	27.3°	71	2	3	120°
13 Sept. e.....	1308	20°17.6′	156°02.4′	2,150	69°50′	215°	2.41	1.97	090°	27.35°	28.4°	60	4	5	075°
13 Sept. f.....	1308	20°17.6′	156°02.4′	2,150	69°50′	216°	2.41	1.97	090°	27.35°	28.4°	60	4	5	075°
17 Sept. e.....	1136	20°29.9′	156°24.8′	2,000	68°40′	149°	9.79	8.31	086°††	26.80°	27.8°	76	4	3	080°
17 Sept. c, h, k, n, q¶ ..	1111 1205	20°28′	156°24′	2,000	65°15′ 71°30′	136° 169°	9.74	8.18	088°††	26.80°	27.7°	77	4	3	080°
17 Sept. A....	1424	20°17.6′	156°14.8′	1,800	54°40′	243°	10.5	8.45	068°††	26.90°	27.8°	79	5	3	080°

* Includes date of observation, 1951.
† Time meridian 150° W.
‡ Elevation above sea level.
§ True azimuth of principal (y′) axis.

SUMMARY OF ANALYZED DATA

Sea surface	Power-series coefficients (7.2-1)								x + Sun azimuth§	Mean square slope components		Weight factor‖
	a_0'	a_0''	a_1	a_1'	a_2	a_2'	a_3	a_4		σ_c^2	σ_u^2	
clean	20.2	22.	−1.0	3.7	8.1	− 26.	− .18	.30	063°	.0211	.0390	125
clean	15.4	9.0	−1.1	7.6	5.4	− 14.	− .35	− .25	057°	.0294	.0484	155
clean	14.7	0	− .30	3.9	5.9	− 18.	− .09	− .16	036°	.0287	.0452	157
clean	18.5	25.	−1.1	7.2	4.5	− 12.	− .12	+ .01	047°	.0276	.0404	160
clean	141.	680.	+ .23	−46.	33.	−440.	− 3.2	− 20.	095°	.00337	.00489	114
clean	27.4	39.	−1.3	+ 7.8	.43	− 3.2	+ .074	− .11	140°	.0224	.0230	158
clean	38.3	19.	0	0	0	0	.31	− .25	**	.0152	.0153	181
nat. slick	578.	16000.	−6.0	0	67.	0	−19.	+100.	120°	.00096	.00126	84
clean	74.2	240.	− .28	0	15.	− 69.	− .52	1.6	94°	.00694	.00977	179
clean	39.2	130.	−1.1	10.	8.8	− 55.	− .16	.18	126°	.0136	.0191	182
clean	41.0	97.	−1.5	11.	6.2	− 28.	− .28	− .28	136°	.0134	.0170	136
clean	39.2	85.	− .55	8.8	7.3	− 20.	+ .90	+ 1.2	119°	.0136	.0186	137
clean	35.9	51.	− .53	5.5	− 3.2	+ 41.	.27	− .18	**	.0172	.0174	139
clean	82.9	25.	+ .25	− 8.3	+29.	−190.	− .016	− 9.1	296°	.00534	.00906	156
clean	83.1	200.	.58	− 5.3	19.	−100.	− 1.5	+ 4.0	280°	.00609	.00875	156
clean	53.2	110.	− .37	+ 5.8	6.3	− 24.	+ .55	− 1.5	237°	.0102	.0125	188
clean	24.2	37.	+1.5	−15.	1.4	− 12.	...	...	**	.0252	.0265	42
oil slick	56.4	220.	.21	− 4.8	− 1.8	+ 32.	...	...		.0111	.0108	73
clean	18.9	4.6	−1.4	+ 6.9	+ 5.1	− 14.	+ .08	− .45	040°	.0254	.0357	159
clean	20.0	23.	− .70	2.2	5.0	− 11.	.21	− .039	045°	.0254	.0374	151
clean	19.3	0	...	...	...	...	...	...	**	....	....	51
oil slick	54.1	76.	− .69	6.9	3.9	0	...	...		.0102	.0117	97
oil slick	63.1	160.	− .18	− 2.1	5.3	0	.51	+ .25	**	.00860	.0100	100
clean	35.2	60.	− .46	+ 3.4	6.4	− 30.	...	...	**	.0137	.0179	59
oil slick	61.7	210.	0	−16.	.92	− 16.	...	...		.00967	.00985	67
clean	45.6	120.	− .58	+ 4.4	− 1.2	+ 18.	.40	.80	**	.0136	.0137	137
oil slick	54.1	58.	+ .23	−14.	+ .46	0	− 2.3	− 5.5	**	.0107	.0109	108
clean	68.6	0	...	...	...	...	...	...	**	....	....	37
oil slick	138.	460.	2.5	0	18.	−370.	− .18	+ 7.0		.00391	.00467	86
oil slick	69.8	140.	.23	+ 6.9	13.	− 69.	+ .67	1.9	076°	.00724	.00959	136
clean	26.5	37.	− .74	6.9	3.2	0	.094	− 2.0	080°	.0209	.0264	79
oil slick	51.1	180.	+ .023	−14.	14.	−340.	− 1.5	− 5.8		.0106	.0126	45
clean	22.3	21.	−1.7	+12.	4.6	− 6.9	− .27	− .49	087°	.0230	.0322	752
clean	20.1	9.0	−2.9	14.	6.9	− 18.	+ .31	− .26	069°	.0224	.0365	172

‖ No. of densitometer readings contributing to probability distribution.
¶ Probability distribution derived from 5 photographic sets.
** Observed wind direction used.
†† Wind direction estimated from direction of wind streaks on water; recorded wind direction appears to be in error by twice magnetic variation.

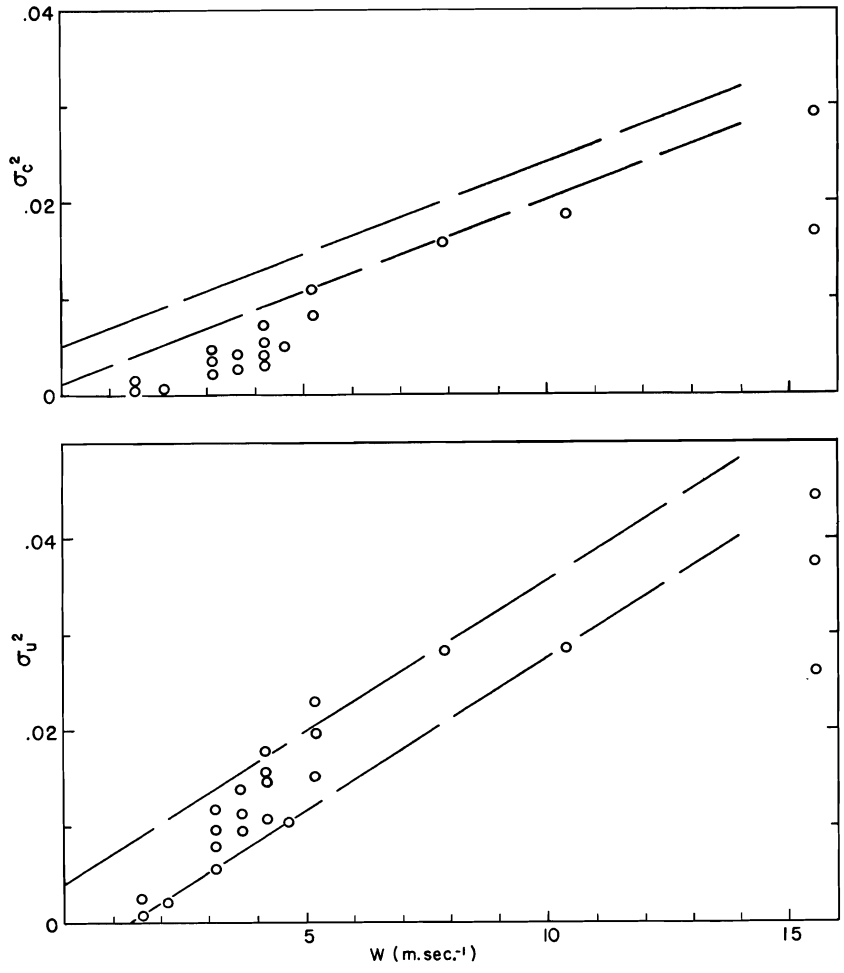

Fig. 16. Mean square slope components as functions of wind speed W. Open circles refer to measurements by Schooley in the Anacostia River. Dashed lines show the standard error limits to the regression lines based on the data of the present study.

surface films would be swept away. Schooley's low values at high winds may be due to (1) the fetch on the river being so short that the mean square slope was still increasing downwind; and (2) the imperfect resolution of highlighted areas on Schooley's photos. Visual inspection of sun glitter indicates that the curvature distribution of the sea surface becomes peaked at greater and greater values the higher the wind speed. This results in the glitter spots becoming smaller at higher winds. Resolution of the photographic setup then sets a limit to the wind speed for which high lights can be resolved.

PART II: INTERPRETATION

In this part the results described in Part I are to be interpreted in terms of various models of the sea surface. In sections **12–14** the simplest model is sought consistent with two observed features: the nearly Gaussian distribution of slopes and the

appropriate ratio of up/down to crosswind mean square slope components. These features do not place any severe restrictions on the dependence of the slope spectrum on wave frequency.

In sections **15–16** the more complicated models proposed respectively by Darbyshire and Neumann are examined. Only the Neumann wave spectrum is consistent with the remaining principal feature of the observed slope distribution: the linear increase of mean square slope with wind speed.

12. Waves in One Dimension

Before introducing the complications inherent in the two-dimensional character of the sea surface, we may consider waves the height of which varies in only one horizontal direction. If such waves existed on the ocean surface they would have infinitely long crests. The slope distribution would be one-directional, and the glitter pattern would consist of a single streak along some line α = constant. Clearly this is not in accord with observations (pls. 10–12).

12.1 *Single sine wave.*—Possible solutions of the hydrodynamical equations of motion for the elevation of the sea surface, z, and the slope component, z_x, are

$$z = (a/k) \sin kx, \qquad z_x = a \cos kx \tag{12.1–1}$$

for waves of small amplitude on the surface of a fluid with negligible viscosity. Since every cycle of undulation is alike, the probability distribution of slopes over a large area is the same as that within the half wave length $0 \leqq x < (\pi/k)$. Within this range, the fraction of the horizontal distance, $|\delta x| \div (\pi/k)$, within which the slope lies between the limits z_x and $z_x + \delta z_x$ is

$$\left(\frac{k}{\pi}\right) \frac{|\delta z_x|}{ak \sin kx} = \frac{|\delta z_x|}{\pi(a^2 - z_x^2)^{\frac{1}{2}}} .$$

provided $|z_x| < |a|$; and is zero for $|z_x| > |a|$, since $|a|$ is the maximum slope according to (**12.1**–1). This is also the probability, $p_1(z_x)\delta z_x$, for a slope between $z_x \pm \frac{1}{2}\delta z_x$; hence

$$p_1(z_x) = \begin{cases} \pi^{-1}(a^2 - z_x^2)^{-\frac{1}{2}} & \text{if} \quad z_x^2 < a^2 \\ 0 & \text{if} \quad z_x^2 > a^2 . \end{cases} \tag{12.1–2}$$

The distribution (**12.1**–2) is bimodal and far from Gaussian (fig. 17). Clearly a more complicated model is necessary to approximate the nearly Gaussian character of the observed distribution.

12.2 *Finite number of sine waves.*—The next step is to consider the linear superposition of N sine waves,

$$z_x = \sum_{j=1}^{N} a_j \cos (k_j x + \phi_j) . \tag{12.2–1}$$

We shall restrict the discussion to the case where the ratio of any two wave numbers,

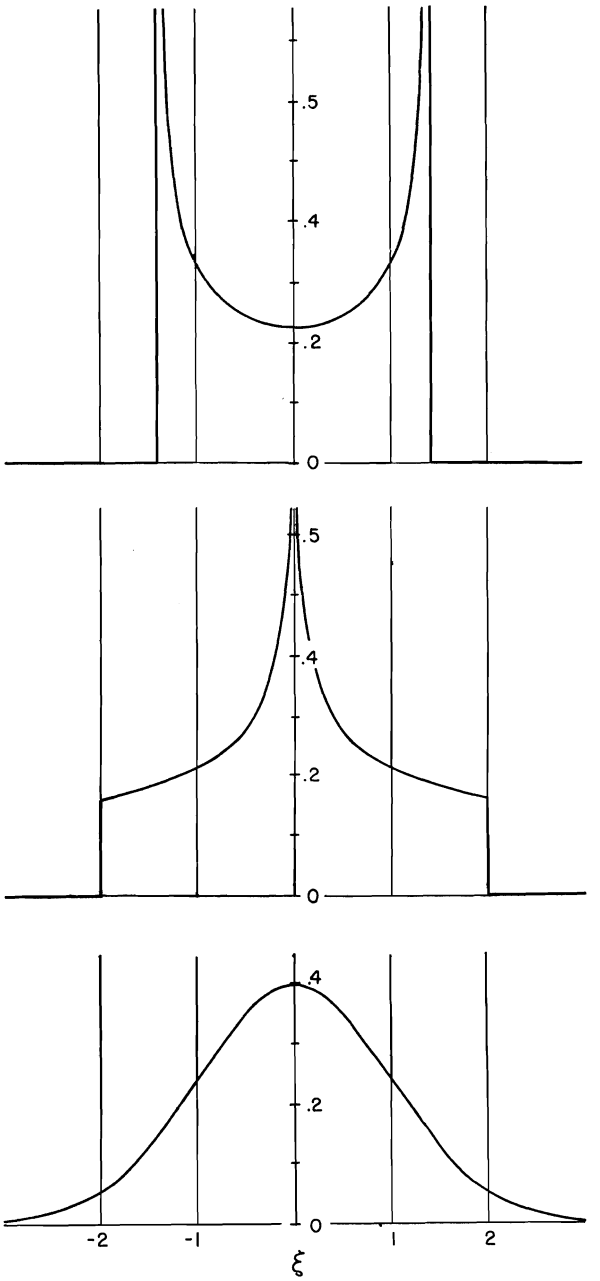

Fig. 17. Slope probabilities resulting from one sine wave (upper figure); the linear superposition of two sine waves of equal maximum slopes and irrational periods (center); and the linear superposition of an infinite number of irrational sine waves (lower). The horizontal scale is $\xi = z_x/\sigma_x$, the vertical gives $p_N(z_x)$ in units of σ_x^{-1}.

k_l/k_m, is irrational. The slope component is then an example of the "almost periodic function" of H. Bohr. As implied by its name, the almost periodic function comes very close to being periodic, but never quite repeats itself, a property which is in accord with our impressions of the real sea surface. The irrationality of the wave numbers forbids that (**12.2**–1) could represent any wave phenomenon in which the waves have rational "overtones," as, for example, Stokes waves of finite amplitude or seiches of a shallow rectangular body of water. In the open sea these are not believed to be serious limitations.

With the proviso of irrational wave numbers, the partial slope, $r_j = a_j \cos(k_j x + \phi_j)$, for the jth component is entirely uncorrelated with any particular value of partial slope for any other component; consequently the value of z_x is the sum of the N independent quantities r_j, and calculation of the distribution of z_x is an example of the problem of random flights (see, for example, Chandrasekhar, 1943). According to the solution obtained by Markoff, the probability $p_N(z_x)\,|\,\delta z_x\,|$ that the total slope lies within the limits $z_x \pm (\frac{1}{2}\,\delta z_x)$ is

$$p_N(z_x)\,|\,\delta z_x\,| = \frac{|\,\delta z_x\,|}{2\pi} \int_{-\infty}^{\infty} A_N(\rho) \exp(-i\,\rho\,z_x)\,d\rho\,, \tag{12.2–2}$$

where

$$A_N(\rho) = \prod_{j=1}^{N} \int_{-\infty}^{\infty} p_1(a_j,r_j) \exp(i\,\rho\,r_j)\,dr_j\,. \tag{12.2–3}$$

In the latter formula $p_1(a_j,r_j)dr_j$ is the probability that the jth component has the ordinate $r_j \pm \frac{1}{2}\,dr_j$. According to (**12.1**–2)

$$p_1(a_j,r_j) = \begin{cases} \pi^{-1}(a_j^2 - r_j^2)^{-\frac{1}{2}} & \text{if} \quad r_j^2 < a_j^2 \\ 0 & \text{if} \quad r_j^2 > a_j^2\,. \end{cases} \tag{12.2–4}$$

The integrals forming A_N can be evaluated by a known integral formula of the Bessel function of the first kind and zero order:

$$A_N = \prod_{j=1}^{N} J_o(\rho\,a_j)\,. \tag{12.2–5}$$

From the fact that $J_o(-x) = J_o(x)$, one may write $A_N(-\rho) = A_N(\rho)$ and

$$p_N(z_x) = \pi^{-1} \int_o^{\infty} \cos(\rho\,z_x) \left[\prod_{j=1}^{N} J_o(\rho\,a_j)\right] d\rho\,. \tag{12.2–6}$$

12.21 N *small.*—When $N = 2$, (**12.2**–6) reduces to

$$p_2(z_x) = \pi^{-1} \int_o^{\infty} J_o(\rho\,a_1)\,J_o(\rho\,a_2) \cos(\rho\,z_x)\,d\rho\,. \tag{12.2–7}$$

Applying the folding theorem of Fourier integrals (see, for example, Titchmarsh,

1937) this formula yields

$$p_2(z_x)|\delta z_x| = |\delta z_x| \int_{-\infty}^{\infty} p_1(a_1,u)\, p_1(a_2,z_x - u)\, du \qquad \textbf{(12.2–8)}$$

where the functions p_1 are those of (**12.2**–4). This is a reasonable result which could have been written down directly by noting that the likelihood of finding the slope $z_x \pm \frac{1}{2}\,\delta z_x$ is proportional to the number of times during which one component wave slope has the ordinate $u \pm \frac{1}{2}\,du$ and the other ordinate $z_x - u \pm \frac{1}{2}\,\delta z_x$. The probability of such a double occurrence is the product of the individual probabilities for waves of irrational wave numbers. Hence (**12.2**–8) follows directly. The only reason for the formal development is to prepare the way for large N.

Suppose $|a_1| = |a_2| = a$. Then (**12.2**–8) becomes, for $z_x^2 < 4a^2$,

$$p_2 = \pi^{-2} \int_{|z_x|-a}^{a} (a^2-u^2)^{-\frac{1}{2}}\, [a^2-(|z_x|-u)^2]^{-\frac{1}{2}}\, du = \frac{1}{\pi^2 a}\, K\left[1-\left(\frac{z_x}{2a}\right)^2\right]^{\frac{1}{2}} \qquad \textbf{(12.2–9)}$$

and zero otherwise. Here $K(x)$ is the elliptic integral $\int_0^{\pi/2} (1 - x^2 \sin^2 t)^{-\frac{1}{2}}\, dt$. The form of (**12.2**–9) is illustrated in figure 17 (sec. **12.1**) for comparison with the distribution p_1, (**12.1**–2). In this special case the distribution p_2 has a single, logarithmically infinite maximum. In the general case, $|a_1| \neq |a_2|$, there are two similar maxima.

The distribution function for three sine waves has not been found in closed form; however, it is possible to show that there are no infinite peaks for the distribution functions of three or more irrational sine waves. Since these functions are bounded, have a limited range in the variable z_x, and have only a finite number of discontinuities, it is possible to represent them by Gram-Charlier series (Cramer, 1946, p. 222). In the next section the asymptotic form of this series for large N is found by an expansion based on Markoff's method.

12.22 N *large.*—When N is large we may find $p_N(z_x)$ by noting that $A_N(\rho)$, equation (**12.2**–5), has a small value except near $\rho = 0$ owing to the character of J_o. The power-series expansion appropriate for small x is

$$J_o(x) = 1 - \frac{1}{4}\,x^2 + \frac{1}{64}\,x^4 + O(x^6) = e^{-\frac{1}{4}x^2}\left[1 - \frac{1}{64}\,x^4 + O(x^6)\right];$$

hence

$$A_N(\rho) = \exp\left[-\frac{1}{4}\,\rho^2 \sum_{j=1}^{N}(a_j)^2\right]\left\{1 - \frac{1}{64}\,\rho^4 \sum_{j=1}^{N}(a_j)^4 + O\left[\rho^6 \sum_{j=1}^{N}(a_j)^6\right]\right\}, \qquad \textbf{(12.2–10)}$$

and

$$p_N(z_x) = (\sqrt{2\pi}\sigma_x)^{-1} \exp(-\tfrac{1}{2}\xi^2)\left\{1 - \frac{\sum (a_j)^4}{64\sigma_x{}^4}(\xi^4 - 6\xi^2 + 3) + O\left[\sum (a_j)^6/\sigma_x{}^6\right]\right\}, \qquad \textbf{(12.2–11)}$$

where

$$2\sigma_x{}^2 = \sum_{j=1}^{N}(a_j)^2\,, \qquad \xi = z_x/\sigma_x\,. \qquad \textbf{(12.2–12)}$$

This series is of the Gram-Charlier type (sec. **6.2**). It approaches a Gaussian distribution represented by its first term as $N \to \infty$, provided

$$\lim_{N\to\infty} \sum_{j=1}^{N} (a_j)^{2m}/{\sigma_x}^{2m} = 0 \; ; \qquad m = 2, 3 \cdots . \tag{12.2–13}$$

If all a_j are equal, $a_j = a$, then the above sum is N^{-1} and the condition is satisfied. For less regular distributions one would still expect (**12.2**–13) to hold.

The second term within the braces of (**12.2**–11) is a term representing *negative* peakedness—compare (**6.2**–8), the two-dimensional form of a Gram-Charlier series. For $a_j = a$ and $N = 5$, 10, the corresponding values of peakedness are $-\frac{3}{2} N^{-1}$ or $-.30$, $-.15$, respectively, compared to the observed value $c_{40} = +0.4$. Hence the experimental results provide no evidence for discrete spectral components in the ocean waves.

12.3 *The continuous spectrum.*—A "Gaussian random" sea surface with a continuous spectrum of waves may be considered as the result of increasing the number of discrete sine wave components without limit and at the same time maintaining condition (**12.2**–13). By (**12.2**–11) the probability distribution of slopes is Gaussian. Since the observed distribution was to a first approximation Gaussian (in two dimensions), the sea-surface model represented by the linear superposition of a spectrum of waves in two dimensions will be chosen for detailed examination.

13. Waves in Two Dimensions Having a Continuous Spectrum

For waves with a continuous spectrum, it is no longer possible to give a simple formula analogous to (**12.1**–1) or (**12.2**–1); instead a complicated limiting process such as that indicated in section **12.3** seems necessary. There is, however, a statistical variable pertaining to the waves which may be stated in closed form and which is useful for relating the mean square slope to other observables; it is the correlation defined by

$$\psi(\boldsymbol{\varrho}, \tau) = \langle z(\mathbf{r}, t) z(\mathbf{r} + \boldsymbol{\varrho}, t + \tau) \rangle , \tag{13–1}$$

where $z(\mathbf{r},t)$ is the elevation of the sea surface at the point $\mathbf{r} = (x,y)$ and time t, and the symbol $\langle\ \rangle$ refers to an average over-all space. This definition of the correlation is possible only if the elevation $z(\mathbf{r})$ is statistically uniform over a large area.

13.1 *The frequency spectrum of the variance of elevation.*—Most observations of ocean waves have been made at a single point in space, say the point $\mathbf{r} = 0$. The result has been a record of $z(0, t)$ for a limited time $|t| < T$. Such a record may be represented by an infinite sum of sine waves of frequency ω and (complex) amplitude $g(\omega)$,

$$z(0,t) = \int_{-\infty}^{\infty} g(\omega)\, e^{i\omega t}\, d\omega , \tag{13.1–1}$$

where

$$g(\omega) = (2\pi)^{-1} \int_{-T}^{T} z(0,t)\, e^{-i\omega t}\, dt \tag{13.1–2}$$

according to the Fourier integral theorem.

But $g(\omega)$ is not a convenient function. It is sensitive to phase, and its absolute value tends to increase as the length of record $2T$ increases. On the other hand $|g(\omega)|^2$ is not phase sensitive. Furthermore, it is readily measured by passing the wave-generated signal through a narrow tuned filter. Since by hypothesis the sea surface is statistically uniform in time, the mean square of the sea-surface elevation must exist. According to Parseval's theorem (see, for example, Titchmarsh, 1937), the time average of z^2 is

$$\overline{z^2(0,t)} = \lim_{T\to\infty} \frac{1}{2T} \int_{-T}^{T} z^2(0,t)\, dt$$

$$= \lim_{T\to\infty} 2\pi \int_{-\infty}^{\infty} \frac{g(\omega)\, g(-\omega)}{2T}\, d\omega = \lim_{T\to\infty} 4\pi \int_{o}^{\infty} \frac{|g(\omega)|^2}{2T}\, d\omega \,. \quad \textbf{(13.1–3)}$$

The last equality follows because z is a real quantity, hence from **(13.1–2)** $g(-\omega) = g^*(\omega)$.

It would be tempting to assume that $\lim_{T\to\infty} \frac{g(\omega)^2}{2T}$ exists, and set

$$\mathbf{T}_\omega = \lim_{T\to\infty} \frac{4\pi\, |g(\omega)|^2}{2T} \,, \quad \textbf{(13.1–4)}$$

so that

$$\overline{z^2} = \int_{-\infty}^{\infty} \mathbf{T}_\omega\, d\omega \,. \quad \textbf{(13.1–5)}$$

If, as seems likely, the waves are due to a large number of impulses applied at random to the sea surface, then $\frac{|g(\omega)|^2}{2T}$ does not approach a limit. In fact, a plot of this function against ω is a wiggly line, oscillating more and more wildly as the record length, $2T$, increases. Since **(13.1–3)** is still correct, we can remove the difficulty by defining $(\bar{g})^2$ as a smoothed version of $|g|^2$ averaged over the arbitrarily small but finite range, $\omega \pm \epsilon$. The limit of $\bar{g}^2/2T$ then exists; hence **(13.1–4)** and **(13.1–5)** follow with $(\bar{g})^2$ in place of $|g|^2$. The rigorous mathematical approach uses a Lebesgue integral formula in place of **(13.1–3)**. (See, for example, Wiener, 1933.) The application of the Lebesgue integral to ocean-wave analysis is due to Pierson and Marks (1952).

In **(13.1–5)** $\mathbf{T}_\omega\, d\omega$ may be regarded as the contribution to $\overline{z^2}$ by waves in the frequency band $\omega \pm \frac{1}{2}\, d\omega$. The average kinetic and potential energy for gravity waves both equal $\frac{1}{2}\rho g\langle z^2\rangle$; hence $\rho g \mathbf{T}_\omega$ may be interpreted as the energy spectrum of gravity waves. The potential energy due to surface tension Γ may be estimated as follows. The increase of surface area due to waves is $\iint_A (\sec\beta - 1)\, dx\, dy$ and the potential energy per unit area is $(\Gamma/A)\iint (\sec\beta - 1)\, dx\, dy \approx \Gamma\sigma^2/2$. The potential energy increases linearly with σ^2 and hence is proportional to wind speed, reaching a value of 2.8 erg cm.$^{-2}$ at $W = 14$ m. sec.$^{-1}$ According to the Neumann energy spectrum (sec. **15**) this is 3×10^{-7} times the potential energy due to gravity waves under similar conditions.

It may be shown (see, for example, Rice, 1944, sec. 2) that $\mathbf{T}_\omega$ is related to the correlation by

$$\psi(0,\tau) = \int_{o}^{\infty} \mathbf{T}_\omega \cos(\omega\tau)\, d\omega \,, \quad \textbf{(13.1–6)}$$

on the assumption, verified in section **13.21**, that the space average defining ψ is equivalent to a time average.

13.2 *The directional spectrum of variance of* $z(\mathbf{r},t)$.—In contrast to measurements made at a single point in space, each measurement of the slope distribution was made at a single instant. We may connect these two types of observations by means of the wave equation.

Suppose that z and $\partial z/\partial t$ are specified at $t = 0$. Then Longuet-Higgins (1950) has shown that

$$z(\mathbf{r},t) = Re \int_0^\infty \int_{-\pi}^{\pi} A(\mathbf{k}) \exp [i(\mathbf{k} \cdot \mathbf{r} - \omega t)]\, k\, dk\, d\alpha\,, \qquad (\mathbf{13.2}\text{–}1)$$

with $k = |\mathbf{k}|$, $\mathbf{k} = (k_x,k_y) = (k \sin \alpha, k \cos \alpha)$, $\mathbf{r} = (x,y)$, and

$$A(\mathbf{k}) = (2\pi)^{-2} \int_{-s}^{s} \int_{-s}^{s} \left(z - \frac{1}{i\omega} \frac{\partial z}{\partial t}\right)_{t=0} \exp (-i\, \mathbf{k} \cdot \mathbf{r})\, dx\, dy\,, \qquad (\mathbf{13.2}\text{–}2)$$

satisfies the specified initial values within the area $|x| < s$, $|y| < s$. Equation (**13.2**–1) represents z as the sum of infinitesimal sine waves of propagation vector $\mathbf{k}$, wave length $2\pi/k$, frequency $\omega(k)$ according to the usual formula, phase velocity $C = \omega/k$, and amplitude $A(\mathbf{k})\, k\, dk\, d\alpha$, traveling in the direction of k. Each wavelet obeys the wave equation $\nabla^2 z = C^{-2}\, \partial^2 z/\partial t^2$. Hence (**13.2**–1) follows from the linearity of the wave equation. It will become a poor forecasting formula after a long time because of the limited knowledge at $t = 0$; (**13.2**–1) assumes the sea is flat for $|x| > s$, $|y| > s$ at $t = 0$. This difficulty can be eliminated by increasing the area $4s^2$ without limit. In particular, it will be shown in section **13.21** that if

$$\mathbf{S}_{\mathbf{k}} = \lim_{s \to \infty} \frac{2\pi^2 [\overline{A}(\mathbf{k})]^2}{4s^2}\,, \qquad (\mathbf{13.2}\text{–}3)$$

where $(\overline{A})^2$ is a smoothed version of $|A(\mathbf{k})|^2$ analogous to the relation between $\overline{g}^2$ and $|g|^2$, section **13.1**, then

$$\psi(\boldsymbol{\rho},\tau) = \iint_{-\infty}^{\infty} \mathbf{S}_{\mathbf{k}} \cos (\mathbf{k} \cdot \boldsymbol{\rho} - \omega\tau)\, dk_x\, dk_y\,. \qquad (\mathbf{13.2}\text{–}4)$$

The way is now open to find the connection between the frequency spectrum, $\mathbf{T}_\omega$, and the directional spectrum $\mathbf{S}_{\mathbf{k}}$. In (**13.2**–4) we change variables from (k_x,k_y) to (ω,α). Writing

$$\mathbf{S}_{\mathbf{k}}\, dk_x\, dk_y = \mathbf{S}_{\mathbf{k}}(\omega,\alpha) \left|\frac{\partial(k_x,k_y)}{\partial(\omega,\alpha)}\right| d\omega\, d\alpha\,, \qquad (\mathbf{13.2}\text{–}5)$$

where $\dfrac{\partial(k_x,k_y)}{\partial(\omega,\alpha)}$ is the Jacobian of the transformation, and setting $\boldsymbol{\rho}$ equal to zero, we have on comparison with (**13.1**–6)

$$\mathbf{T}_\omega = \int_{-\pi}^{\pi} \mathbf{S}_{\mathbf{k}}(\omega,\alpha) \left|\frac{\partial(k_x,k_y)}{\partial(\omega,\alpha)}\right| d\alpha\,. \qquad (\mathbf{13.2}\text{–}6)$$

There are two approximations inherent in the stated form of the wave equation which limit the applicability of these results: (1) nonlinear terms have been neglected, and (2) no allowance has been made for generation and decay of waves. The first error may be connected with the fact that the observed distribution of slopes showed a slight positive peakedness relative to a Gaussian distribution whereas the linear equation predicts a strictly Gaussian distribution for the statistically steady state. The second error will cause the predicted form of the sea surface to disagree with (**13.2**–1) for $t > 0$, but if the fetch and duration of the wind are sufficiently large that "equilibrium waves" are present, then the statistical behavior of the sea surface is probably represented almost correctly. Since very short waves are generated and decay most rapidly, the uncertainty of the results is greatest for large values of k and ω.

A theory avoiding the second error should account for the observed skewness in the slope distribution since this is probably the result of driving forces due to winds. In the following sections we shall omit any further discussion of these limitations.

13.21 *Relation between correlation and directional spectrum.*—We proceed to the derivation of (**13.2**–4). The method is formal, and questions regarding the justification of interchanging of limiting operations are not considered.

To evaluate the correlation (**13**–1),

$$\psi(\boldsymbol{\varrho},\tau) = \lim_{s\to\infty} \frac{1}{4s^2} \int_{-s}^{s}\int_{-s}^{s} z(\mathbf{r},t)\, z(\mathbf{r}+\boldsymbol{\varrho},t+\tau)\, dx\, dy\ ,$$

we replace the two z functions in the integrand by their respective Fourier transforms (**13.2**–1), making use of the identity:

$$Re[A\exp(i\mathbf{k}\cdot\mathbf{r}-i\omega t)] = \tfrac{1}{2}[A\ e^{i(\mathbf{k}\cdot\mathbf{r}-\omega t)} + A^{*}e^{-i(\mathbf{k}\cdot\mathbf{r}-\omega t)}]\ .$$

Then we reverse the order of integration by integrating first over x and y. This leaves a product of two double integrals, which can be written as a single quadruple integral (limits $\pm\infty$) over the four wave numbers $k_x,k_y;\ k_x',k_y'$. The unprimed parameters go with $z(\mathbf{r},t)$, the primed parameters with $z(\mathbf{r}+\boldsymbol{\varrho},\ t+\tau)$. The result of this integration is

$$\begin{aligned}\psi = \lim_{s\to\infty}\frac{1}{4}\int_{-\infty}^{\infty}\!\!\iiint \Big\{ & A(\mathbf{k})\ A(\mathbf{k}')\exp[i(\mathbf{k}'\cdot\boldsymbol{\varrho}-\omega'\tau-(\omega+\omega')t)] \\ & + A^{*}(\mathbf{k})\ A^{*}(\mathbf{k}')\exp[-i(\mathbf{k}'\cdot\boldsymbol{\varrho}-\omega'\tau-(\omega+\omega')t)]\Big\}\ F^{+}\ d\mathbf{k}\ d\mathbf{k}' \\ + \lim_{s\to\infty}\frac{1}{4}\int_{-\infty}^{\infty}\!\!\iiint \Big\{ & A^{*}(\mathbf{k})\ A(\mathbf{k}')\exp[i\mathbf{k}'\cdot\boldsymbol{\varrho}-\omega'\tau+(\omega-\omega')t)] \\ & + A(\mathbf{k})\ A^{*}(\mathbf{k}')\exp[-i(\mathbf{k}'\cdot\boldsymbol{\varrho}-\omega'\tau+(\omega-\omega')t)]\Big\}\ F^{-}\ d\mathbf{k}\ d\mathbf{k}'\ . \quad (\mathbf{13.2}\text{–}7)\end{aligned}$$

The factors

$$F^{\pm} = \frac{\sin s(k_x \pm k_x') \sin s(k_y \pm k_y')}{s^2(k_x \pm k_x')(k_y \pm k_y')}$$

are sharply peaked near $\mathbf{k}' = \mp\mathbf{k}$, and converge rapidly on zero for $\mathbf{k}'$ diverging from $\mathbf{k}$, for large s. Consequently almost all the contributions to the integrations over $\mathbf{k}'$ occur near these peaks. It is plausible that the results of these integrations are given by making the substitution $\mathbf{k}' = \mathbf{k}$ and $\omega' = +\omega$ *inside* the braces and integrating only over the factors $F^{\pm}$. Although this procedure is only approximately correct for finite s, the accuracy improves as s increases. Noting that $\int\int F^{\pm}\, d\mathbf{k}' = \pi^2/s^2$ one finds that

$$\psi = 2\pi^2 \int\int_{-\infty}^{\infty} \left\{ \frac{A(\mathbf{k})\, A(-\mathbf{k})}{4s^2} \cos\left[\mathbf{k} \cdot \boldsymbol{\varrho} + \omega(\tau + 2t) - \phi_{\mathbf{k}} - \phi_{-\mathbf{k}}\right] + \frac{|A(\mathbf{k})|^2}{4s^2} \cos(\mathbf{k} \cdot \boldsymbol{\varrho} - \omega\tau) \right\} d\mathbf{k} \qquad \textbf{(13.2–8)}$$

nearly, where $A(\mathbf{k}) = |A(\mathbf{k})| \exp(i\phi_{\mathbf{k}})$. Because the phases $\phi_{\mathbf{k}}$ and $\phi_{-\mathbf{k}}$ of oppositely directed waves are random, the contribution to (**13.2**–8) by the first term of the integrand is negligible compared to the second. At great depths, the relative importance of the two terms will be interchanged when the area $4s^2$ covered by waves is finite. This leads to the double-frequency oscillations discussed by Longuet-Higgins (1950) in his study of microseisms. In the second term the factor $|A(\mathbf{k})|^2/4s^2$ oscillates rapidly with $\mathbf{k}$ for large s. However, the value of the integral is not changed if we replace this expression by $(\bar{A})^2/(4s^2)$, a smoothed version obtained by averaging over an arbitrarily small but finite range of $\mathbf{k}$ (sec. **13.1**). In the limit

$$2\pi^2 [\bar{A}(\mathbf{k})]^2/(4s^2) \rightarrow \mathbf{S}_{\mathbf{k}} \qquad \textbf{(13.2–9)}$$

and

$$\psi(\boldsymbol{\varrho}, \tau) = \int\int_{-\infty}^{\infty} \mathbf{S}_{\mathbf{k}} \cos(\mathbf{k} \cdot \boldsymbol{\varrho} - \omega\tau)\, dk_x\, dk_y\,. \qquad \textbf{(13.2–10)}$$

This is the desired relation. Under the present assumption of random phase, the first part of (**13.2**–7) vanished and hence ψ is *not* a function of time t. If it were, then spatial averages would have differed from time averages contrary to the usual ergodic hypothesis for statistically uniform conditions.

13.3 *Slope spectra and mean square slopes.*—The relation (**13.2**–4) between the correlation and the directional spectrum permits the comparison of spatial observations (such as the slope distribution as determined by sun-glitter observations) with records obtained at a single point. For slopes, the relationship is derived as follows: The equation defining the correlation may be written

$$\psi(\xi, \eta, \tau) = \langle z(x,y,t)\, z(x + \xi, y + \eta, t + \tau) \rangle\,, \qquad \textbf{(13.3–1)}$$

where ξ, η are components of the separation vector ϱ in (**13**–1). Following Eckart (1953) we differentiate (**13.3**–1) to obtain

$$\left.\begin{aligned} -\frac{\partial^2\psi}{\partial\xi^2} &= \langle z_x(x,y,t)z_x(x+\xi,y+\eta,t+\tau)\rangle = \iint_{-\infty}^{\infty} k_x^2\mathbf{S}_\mathbf{k}\cos(\mathbf{k}\cdot\varrho-\omega\tau)dk_x\,dk_y, \\ -\frac{\partial^2\psi}{\partial\eta^2} &= \langle z_y(x,y,t)z_y(x+\xi,y+\eta,t+\tau)\rangle = \iint_{-\infty}^{\infty} k_y^2\mathbf{S}_\mathbf{k}\cos(\mathbf{k}\cdot\varrho-\omega\tau)dk_x\,dk_y. \end{aligned}\right\} \quad (\mathbf{13.3}\text{–}2)$$

In comparison with (**13.2**–4) it will be seen that $k_x^2\mathbf{S}_\mathbf{k}$ and $k_y^2\mathbf{S}_\mathbf{k}$ are the spectra of the slope components z_x and z_y. For the case $\xi = \eta = \tau = 0$ (**13.3**–2) reduces to

$$\langle z_x^2\rangle = \iint_{-\infty}^{\infty} k_x^2\mathbf{S}_\mathbf{k}\,dk_x\,dk_y\ ; \qquad \langle z_y^2\rangle = \iint_{-\infty}^{\infty} k_y^2\mathbf{S}_\mathbf{k}\,dk_x\,dk_y\ . \qquad (\mathbf{13.3}\text{–}3)$$

With the y-axis pointing upwind, these are the crosswind and up/downwind components of mean square slopes, σ_c^2 and σ_u^2. On changing to the variables k,α' one obtains finally

$$\sigma_c^2 = \int_o^\infty\int_{-\pi}^{\pi} k^2\sin^2\alpha'\ \mathbf{S}_\mathbf{k}\,k\,dk\,d\alpha'\ , \qquad \sigma_u^2 = \int_o^\infty\int_{-\pi}^{\pi} k^2\cos^2\alpha'\ \mathbf{S}_\mathbf{k}\,k\,dk\,d\alpha', \quad (\mathbf{13.3}\text{–}4)$$

and

$$\sigma^2 = \sigma_c^2 + \sigma_u^2 = \iint_{-\infty}^{\infty} k^2\mathbf{S}_\mathbf{k}\,dk_x\,dk_y = \int_o^\infty k^2\mathbf{T}_\omega\,d\omega\ . \qquad (\mathbf{13.3}\text{–}5)$$

The last expression follows from (**13.2**–5, –6).

13.4 *Curvature spectrum and mean square curvature.*—The *mean curvature* at a point on a surface is defined as the sum of the two principal radii of curvature at the point. The *total*, or *Gaussian, curvature* is the product of the principal radii of curvature. The statistics of the mean curvature are related to the spectrum $\mathbf{T}_\omega$, but description of the total curvature needs the more complete information inherent in the directional spectrum $\mathbf{S}$. For our purposes a prediction of the mean of the *mean* curvature squared will be sufficient.

It may be shown that the value of the mean curvature is given by

$$\begin{aligned} \kappa = z_{xx}\cos\beta(1-\cos^2\alpha\sin^2\beta) - 2z_{xy}\sin\alpha\cos\alpha\sin^2\beta\cos\beta \\ + z_{yy}\cos\beta(1-\sin^2\alpha\sin^2\beta)\ . \end{aligned}$$

For small β this reduces to

$$\kappa \approx z_{xx} + z_{yy}\ . \qquad (\mathbf{13.4}\text{–}1)$$

The mean square of κ may be found by differentiating (**13**–1) with respect to ξ and η, the (x,y) components of ϱ. This yields

$$\left(\frac{\partial^2}{\partial\xi^2} + \frac{\partial^2}{\partial\eta^2}\right)^2 \psi(0,0,0) = \langle(z_{xx} + z_{yy})^2\rangle = \langle\kappa^2\rangle \,. \qquad (\mathbf{13.4}\text{–}2)$$

The process is similar to the derivation of (**13.3**–2). By use of (**13.2**–5, –6) this becomes

$$\langle\kappa^2\rangle = \int_o^\infty k^4 \mathbf{T}_\omega \, d\omega \,. \qquad (\mathbf{13.4}\text{–}3)$$

13.5 *A summary of useful relations.*—In terms of the frequency spectrum $\mathbf{T}_\omega$ the mean square elevation, slope, and curvature are, respectively,

$$\langle z^2\rangle = \int_o^\infty \mathbf{T}_\omega \, d\omega \,, \qquad (\mathbf{13.5}\text{–}1)$$

$$\sigma^2 = \int_o^\infty k^2 \mathbf{T}_\omega \, d\omega \,, \qquad (\mathbf{13.5}\text{–}2)$$

$$\langle\kappa^2\rangle = \int_o^\infty k^4 \mathbf{T}_\omega \, d\omega \,. \qquad (\mathbf{13.5}\text{–}3)$$

Equations (**13.5**–2, –3) may be regarded as definitions of the (frequency) spectra of slope, $k^2\mathbf{T}_\omega$, and of curvature, $k^4\mathbf{T}_\omega$, respectively. The components of mean square slope are

$$\sigma_c^2 = \int_o^\infty \int_{-\pi}^{\pi} k^2 \sin^2\alpha' \, \mathbf{S}_\mathbf{k} \, k \, dk \, d\alpha', \quad \sigma_u^2 = \int_o^\infty \int_{-\pi}^{\pi} k^2 \cos^2\alpha' \, \mathbf{S}_\mathbf{k} \, k \, dk \, d\alpha' \qquad (\mathbf{13.5}\text{–}4)$$

where α' is the angle between the propagation vector $\mathbf{k}$ and the wind, and $\mathbf{S}_\mathbf{k}$, the directional spectrum, is related to the frequency spectrum by (**13.2**–6)

$$\mathbf{T}_\omega = \int_{-\pi}^{\pi} \mathbf{S}_\mathbf{k}(\omega,\alpha') \left|\frac{\partial(k_x,k_y)}{\partial(\omega,\alpha)}\right| d\alpha' \,.$$

It is sometimes convenient to make use of the period spectrum $\mathbf{T}_T$, which is related to the frequency spectrum by

$$\mathbf{T}_\omega \, d\omega = \mathbf{T}_T \, dT \,. \qquad (\mathbf{13.5}\text{–}5)$$

The wave number k is related to frequency ω, period t, and wave length L

according to

$$\left.\begin{aligned} \omega &= 2\pi/T, \qquad k = 2\pi/L, \\ \omega^2 &= gk + \gamma k^3, \end{aligned}\right\} \tag{13.5–6}$$

with γ designating surface tension divided by density (74 cm.^{3} sec.$^{-2}$ for clean water). According to (**13.5**–6) the phase velocity reaches a minimum value

$$C_{min} = \omega_m/k_m = (4g\gamma)^{\frac{1}{2}} \tag{13.5–7}$$

when

$$\omega_m = (4g^3/\gamma)^{\frac{1}{4}}, \qquad k_m = (g/\gamma)^{\frac{1}{2}}.$$

Numerical values are $C_{min} = 23$ cm. sec.$^{-1}$, $T_m = 0.074$ sec., $L_m = 1.7$ cm.

Waves much larger than L_m are gravity waves and for these

$$\omega^2 \approx g\,k\,. \tag{13.5–8}$$

Waves much shorter are capillary waves, and

$$\omega^2 \approx \gamma k^3\,. \tag{13.5–9}$$

14. "Beam Width" of the Trade-Wind Sea

The problem is to learn something concerning the dependence of $\mathbf{S_k}$ upon α' from the observed ratio σ_c^2/σ_u^2. The relationship linking these quantities is (**13.5**–4). In the absence of any information whatsoever concerning the directionality of different frequency components, we may assume waves of all periods have the same direc-

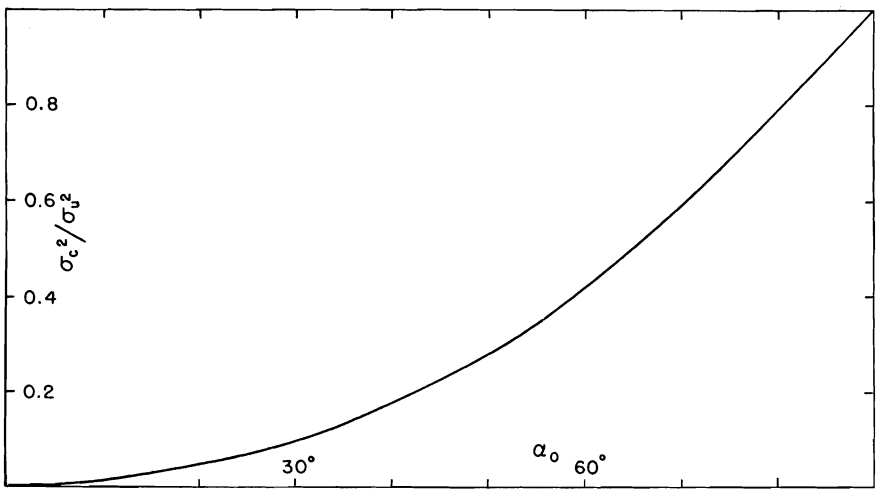

Fig. 18. Half-beam width of wave directions, α_o, as a function of the ratio of mean square slope components, σ_c^2/σ_u^2. It is assumed that waves of all periods have the same beam width.

tionality. We shall consider two cases. For a single beam pattern of width $2\alpha_o$ we set

$$\mathbf{S_k} = \begin{cases} F(k) & \text{if} \quad -\alpha_o < \alpha' < \alpha_o \\ 0 & \text{otherwise.} \end{cases}$$

This gives

$$\sigma_c^2 = (\alpha_o - \tfrac{1}{2}\sin 2\alpha_o)\int_o^\infty F(k)k^3\,dk, \quad \sigma_u^2 = (\alpha_o + \tfrac{1}{2}\sin 2\alpha_o)\int_o^\infty F(k)k^3\,dk\,,$$

and

$$\frac{\sigma_c^2}{\sigma_u^2} = \frac{2\alpha_o - \sin 2\alpha_o}{2\alpha_o + \sin 2\alpha_o}. \tag{14-1}$$

For narrow beam width this reduces to $\alpha_o^2/3$. The function is plotted in figure 18.

For two infinitely narrow crossbeams intersecting at an angle $2\alpha_o$ we set

$$\mathbf{S_k} = \begin{cases} F(k) & \text{for} \quad \alpha = -\alpha_o, \alpha = +\alpha_o \\ 0 & \text{otherwise.} \end{cases}$$

This yields simply

$$\frac{\sigma_c^2}{\sigma_u^2} = \tan^2 \alpha_o \quad . \tag{14-2}$$

The corresponding values are given in table 2. For a trade-wind sea the single broad beam is believed to conform more nearly to actual conditions. The corresponding beam width is remarkably wide. These values, though based heavily on

TABLE 2

BEAM WIDTHS, AND ANGULAR SPREAD BETWEEN TWO INTERSECTING BEAMS, LEADING TO OBSERVED RATIOS OF CROSSWIND AND UP/DOWNWIND SLOPE COMPONENTS

	Min.	Mean	Max.	Slick (mean)
Ratio, σ_c^2/σ_u^2	0.54	0.75	1.0	0.86
$2\alpha_o$, single beam	134°	157°	180°	167°
$2\alpha_o$, two narrow crossbeams	72°	82°	90°	86°

simplifying assumptions, are nevertheless of interest, as they are believed to represent the first measurements of the directionality of ocean waves. It was shown in section **10.3** that the maximum ratio $\sigma_c^2/\sigma_u^2 = 1.0$ can be interpreted as due to the unsteadiness of the wind field. The angles referring to the *minimum* ratio can be considered as the *maximum* beam width of the longer waves since these waves are not affected by rapid fluctuations of wind direction.

15. Spectra Proposed by Darbyshire and Neumann

Darbyshire (1952) has proposed a spectrum of the variance of z equivalent to

$$\mathbf{T}_T = c'T^2 \exp\left[-2.0\left(\frac{gt}{U} - 4.6\right)^2\right] \qquad (15\text{–}1$$

where c' has the value 22 cm.^{2} sec.$^{-3}$, and U is the gradient wind speed equal on the average to one and one-half times the masthead wind speed, W.

The spectrum was obtained by frequency-analyzing pressure records of waves generated by local storms at Lands End, England. Only those storm records were analyzed for which the fetch was sufficient to generate equilibrium waves. The bottom pressure transducer was usually located at a depth of 50 feet. The usual hydrodynamic relationship had then to be used to convert bottom pressure to surface elevation. For wave periods less than six seconds the bottom pressure oscillations, reduced to such a low level that the process was no longer practicable,were ignored by Darbyshire. But it will be shown that these waves contribute about five-sixths of the total wave energy and that consequently Darbyshire's spectrum is too narrow and total energy too small (fig. 19). A pressure recorder at 50 feet is evidently not a suitable instrument for obtaining the energy spectrum.

On the basis of visual observations of fully developed waves in a storm area, Neumann (1953) proposes a spectrum (fig. 19)

$$\mathbf{T}_T = \frac{1}{8} c \left(\frac{gT^2}{2\pi}\right)^2 \exp\left[-2\left(\frac{gT}{2\pi W}\right)^2\right], \qquad (15\text{–}2)$$

where W is the wind speed, and

$$c = 0.827 \times 10^{-3} \text{ sec.}^{-1}. \qquad (15\text{–}3)$$

It is of interest to compare the Darbyshire and Neuman spectra. The periods corresponding to the maximum value of $\mathbf{T}_T$ are

$$4.7\, g^{-1} U \approx 7.1\, g^{-1} W, \qquad 2\pi\, g^{-1} W, \qquad (15\text{–}4)$$

respectively, and in reasonable agreement. The mean square elevations, however, follow different laws:

$$6.4 \times 10^{-5} \text{ cm.}^{-1} \text{ sec.}^3\, U^3, \qquad 3.2 \times 10^{-12} \text{ cm.}^{-3} \text{ sec.}^5\, W^5 \quad . \qquad (15\text{–}5)$$

If the observations in Darbyshire's figure 7 are fitted to Neumann's formula and $\langle z^2 \rangle$ is assumed proportional to W^5, it is found that $c = 0.3 \times 10^{-3}$ sec.$^{-1}$, compared to Neumann's value 0.8×10^{-3}. The small value presumably reflects the lack of information on wave periods less than $T_1 = 6$ sec. It may be corrected as follows:

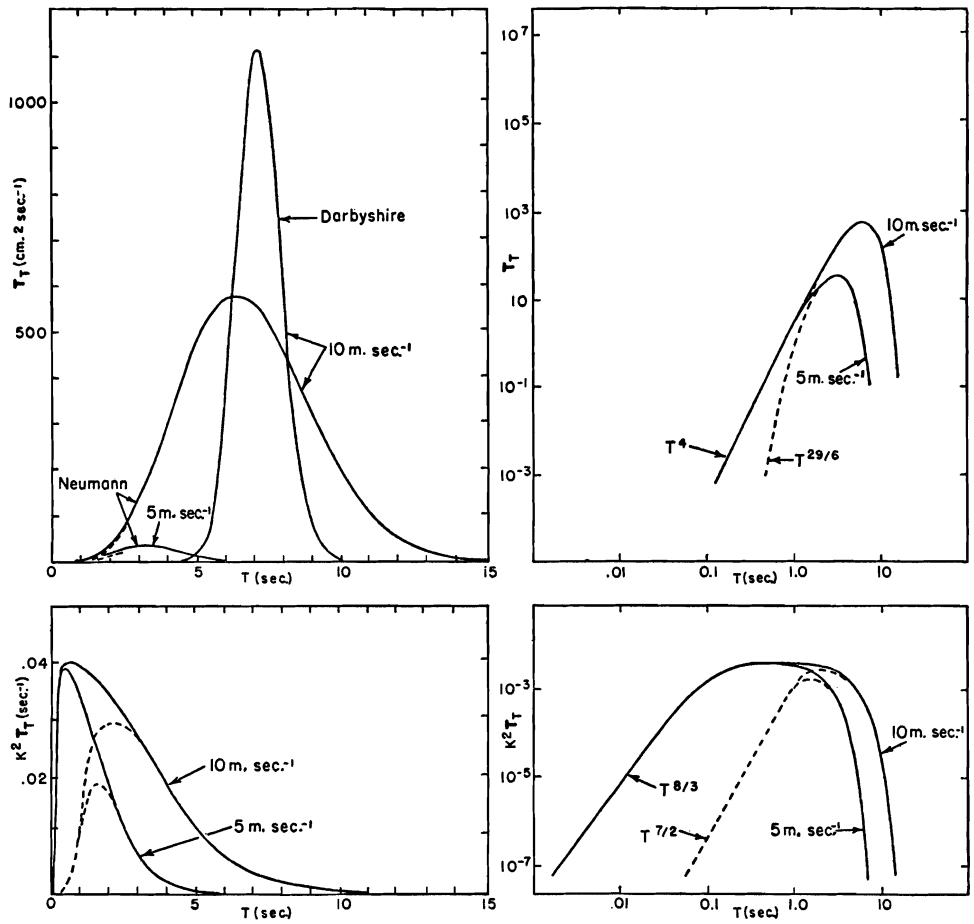

Fig. 19. Period spectra of variance of sea-surface elevation (upper panels) and of slope regardless of direction (lower panels). The left panels are drawn on a linear scale, the right panels on a double logarithmic scale. The asymptotic behavior for high frequencies is indicated. Curves refer to wind speeds of 5 and 10 m. sec.$^{-1}$ as noted. Solid lines apply to clean sea surface, dashed lines to slick surface. The variance of the $z(t)$ spectrum proposed by Darbyshire is illustrated on the upper left panel; all other curves are derived from Neumann's spectrum.

Assume Neumann's spectrum (**15**–2). The contribution of waves having periods greater than T_1 to the mean square elevation is

$$\langle z^2\rangle_{T>T_1}=\int_{T_1}^{\infty}\mathbf{T}_T dT=\left(\frac{g}{2\pi}\right)^2\frac{c}{8}\left\{\tfrac{1}{2}T_1{}^3V^2\left(1+\frac{3}{2}\frac{V^2}{T_1{}^2}\right)e^{-T_1^2/V^2}+\frac{3}{8}V^5\pi^{\frac{1}{2}}\left[1-H\left(\frac{T_1}{V}\right)\right]\right\},\tag{15–6}$$

where $V=\pi 2^{\frac{1}{2}}g^{-1}W$ and $H(x)=2\pi^{-\frac{1}{2}}\int_0^x e^{-t^2}dt$ is the error integral.

Entering (**15**–6) with appropriate values of W and $\langle z^2\rangle_{T>T_1}$ from Darbyshire's data, and setting $T_1=6$ seconds, we obtain $c=2\times10^{-3}$ sec.$^{-1}$ with very large scatter, compared to the previous value of 0.3×10^{-3} sec.$^{-1}$ (uncorrected for the high-frequency cutoff) and Neumann's value 0.8×10^{-3} sec.$^{-1}$

15.1 *The slope spectrum and mean square slope.*—The mean square slope regardless of direction, σ^2, can be computed from $\mathbf{T}_T$ according to (**13.5**–2, –5). *Neglecting capillary waves*, the spectra proposed by Darbyshire and Neumann yield, respectively,

$$\sigma^2 = (2\pi)^4 \sqrt{\tfrac{1}{2}\pi}\, (4.6)^{-2}\, c'(gU)^{-1} = 1.0\, W^{-1}\,, \qquad (\mathbf{15.1}\text{–}1)$$

$$\sigma^2 = \tfrac{1}{2}\pi^3 \sqrt{\tfrac{1}{2}\pi}\, c\, g^{-1}\, W \qquad = 1.65 \times 10^{-5}\, W\,, \qquad (\mathbf{15.1}\text{–}2)$$

where W is in cm. sec.$^{-1}$ The observations (sec. **9.1**) gave

$$\sigma^2 = 5.12 \times 10^{-5} W + 0.003 \pm 0.004\,, \qquad (\mathbf{15.1}\text{–}3)$$

for clean sea surface, and

$$\sigma^2 = 1.56 \times 10^{-5} W + 0.008 \pm 0.004\,, \qquad (\mathbf{15.1}\text{–}4)$$

for slick surface.

The Darbyshire spectrum predicts that the mean square slope *decreases* with increasing wind speed, contrary to our observations. For $W = 10$ m. sec.$^{-1}$, $\sigma^2 = 10^{-3}$ compared to the observed value $(54 \pm 4) \times 10^{-3}$. Clearly the spectrum proposed by Darbyshire has too little energy in the short waves. As noted earlier, this is not surprising since waves having periods shorter than six seconds could not have been observed.

The important result is that Neumann's spectrum yields the observed linear relation between mean square slope and wind speed. (This was mentioned by W. J. Pierson, Jr., in a paper delivered before the American Geophysical Union, May, 1953.) Furthermore, the computed proportionality constant agrees with the measurements over slicks, but is one-third the value required to account for the clean surface. If we take the value $c = 2 \times 10^{-3}$ sec.$^{-1}$ on the basis of Darbyshire's data corrected for high-frequency cutoff, the result is

$$\sigma^2 = 4 \times 10^{-5}\, W \text{ (c.g.s.)}\,.$$

A generalization of Neumann's spectrum of the form

$$\mathbf{T}_T \sim T^m \exp\,[-(T/W)^n]$$

yields

$$\sigma^2 \sim W^{m-3}\, n^{-1}\, \Gamma\left(\frac{m-3}{n}\right)$$

and hence σ^2 will be proportional to W only if $m = 4$, as assumed by Neumann. Neumann states that his data is convincingly better in accord with $\mathbf{T}_T \sim T^4$ than with T^3 or T^5. There must, of course, be other analytic functions which also yield $\sigma^2 \sim W$. Nevertheless, the consistency of Neumann's result with the present measurements is encouraging.

A slight modification to the linear relation (**15.1**–2) results from considering capillary waves. Although Neumann's spectrum was intended to represent only gravity waves, the procedure adopted here is to extend his spectrum without alteration into the capillary range. In this range the *slope* spectrum decreases with decreasing T like $T^{8/3}$ instead of remaining constant (fig. 19), so that the mean square slope must be less than that given by (**15.1**–2).

It is no longer possible to obtain the integral for σ^2 in closed form. We have, however, derived analytic solutions for the two asymptotic cases, $W \ll C_{min}$ and $W \gg C_{min}$, and integrated the intermediary part by numerical methods. The resulting mean square slope is $\sigma^2[1 - 2.28\pi^{-\frac{1}{2}}(C_{min}/W)]$ where σ^2 is the solution (**15.1**–2) when capillarity is neglected. The numerical value of the correction term, $-2.28\pi^{-\frac{1}{2}}\sigma^2(C_{min}/W)$, is $-.0005$. The measured intercept (**15.1**–3) is $+0.003 \pm 0.004$. The modification is evidently smaller than the uncertainty in the empirical relations.

15.2 *Curvature spectrum.*—In the preceding section it has been found that the Neumann spectrum gives nearly a satisfactory account of the observed distribution of slopes. One is tempted to find what it predicts about the distribution of curvatures. Since curvature is heavily weighted in favor of the very short waves, this prediction must be viewed as very uncertain. Conversely, observations of curvature may provide a powerful method for studying the high-frequency tail of the spectrum.

The curvature spectrum $k^4\mathbf{T}_T$ is nearly peaked at T_m, and hence capillary and gravity waves contribute about equally. The mean square curvature can be computed in three parts.

Let

$$\kappa_o^2 = \tfrac{1}{2}\pi^3 c\, g^{1/4}\gamma^{-3/4}\,. \qquad (\mathbf{15.2}\text{–}1)$$

Then for the capillary, intermediary, and gravity portions of the spectrum the contributions are

$$\kappa_c^2 = \int_o^{1/5Tm} k^4\mathbf{T}_T dT = (3/7)\, 2^{-1/6}\, 5^{-7/3}\, \kappa_o^2 = 0.0090\, \kappa_o^2\,,$$

$$\kappa_i^2 = \int_{1/5Tm}^{5Tm} k^4\mathbf{T}_T dT = I\, \kappa_o^2 = 4.89\, \kappa_o^2\,,$$

$$\kappa_g^2 = \int_{5Tm}^{\infty} k^4\mathbf{T}_T dT \approx (4/3)\, 2^{\frac{1}{2}}\, 5^{-3}\left[1 - \frac{3}{2}(5C_{min}/W)^2\right]\kappa_o^2$$

$$= 0.015[1 - 37.5(C_{min}/W)^2]\,\kappa_o^2\,;$$

where

$$I = \tfrac{1}{2}\int_{(1/5)^4}^{(5)^4} y^{-1/4}(1 + 3y)(1 + y)^{-7/2}\, dy$$

has been evaluated numerically. In the evaluation of κ_g^2 it was assumed that $W \gg C_{min}$. The total mean square curvature is

$$4.9\kappa_o^2 = \begin{cases} .014 \text{ cm.}^{-2} \\ .034 \text{ cm.}^{-2} \end{cases} \qquad \textbf{(15.2–2)}$$

The upper number refers to $c = 8.27 \times 10^{-4}$ sec.$^{-1}$ (Neumann), the lower to $c = 2 \times 10^{-3}$ sec.$^{-1}$ (Darbyshire's data modified for high-frequency cutoff). The corresponding principal radii of curvature are 12 cm. and 8 cm. almost independent of wind speed; the diameters of the sun's image formed by the sea surface would be roughly 0.5 mm. and 0.3 mm.

15.3 *Acceleration spectrum.*—The horizontal acceleration of an elementary wave train $A \cos (kx - \omega t)$ has an amplitude $\omega^2 A$ at the sea surface. For gravity waves this equals gkA. The slope has an amplitude kA. Except for a minor contribution from capillaries, *the distributions of acceleration (in units of g) and of slope (in radians) are equivalent.* (This was pointed out by N. F. Barber in a personal communication.) To this approximation,

$$a_c^2 = \sigma_c^2, \qquad a_u^2 = \sigma_u^2, \qquad \textbf{(15.3–1)}$$

where a_c^2 and a_u^2 are the crosswind and up/downwind components of the mean square acceleration (in units of g) at the sea surface. The mean square horizontal acceleration regardless of direction is therefore

$$a_h^2 = a_c^2 + a_u^2 = \sigma^2 . \qquad \textbf{(15.3–2)}$$

The mean square vertical acceleration a_v^2 for deep-water waves equals the horizontal, and the mean square acceleration in all three directions is therefore

$$a^2 = a_h^2 + a_v^2 = 2\sigma^2 . \qquad \textbf{(15.3–3)}$$

Preceding results regarding the slope distribution can be applied immediately. Thus the up/downwind component exceeds the crosswing component of mean square acceleration by a factor of 1.3, on the average; all mean square accelerations increase linearly with wind, and the total r.m.s. acceleration at a wind speed of 14 m. sec.$^{-1}$ is 0.4 g!

The horizontal acceleration spectrum is

$$\omega^4 \mathbf{T}_T , \qquad \textbf{(15.3–4)}$$

and the mean square acceleration

$$a_h^2 = \int_o^\infty \omega^4 \mathbf{T}_T dT = \pi^3 \sqrt{\tfrac{1}{2}\pi} \frac{cW}{g} \approx \sigma^2 \qquad \textbf{(15.3–5)}$$

varies *exactly* in proportion to wind speed according to the Neumann spectrum.

16. Effect of Slicks

We wish to consider whether it is possible to account for the observed reduction by a factor of two or three of the mean square slopes. The method will in a sense be the opposite of that in section **13.2**. There a statistical balance between generation and decay was assumed. Here no generation and full decay by laminar processes is proposed.

According to Reynolds' classical theory (Lamb, 1945, art. 351), the effect of an *inextensible* surface film is to annul the horizontal velocity at the surface. This leads to a modulus of decay of

$$\tau = 2^{3/2}\nu^{-\frac{1}{2}}k^{-1}\omega^{-\frac{1}{2}}, \qquad (\mathbf{16}\text{–}1)$$

where ν is the kinematic viscosity. In the actual case, the film will be somewhat extensible, and the foregoing expression may be regarded as an upper limit to the effectiveness of a surface active agent. The reduction in (amplitude)^2 for each spectral component is exp $(-2t/\tau)$, where t is the length of time since the wave has entered the slick. The time required to cross a slick of length s is $t' = sk/\omega$, and the mean reduction (sampled by a photograph of the entire slick) is

$$F = \frac{1}{t'}\int_0^{t'} e^{-t/(2\tau)}\,dt = \alpha(1 - e^{-1/\alpha}), \qquad (\mathbf{16}\text{–}2)$$

where

$$\alpha = (2\omega)^{\frac{1}{2}}s^{-1}\nu^{-\frac{1}{2}}k^{-2} = 2.11 \times 10^{-4}k^{-2}\omega^{\frac{1}{2}}\ \text{(c.g.s.)}$$

for a slick 500 m. in length. For $\alpha \gg 1$, $F \approx 1$, and for $\alpha \ll 1$, $F \approx \alpha$. Combining (**16**–2) with $\omega(k)$ leads to $F(T)$. This reduction factor has been applied to the (amplitude)^2 and (slope)^2 spectra, as shown in figure 19 (sec. **15**). For waves of 0.5 sec. period (1 ft. length) each spectrum is reduced by a factor of 100 (amplitude by a factor of 10), and waves shorter than this are thus essentially eliminated. This is in reasonable accord with visual observations. As is to be expected, the mean square amplitude is hardly affected by this "high-frequency cutoff," whereas the mean square curvature is greatly reduced. The latter feature may account for the pronounced optical effect. The effect on the mean square slope falls between these extremes.

The mean square slope in the presence of slicks is $\int_0^\infty F\,k^2\mathbf{T}_T dT$, and equals

$$0.40 \times 10^{-2}, \qquad 1.13 \times 10^{-2}$$

for wind speeds of 5 m. sec.$^{-1}$ and 10 m. sec.$^{-1}$ respectively. The corresponding ratios in mean square slope with slick as compared to a clean surface are

$$(0.40/0.82) = 0.48, \qquad (1.13/1.65) = 0.68\,.$$

The observations give

$$0.55\,, \qquad 0.44\,.$$

These numerical values show a rough agreement between the observed decrease in mean square slope within the slick and that computed on the basis of Reynolds' classical theory. But there remain some serious difficulties. Reynolds' theory presumes a (horizontally) inextensible surface film such as one would expect to find for a monomolecular layer, or for layers a few molecules thick at most. On the other hand, the thickness of the artificial slicks is estimated to be of the order of 10^{-4} cm., or 1,000 molecules. This estimate follows from considerations involving the known size of slick and volume of oil, and from the occasional appearance of interference colors.

It is possible, however, that the oil film had an adsorbed monolayer at the air-oil or oil-water interface, or a crystallike organization at the surface which would withstand static forces (Hennicker, 1949). The compressional strength of such a layer would be the difference between the surface tension of a clean interface ($\approx$40 dynes cm.$^{-1}$ for oil-water) and the surface tension of the contaminated surface (>0 dynes cm.$^{-1}$). The following calculation shows that this would not be sufficient to annul the surface orbital velocities.

The x,y components of stress induced in the film by horizontal shear in the orbital velocity just below the film are

$$p_{xz} = \mu\left(\frac{\partial w}{\partial x} + \frac{\partial u}{\partial z}\right), \qquad p_{yz} = \mu\left(\frac{\partial w}{\partial y} + \frac{\partial v}{\partial z}\right)$$

where u,v,w are the x,y,z components of orbital velocity of the waves, μ is the viscosity, and the derivatives are to be evaluated at the surface. Let $\mathbf{p}$ be the vector shear whose components are p_{xz} and p_{yz}. For a single infinitesimal sine wave in the direction $\mathbf{k}$ (unit vector $\mathbf{k}_1$),

$$Re\, A \exp\left[i(\mathbf{k}\cdot\mathbf{r} - \omega t)\right] k\, dk\, d\alpha\,,$$

the appropriate formula is (Lamb, 1945, arts. 349 and 351)

$$\mathbf{p} = \mathbf{k}_1\omega^{3/2}(\rho\mu)^{\frac{1}{2}}\, Re\left\{A \exp\left[i\left(\mathbf{k}\cdot\mathbf{r} - \omega t - \frac{\pi}{4}\right)\right] k\, dk\, d\alpha\right\}.$$

Consider two points, $\mathbf{r}_1$ and $\mathbf{r}_2$, and let $\Delta\mathbf{r} = \mathbf{r}_2 - \mathbf{r}_1$. Then if there is no shear strength in the film, the scalar

$$F_{12} = \int_{\mathbf{r}_2}^{\mathbf{r}_1} \mathbf{p}\cdot d\mathbf{r}$$

is the *difference* in tension between the two points. For the single sine wave this gives

$$F_{12} = 2\omega^{3/2}(\rho\mu)^{\frac{1}{2}} k^{-1} \sin\left(\tfrac{1}{2}\mathbf{k}\cdot\Delta\mathbf{r}\right) Re\left\{A \exp i\left(\mathbf{k}\cdot\mathbf{r} - \omega t - \frac{\pi}{4}\right) k\, dk\, d\alpha\right\}.$$

For a continuous spectrum of waves, a calculation similar to that in section **13.21** yields for the mean square tension

$$\langle F_{12}{}^2 \rangle = 4\rho\mu \iint \omega^3 k^{-2} \sin^2 (\tfrac{1}{2}\mathbf{k} \cdot \boldsymbol{\Delta}\mathbf{r})\, \mathbf{S}_{\mathbf{k}} k\, dk\, d\alpha .$$

For sufficiently large values of $\boldsymbol{\Delta}\mathbf{r}$ the $(\sin)^2$ factor oscillates rapidly and may be replaced by its average value, $\frac{1}{2}$, and the integral over α performed:

$$\langle F_{\infty}{}^2 \rangle = 2\rho\mu \int_o^{\infty} \omega^3 k^{-2}\, \mathbf{T}_T\, dT .$$

Assuming the Neumann spectrum for $\mathbf{T}_T$ and setting $\omega^3 k^{-2} = g^2 \mathrm{T}/2\pi$ (gravity waves),

$$\langle F_{\infty}{}^2 \rangle = \rho\mu \frac{(2\pi)^3 c W^6}{32 g^2} = 6 \times 10^7 \left(\frac{W}{10 \text{ m. sec.}^{-1}} \right)^6 (\text{dyne cm.}^{-1})^2 .$$

The required strength is therefore far in excess of 40 dynes cm.$^{-1}$ But the large value reflects primarily the stresses due to the long-period waves. To estimate the longest waves which will not frequently rupture the film, one may set

$$2\rho\mu \int_o^{T_{max}} \omega^3 k^{-2}\, \mathbf{T}_T\, dT = (40 \text{ dyne cm.}^{-1})^2 .$$

Neglecting capillary waves, one finds

$$T_{max} = (24)^{1/6} (2\pi)^{\frac{1}{2}} (\rho g^4/c)^{-1/6} (40 \text{ dyne cm.}^{-1})^{1/3} = 0.7 \text{ sec.}$$

The principal reduction in σ^2 by slicks has been attributed to waves of period greater than 0.7 sec. (fig. 19; see sec. **15**). This is rendered unlikely by the present computation.

No allowance for generation and decay (other than by molecular processes) has been made in the present calculation. An alternate hypothesis for the effectiveness of slicks is that they damp only high-frequency wave components and that in absence of these components the balance between generation and decay is thrown in favor of decay for low-frequency components. This matter needs further investigation.

PART III: APPLICATION

As a result of the measurements of sea-surface slopes, certain oceanographic problems have become accessible to numerical treatment. In these problems one is concerned with the *average* radiance of the sea surface due to sun or sky, viewed from above or beneath. The average is formed over sufficient time or surface area to smooth out fluctuations such as the ones resulting from individual glitter sparkles of sunlight. The average is then essentially independent of time, but varies smoothly with the azimuth and elevation of the portion of sea surface under consideration.

Let $z(x,y)$ designate the elevation of the sea surface above a mean level, and $\partial z/\partial x = z_x$, $\partial z/\partial y = z_y$ (fig. 1; see sec. **3**) the corresponding slope components. In the following computations a Gaussian isotropic distribution of the slope components will be adopted as a suitable first approximation (sec. **11**):

$$p(z_x,z_y) = (\pi\sigma^2)^{-1} \exp\left[-(z_x^2 + z_y^2)/\sigma^2\right] .$$

The mean square slope regardless of direction, $\sigma^2 = \langle z_x^2 + z_y^2 \rangle$, increases with the "masthead" wind speed in m. sec.$^{-1}$, W, according to

$$\sigma^2 = .003 + 5.12 \times 10^{-3} W \pm .004 .$$

In the presence of a slick this value is reduced by a factor of 2 or 3.

In adopting the isotropic Gaussian distribution function the results are simplified at the cost of omitting certain effects of wind directionality, for it has been found (sec. **11**) that the mean square up/downwind slope component exceeds the cross-wind component, and that the up/downwind distribution is skewed.

17. Glitter as Seen from Beneath the Surface

A diver looking upward to the sea surface views a glitter pattern that differs substantially from the pattern as seen from above. The differences are illustrated in figure 20, and the reader is referred to the legend of this figure. The upper part of the figure is based on the theory of the *reflected* glitter (sec. **4**). The theory for refracted glitter (lower part of figure) is developed along similar lines in the following sections.

The principal differences between the reflected and refracted glitter patterns are:

1. The reflected glitter pattern is larger and less luminous than the refracted pattern.

2. The reflected pattern shrinks and becomes more luminous as the sun sets; the reverse holds for the refracted pattern.

3. The reflected and refracted patterns both move toward the horizon with the setting sun, but the reflected pattern moves almost twice as fast.

In a general way these conclusions are in agreement with what has been observed. However, at ordinary diving depths the luminescence varies considerably with the passage of individual waves, whereas the patterns described here correspond to suitable time exposures. The fluctuations diminish with increasing depth, so that at a depth of 1,000 feet, for example, the observed pattern would resemble the computed pattern rather closely, were it not for the effect of absorption (which we have ignored) and scattering.

Whitecaps have been neglected. At low sun elevation the effects of multiple scattering and wave shadowing introduce a serious error into the calculation, and the angular dimension of the sun as compared to the reflected pattern should also be taken into account. All constants were computed for an isotropic slope distribution. Under actual conditions the most probable slope is not zero, but a few degrees, and its azimuth of ascent is directed downwind. The result is an upwind displacement of the bright core of the glitter from the computed position.

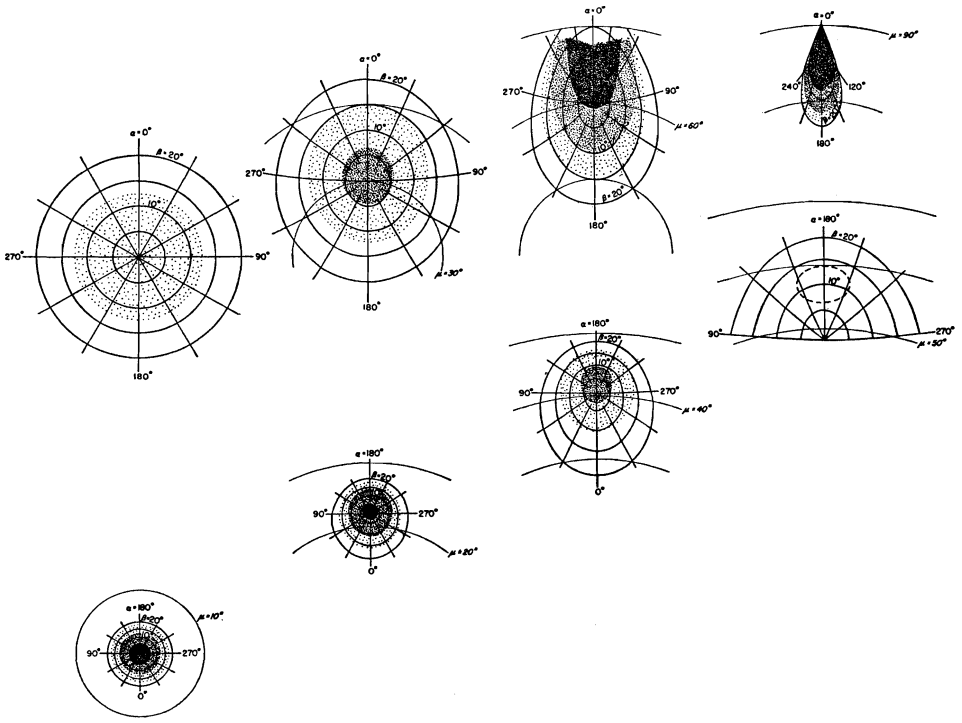

Fig. 20. The glitter patterns for a Beaufort 4 wind (W = 7 m. sec.$^{-1}$, σ = 0.2) as seen from above the surface (upper four) and from beneath (lower four). The patterns from left to right are drawn for solar zenith angles of 0° (sun at zenith), 30°, 60°, and 90° (sun at horizon). Each pattern is drawn with reference to the polar coördinates μ, the observer's zenith angle, and ν, the azimuth relative to the sun (see fig. 21). The value μ = 0° designates a point on the surface directly beneath or above the observer; the horizon is at μ = 90°. The circular arcs in the upper patterns are drawn for μ = 30°, 60°, 90°, in the lower patterns for 10°, 20°, . . . , 70°. The μ-scale in the lower figure is 2.5 times the scale in the upper figures. For each diagram the radial α-lines give the azimuth of ascent, and the quasi-elliptical β-lines the tilt required for the occurrence of a high light (fig. 21). Shadings indicate surface luminosity. The values in units of the sun's luminosity are as follows:

Shading	*None*	*Light*	*Medium*	*Heavy*
Upper figures (parts per million)	.66	.66–3.3	3.3–16.6	16.6
Lower figures (parts per thousand)	.25	.25–1.3	1.3–6.6	6.6

17.1 *The geometry of refraction.*—The following derivation follows closely the derivation of the geometry of reflection in section **3**; therefore an abbreviated account will be given. All angles are defined in figure 21. The azimuth of ascent, α, and the tilt, β, are related to the slope components z_x,z_y, according to

$$z_x = \sin\alpha \tan\beta\,, \qquad z_y = \cos\alpha \tan\beta\,.$$

According to the law of refraction, a unit vector along the incident ray minus a vector along the refracted ray of length equal to the refractive index n equals a vector normal to the refracting surface. This vector equation has the components

$$\left.\begin{aligned} -\sin\psi - n\sin\mu\cos\nu &= -k\cos\alpha\sin\beta\,, \\ -n\sin\mu\sin\nu &= -k\sin\alpha\sin\beta\,, \\ -\cos\psi + n\cos\mu &= k\cos\beta\,. \end{aligned}\right\} \qquad \textbf{(17.1–1)}$$

The factor k may be found by eliminating μ and ν. This yields

$$k = n \cos \omega_r - \cos \omega \,, \tag{17.1–2}$$

where

$$\cos \omega = \cos \beta \cos \psi - \cos \alpha \sin \beta \sin \psi, \qquad \sin \omega_r = n^{-1} \sin \omega \,. \tag{17.1–3}$$

It can be verified that ω and ω_r are the angles of incidence and refraction (angle measured between ray and surface normal). Solving (17.1–1) for μ and ν yields the "grid" relations

$$\left.\begin{aligned} \cos \mu &= n^{-1} (\cos \psi + k \cos \beta) \\ \cot \nu &= \cot \alpha - (k \sin \alpha \sin \beta)^{-1} \sin \psi \,. \end{aligned}\right\} \tag{17.1–4}$$

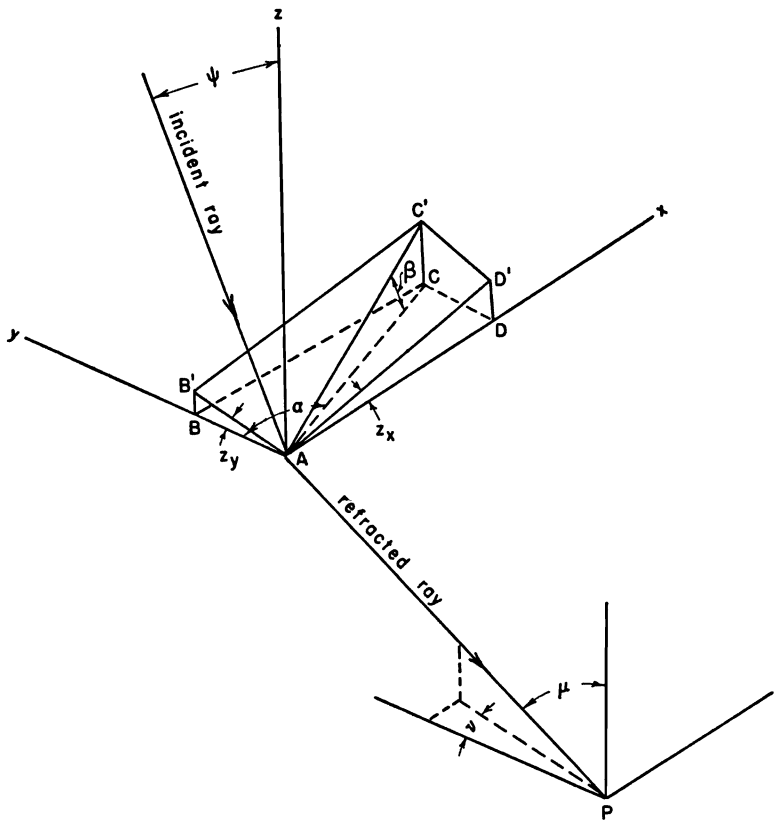

Fig. 21. The coördinate system is centered at the sea surface, with the z-axis vertically upward and the y-axis horizontal and toward the sun. The incident ray is refracted at A toward the observer at P, where it forms an angle μ with the vertical, and an azimuth ν to the right of the sun. Points $A\ B\ C\ D$ define a horizontal plane through A, and $A\ B'\ C'\ D'$ a plane tangent to the sea surface. The tilt β is measured in the direction AC of the steepest ascent, and this direction makes an angle α to the right of the sun.

Any point on the sea surface can be characterized by its zenith angle μ and direction ν. In the eight diagrams of figure 20 the angles μ, ν are represented by polar coördinates; μ is the radial distance and ν the angular coördinate. On these polar diagrams curves of constant $\alpha(\mu,\nu)$ and $\beta(\mu,\nu)$ for various solar zenith angles ψ have been drawn according to the grid relations. An observer looking upward to a point μ,ν at the surface will see the facets highlighted that have the slope given by these curves.

The index of refraction, n, depends on the wave length of light. In the subsequent calculations we have used $n = 1.34$, corresponding to yellow light.

17.2 *Surface radiance.*—This section corresponds to section **4** for the case of reflection. Individual high lights form distorted images of the sun. According to a general law of optics, the radiance (power per unit solid angle per unit area normal to the beam) radiated by an image in a medium of refractive index n is (n^2) times the radiance of the object (in open space) reduced by any transmission losses of the optical system. Accordingly, the radiance within a high light is $B' = n^2\tau B$ where τ is the transmission of the sea surface and B is the radiance of the surface of the sun. According to Fresnel's formula for unpolarized light, $\tau = 1 - \rho$, where ρ is the reflectivity (**4.3**–1). The *total* power radiated per unit solid angle by the entire high light is therefore $J = B'\Delta_s$ where Δ_s is the area of the high light projected normal to the line of sight. Designating the horizontally projected area of the high light by Δ_h, this becomes

$$J = n^2\tau B\Delta_h \sec\beta\cos\omega\,. \qquad (\mathbf{17.2}\text{–}1)$$

The highlighted areas of the sea surface are those for which the sea surface has the appropriate tilt and azimuth of ascent to satisfy (**17.1**–4) within a small "tolerance" which allows for the fact that rays may originate at any point on the sun's face. This imposes limits on the permitted variation of α,β, or alternatively z_x,z_y, within the high light. It may be shown that the area on the z_x,z_y-plane corresponding to the permitted variation of slopes within a high light is

$$\delta z_x\,\delta z_y = \pi\epsilon^2 k^{-2}\cos\omega\sec^3\beta\,, \qquad (\mathbf{17.2}\text{–}2)$$

where $\pi\epsilon^2$ is the solid angle subtended by the sun. The solid angle subtended by a high light is assumed small compared to the angle subtended by the sun. The highlighted areas are of the order of 0.1 mm.^{2} so that this assumption holds except within a few centimeters of the sea surface. In addition, the angular size of the sun is assumed to be small compared to the angular dimensions of the glitter pattern. This assumption fails for low sun and small slopes.

The fraction of the (horizontally projected) sea surface having slope components within the required limits $z_x \pm \frac{1}{2}\,\delta z_x$, $z_y \pm \frac{1}{2}\,\delta z_y$ is

$$p(z_x,z_y)\,\delta z_x\,\delta z_y\,,$$

where p is the probability distribution of slopes. Hence the average power radiated by all high lights within a horizontal unit area of sea surface is $p\,\delta z_x\,\delta z_y\,J$. The average radiance N of the sea surface in the line of sight (power per unit solid angle per

unit area *normal* to the beam) is this value multiplied by sec μ. Substituting from (**17.2**–1) and (**17.2**–2) yields

$$N = n^2 \tau H k^{-2} p \sec^4 \beta \sec \omega_r \cos \omega \sec \mu . \qquad (\mathbf{17.2}\text{–}3)$$

Here we have replaced $\pi\epsilon^2 B$ by H, the irradiance received at the sea surface from the sun. As a check on this formula, we note that with $n = -1$ (**17.1**–2, –3) and (**17.2**–3) yield $\omega = \omega_r$ (corresponding to reflection) and $N = \frac{1}{4} \tau H p \sec^4 \beta \sec \mu$ in conformity with (**4.2**–4) except for replacement of reflectivity ρ by transmission τ.

The simplest computation is for a point directly above the observer ($\mu = 0$) with the sun at the zenith, $\psi = 0$. Under these conditions

$$N_o = \left(\frac{n}{n-1}\right)^2 \left[1 - \left(\frac{n-1}{n+1}\right)^2\right] H\, p(0,0) .$$

For the observer directly *above* this point, the *reflected* radiance under similar circumstances obtained by setting $\beta = z_x = z_y = 0$, $\mu = 0$, $\rho = \left(\frac{n-1}{n+1}\right)^2$ in (**4.2**–4) equals

$$N_o' = \frac{1}{4}\left(\frac{n-1}{n+1}\right)^2 H\, p(0,0) .$$

The ratio of refracted to reflected radiance is

$$\frac{N_o}{N_o'} = 4\left(\frac{n}{n-1}\right)^2 \left[\left(\frac{n+1}{n-1}\right)^2 - 1\right] \approx 3000 .$$

The radiance from a perfectly diffusing surface (one that scatters uniformly into a solid angle 2π) is H/π.

18. Reflection of Direct Sunlight from a Rough Sea Surface

The reflection of direct sunlight is an important factor in the energy budget of the ocean. Estimates based on reflection from a flat water surface are in error because the average coefficient of reflection for a rough surface differs from that for a flat surface. The difference becomes appreciable for low solar elevations.

First we consider the reflection by facets whose slopes lie within the limits $z_x \pm \frac{1}{2}\,\delta z_x$, $z_y \pm \frac{1}{2}\,\delta z_y$. Their (horizontally projected) area within a unit area A (fig. 22) is, on the average, $p(z_x,z_y)\,\delta z_x\,\delta z_y$. The actual (tilted) area is $\sec\beta\; p\;\delta z_x\;\delta z_y$. The projected area normal to the incoming rays from the sun is $\cos\omega \sec\beta\; p\;\delta z_x\;\delta z_y$. The radiant flux intercepted is $H \cos\omega \sec\beta\; p\;\delta z_x\;\delta z_y$. The reflected flux is

$$H\,\rho(\omega) \cos\omega \sec\beta\; p\;\delta z_x\;\delta z_y , \qquad (\mathbf{18}\text{–}1)$$

where $\rho(\omega)$ is given by Fresnel's formula (**4.3**–1). It is assumed that the incident light is not polarized, and is reflected only once.

Equation (**18**–1) gives the reflected flux associated with slopes within the limit $z_x \pm \frac{1}{2}\delta z_x$, $z_y \pm \frac{1}{2}\delta z_y$. The total reflected flux per unit area of sea surface is then

$$H \iint \rho(\omega) \cos\omega \sec\beta \, p \, \delta z_x \, \delta z_y \,, \tag{18–2}$$

with the integration extending over all slopes exposed to the sun.

The radiant flux incident upon the unit area is $H \cos\psi$, where ψ is the sun's zenith angle. Consequently the fraction reflected, i.e., the *albedo*, is

$$R = \sec\psi \iint \rho(\omega) \cos\omega \sec\beta \, p \, dz_x \, dz_y \,. \tag{18–3}$$

For the special case of a level surface, all contributions to the integral occur at $z_x = z_y = \beta = 0$, $\omega = \psi$, so that $R = \rho(\omega)$.

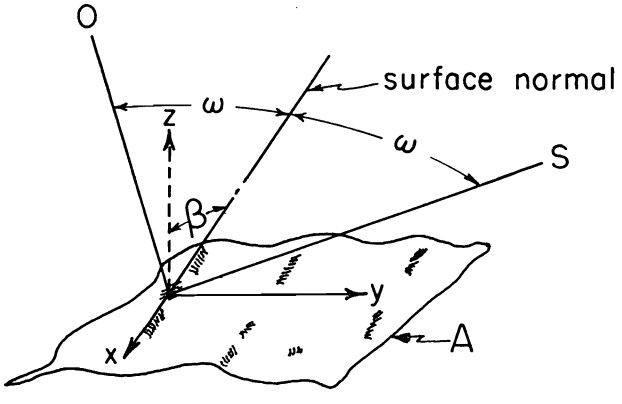

Fig. 22. "*A*" is a unit area of sea surface. The shaded portions indicate all points where the slopes lie within designated limits $z_x \pm \frac{1}{2}\delta z_x$, $z_y \pm \frac{1}{2}\delta z_y$. The average tilt in the shaded areas is β, where $\tan^2\beta = z_x^2 + z_y^2$. The y-axis is drawn away from the sun. Incident rays from the sun at O are reflected toward S. In the discussion of skylight (sec. **19**) the direction of rays is reversed. Incident rays from the sky at S are reflected toward the observer at O. In *both* cases the angle of the incident ray with the z-axis is designated by ψ, and of the reflected ray by μ.

In the general use, one may use the law of reflection in the form (fig. 22)

$$\cos\omega = \cos\beta \, (\cos\psi + z_y \sin\psi) \,. \tag{18–4}$$

The quantities $F(\omega) = \rho(\omega)\cos\omega$ and $\sec\beta = (1 + z_x^2 + z_y^2)^{\frac{1}{2}}$ may now be expanded in Taylor's series in z_x, z_y around the values $z_x = z_y = 0$ for which $\beta = 0$, $\omega = \psi$. This yields

$$R = \rho(\psi) \iint (1 + az_y + bz_y^2 + cz_x^2 + \cdots) \, p \, dz_x \, dz_y \tag{18–5}$$

where

$$a = -F'/F \,, \qquad b = \tfrac{1}{2} + \tfrac{1}{2} F''/F \,, \qquad c = \tfrac{1}{2} + \tfrac{1}{2}(F'/F)\cot\psi \,. \tag{18–6}$$

The functions F, $F' = dF/d\omega$, $F'' = d^2F/d\omega^2$ are evaluated at $\omega = \psi$.

If all slopes are less in magnitude than $90° - \psi$, then the sea surface is everywhere exposed to the sun and the limits are $\pm \infty$. In this case

$$R = \rho(\psi)(1 + b\langle z_y^2\rangle + c\,\langle z_x^2\rangle + \cdots), \tag{18–7}$$

where $\langle z_y\rangle = \int\int z_y\, p\, dz_x\, dz_y$ is zero, because the mean sea level is horizontal. To the present approximation the albedo depends only on the components of mean square slope along the sun's azimuth and normal to it; it does not depend on the form of $p(z_x,z_y)$. For the isotropic case, $\langle z_x^2\rangle = \langle z_y^2\rangle = \frac{1}{2}\sigma^2$, and

$$R = \rho(\psi)[1 + f(\psi)\sigma^2], \tag{18–8}$$

where

$$f(\psi) = \tfrac{1}{2}(b + c) = \tfrac{1}{2} + \tfrac{1}{4}\,(F'/F)\cot\psi + \tfrac{1}{4}F''/F \tag{18–9}$$

is the "roughness" function plotted in figure 23. Some difficulties arise when ψ is large, and these will now be considered.

Large negative slopes in the component z_y are shadowed if they exceed $\cot\psi$. One may allow for this "first order" hiding by setting the limits $(-\cot\psi)$ to ∞ for z_y (but to $\pm\infty$ for z_x). This is equivalent to the limits 0 to 90° in the angle of incidence, ω. Because some additional slopes are hidden, the computed value of R will be somewhat too large for large ψ, but the evaluation of the "second order" hiding

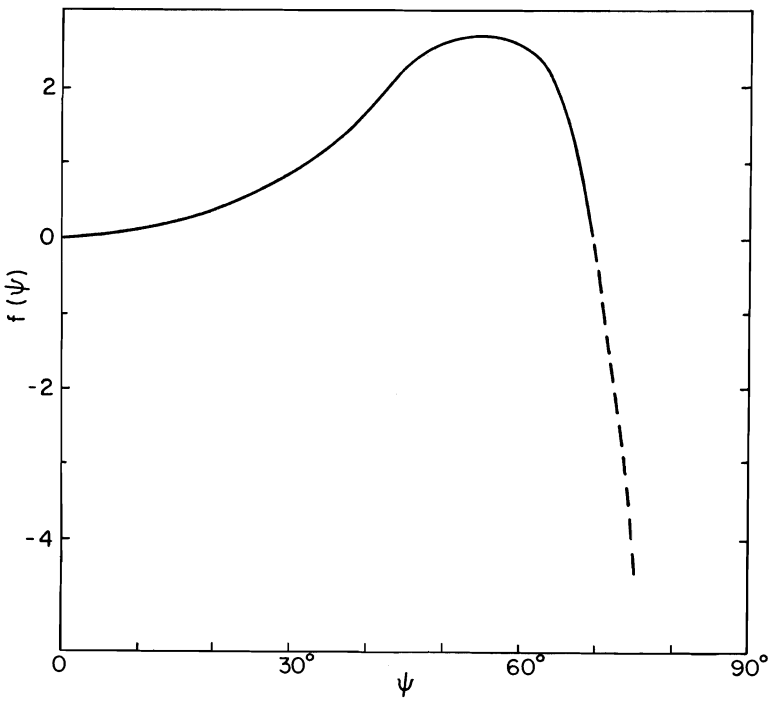

Fig. 23. The roughness function $f(\psi)$ as defined in (18–9). In the dashed portion near the horizon the function is not strictly applicable because of shadowing and multiple reflection.

involves information on the spectrum of ocean waves, and in the absence of such information the calculation must be restricted to the first order hiding.

The integration now yields

$$R = \rho(\psi)\left\{\tfrac{1}{2}[1 + I(k)] + \tfrac{1}{2}\pi^{-\frac{1}{2}}\, a\, \sigma\, e^{-k^2}\right.$$

$$\left. + \tfrac{1}{2}\, b\sigma^2[1 + I(k) - 2\pi^{-\frac{1}{2}}\, k\, e^{-k^2}] + \tfrac{1}{4}\, c\sigma^2[1 + I(k)] + \cdots\right\}, \qquad \textbf{(18–10)}$$

where

$$k = \sigma^{-1} \cot \psi \qquad \textbf{(18–11)}$$

and $I(k) = 2\pi^{-\frac{1}{2}} \int_0^k e^{-t^2}\, dt$ is the error integral. The present approximation is adequate for large values of the dimensionless parameter k. For *very* large values (**18**–10) converges on (**18**–8).

So far multiple reflections have been neglected. If the reflected ray goes toward a point *beneath* the horizon, then certainly there must be at least one further reflection. The condition for this "first order" multiple reflection is that z_y be negative and exceed $\frac{1}{2} \cot \psi\ (1 - \tan^2 \beta)$ in magnitude. The product of coefficients of reflection of all but the first reflection is unknown but must lie between unity and zero. In the first extreme, multiple reflections would not alter R, and (**18**–10) is correct as it stands. In the latter extreme case, the integration with respect to z_y in (**18**–5) is between the limits $-\frac{1}{2} \cot \psi\ (1 - \tan^2 \beta)$ and $+\infty$. These can be replaced by the limits $-\frac{1}{2} \cot \psi$ and $+\infty$ because of the heavy discrimination of the exponential factor in $p(z_x,z_y)$ against contributions from large β. The limits on z_x remain $\pm\infty$. The result of this integration is again (**18**–10), but with k now designated by

$$k = \tfrac{1}{2}\sigma^{-1} \cot \psi \qquad \textbf{(18–12)}$$

rather than the quantity in (**18**–11).

Figure 24 shows the average reflectivity of the sea surface bracketed by these two expressions as compared with the reflectivity of a flat surface. At high sun elevation, the albedo of the rough surface is slightly larger; for $\psi = 40°$ the values are 2.5 per cent for the smooth surface, and 2.7 per cent for the rough surface. At low sun elevation increasing roughness leads to a marked decrease in albedo. The only conclusion of oceanographic consequence seems to be that in summer substantially more energy must penetrate the open stretches of the Arctic Ocean than had previously been estimated, and that the amount of this additional energy depends on the wind speed.

19. Reflection of Diffused Light from a Rough Surface

The radiance of the sky is due to scattering of sunlight and reflected "earth light" by air molecules (Rayleigh scattering), dust, haze, clouds, etc. This varies in a complicated and rather unpredictable way over the sky dome. The three cases illustrated in figure 25 will be considered:

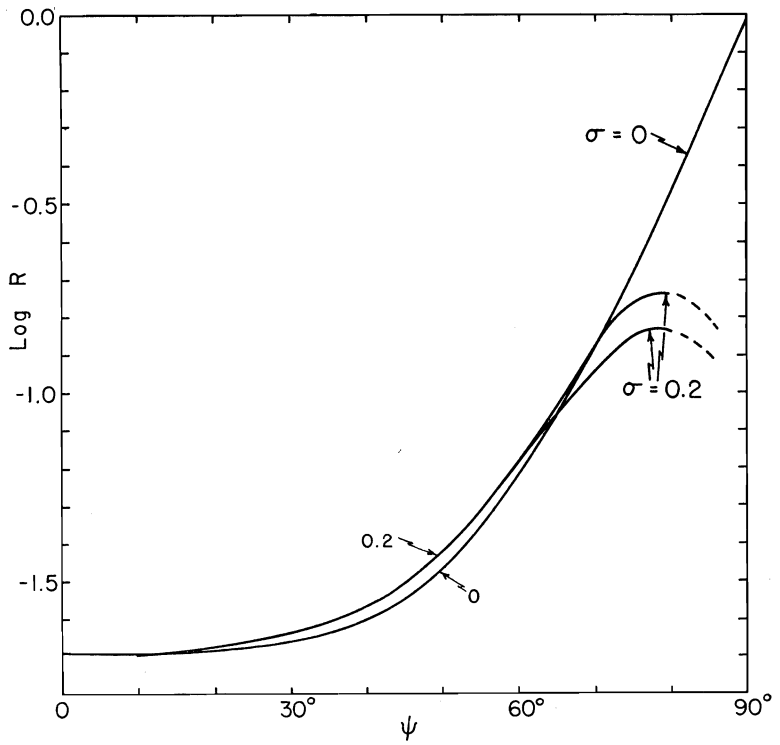

Fig. 24. Reflection of solar radiation from a flat surface ($\sigma = 0$) and a surface roughened by a Beaufort 4 wind ($\sigma = 0.2$). The albedo R varies from .02 for a zenith sun ($\psi = 0°$) to unity for the sun at the horizon ($\psi = 90°$) on a flat sea surface. For a rough surface, shadowing and multiple reflections become important factors when the sun is low. The lower and upper branches of the curve marked $\sigma = 0.2$ represent two assumptions regarding the effect of multiple reflection. True values are expected to lie between the indicated limits.

(*a*) a clear tropical sky, at Bocaiuva, Brazil, from measurements by Richardson and Hulburt (1949); these observations were made at an elevation of 2,200 feet; the sky radiance at sea level would be slightly different; (*b*) a uniform sky dome; (*c*) a completely overcast sky, whose radiance can be approximated by the empirical formula of Moon and Spencer (1942),

$$N_s(\psi) = \tfrac{1}{3} N_s(0)(1 + 2\cos\psi)\,. \qquad (\mathbf{19}\text{–}1)$$

To simplify subsequent calculations, the radiance of the sky will be assumed to depend only on the zenith angle ψ. This already holds for sky conditions (*b*) and (*c*), but even for the Bocaiuva sky the radiance depends largely on zenith angle. Accordingly, the increased radiance near the sun has been ignored and the calculations are based on the observed radiance along an azimuth 90° from the azimuth of the sun. In the following calculations unpolarized skylight will also be assumed. Effectively we write $(N_{s||} + N_{s\perp})(\rho_{||} + \rho_\perp)$ (or $N_s\rho$) in our notation for the reflected radiance instead of $N_{s||}\rho_{||} + N_{s\perp}\rho_\perp$. Here $||$, $\perp$ refer to polarization in the plane of incidence, and normal to it, respectively. Actually there is considerable polarization for a clear sky, and the polarization is a function of the azimuth relative to the sun.

The derivation is similar to that in the preceding section. The rays in figure 22 (sec. **18**) are reversed, with ψ and μ again designating the zenith angles of the incident and reflected rays. The radiant flux from a segment of sky S reflected by the unit area A toward the observer O is, in place of (**18**–1),

$$N_s \, \rho(\omega) \cos \omega \sec \beta \, p \, \delta z_x \, \delta z_y ,$$

where N_s is the radiance of the sky (power per unit solid angle per unit area normal to the beam). Summing the flux for all *visible* slopes yields the total reflected flux from the unit area A toward the observer O,

$$\iint N_s \, \rho(\omega) \cos \omega \sec \beta \, p \, \delta z_x \, \delta z_y . \qquad (\mathbf{19}\text{–}2)$$

The radiance of the sea surface in the observer's line of sight (intensity per unit area normal to the beam) is found by dividing by cos μ:

$$N = \sec \mu \iint N_s \, \rho(\omega) \cos \omega \sec \beta \, p \, dz_x \, dz_y . \qquad (\mathbf{19}\text{–}3)$$

For the special condition of a uniform sky dome, N_s is constant, and the expression

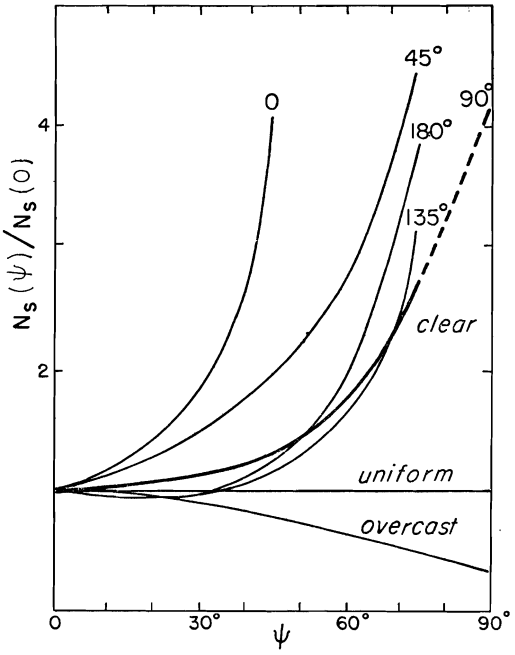

Fig. 25. The radiance of the sky, $N_s(\psi)$, divided by the radiance at the zenith, $N_s(0)$, as function of the zenith angle ψ. The curves for the clear sky are based on observation at Bocaiuva, Brazil, for the sun at $\psi = 60°$. They are drawn for indicated azimuths relative to the sun. Computations are based on the heavy curve marked 90°. The radiance for the overcast sky is based on the empirical law (**19**–1), and applies to all azimuths.

for (N/N_s) is identical with that for R in section **18**. The preceding remarks on integration limits are applicable, and the results given in (**18**–5) to (**18**–12) and in figures 23 and 24 (sec. **18**) can be applied directly.

For conditions in which sky radiance depends on the zenith angle ψ (and ψ only), we must generalize the procedure in section **18**. Writing the law of reflection in the form (fig. 22)

$$\cos\psi = \cos^2\beta[(1 - \tan^2\beta)\cos\mu + 2z_y \sin\mu], \qquad (\mathbf{19}\text{–}4)$$

and again expanding in Taylor's series, lead to the integrals in section **18** with R now denoting $N(\mu)/N_s(\psi)$ and a, b, c replaced by

$$\left.\begin{aligned} a_s &= -F'/F - 2N_s'/N_s\,, \\ b_s &= \tfrac{1}{2} + \tfrac{1}{2}F''/F + 2(N_s'/N_s)(F'/F) + 2N_s''/N_s\,, \\ c_s &= \tfrac{1}{2} + \tfrac{1}{2}(F'/F)\cot\mu + 2(N_s'/N_s)\cot\mu\,. \end{aligned}\right\} \qquad (\mathbf{19}\text{–}5)$$

Figure 26 shows the results for the two sky conditions illustrated in figure 25. Directly beneath the observer ($\mu = 0°$) the rough sea may be brighter or dimmer than a smooth sea depending on the condition of the sky. A rough sea contrasts with a flat surface most markedly near the horizon, where the rough sea appears darker. If the sea were absolutely flat, then the radiance of the sea surface just beneath the horizon would equal the radiance of the sky just above it—there would be no visible horizon.

The albedo of the sea surface exposed to skylight is the ratio of reflected to incident flux. The reflected intensity from a unit area is $N(\mu)\cos\mu$—compare (**18**–2) and (**18**–3)—and the total reflected flux is $2\pi\int_o^{\frac{1}{2}\pi} N(\mu)\cos\mu\sin\mu\,d\mu$. Similarly, the total incident flux is $2\pi\int_o^{\frac{1}{2}\pi} N_s(\psi)\cos\psi\sin\psi\,d\psi$. Hence the albedo is given by

$$R = \int_o^{\frac{1}{2}\pi} N(\mu)\sin 2\mu\,d\mu \Big/ \int_o^{\frac{1}{2}\pi} N_s(\psi)\sin 2\psi\,d\psi\,. \qquad (\mathbf{19}\text{–}6)$$

TABLE 3

ALBEDO OF SEA TO SKYLIGHT

Sky	Sea	
	Smooth (σ=0)	Rough (σ=0.2)
Clear	.100	.071 – .088
Uniform	.066	.050 – .055
Overcast	.052	.043 – .044

The albedo has been evaluated numerically for a smooth and a rough sea surface for each of the three sky conditions shown in figure 25. In the case of the rough surface the integration was carried out along both branches of the curve $\sigma = 0.2$ in figure 26; the correct values are believed to lie within the indicated limits. Compared to a flat sea the albedo is reduced by about 20 per cent in the presence of a Beaufort

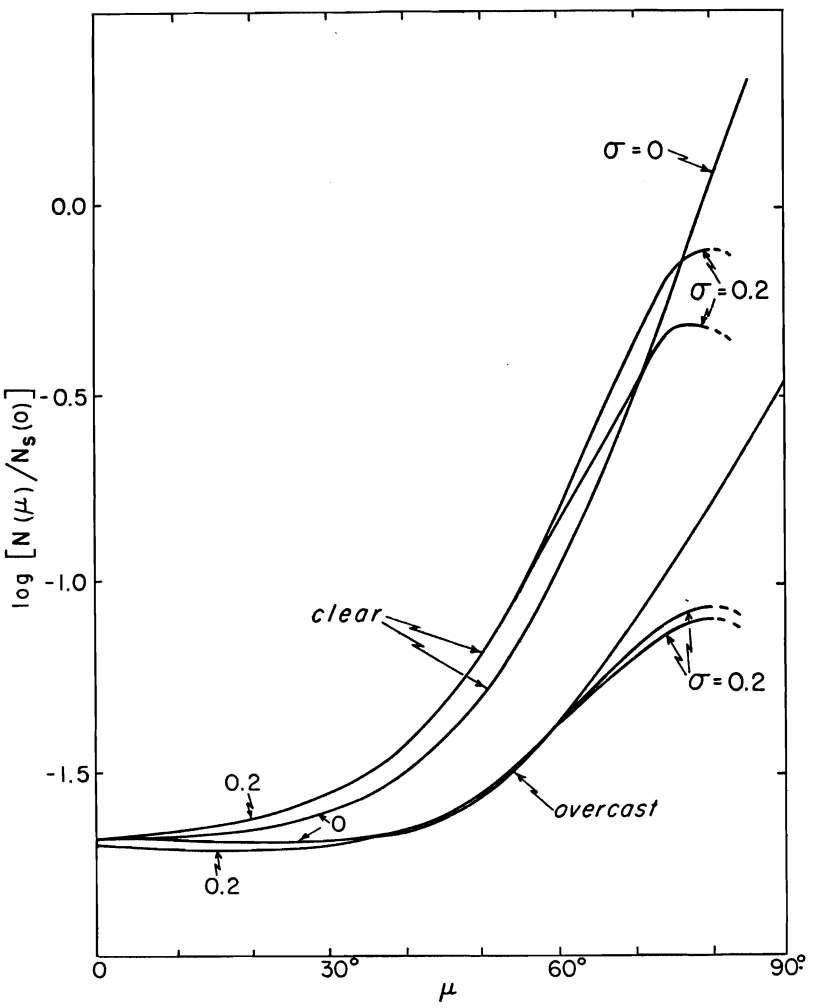

Fig. 26. The radiance of the sea surface, $N(\mu)$, divided by the sky radiance at the zenith, $N_s(0)$, as a function of the vertical angle μ. The curves are computed for a flat ($\sigma = 0$) and rough ($\sigma = 0.2$) surface for two of the sky conditions illustrated in the preceding figure. The two branches for the curves marked $\sigma = 0.2$ again indicate the upper and lower limits inherent in (**18**–11) and (**18**–12).

4 wind, because of the hiding of effectively reflecting slopes and subsequent darkening of the sea surface near the horizon.

For the uniform sky, Schmidt (1915) had previously obtained a theoretical value of 0.17. Measurements by Neiburger (1948) and Burt (1953) under an overcast sky gave only 0.10. Burt subsequently noticed that Schmidt had omitted cosine terms in his flux integration. The correct integration already carried out by Judd (1942) gave a value of 0.066. Whereas initially the theoretical value had been too high, now it was too low, and the discrepancy was almost as bad. The values in table 3 show that allowance for surface roughness does not help. The explanation seems to be the one offered by Neiburger (1954), namely, a reflection from bubbles and particles in the water in addition to the reflection at the surface. The average reflection due to

internal scattering, measured by Powell and Clarke (1936), is 0.03, and this brings observation and theory into reasonable accord. The measurements of background radiation (sec. **5**) also indicate that the scattered intensity can be an appreciable fraction of the reflected intensity.

Burt (1954) has calculated the albedo of the rough sea surface to direct sunlight and diffused light by methods similar to ours. There are, however, two important differences. Burt made no allowance for multiple reflections and he allowed for shadowing by assuming the same distribution of slopes in the shadowed and unshadowed areas. For very low sun elevations he obtains 100 per cent effective reflectivity regardless of surface roughness, whereas our approximation indicates a lowering of reflectivity which increases in magnitude with increasing roughness. Applied to the reflection of skylight, Burt's result implies that there would be no contrast at the horizon; actually, the sea is darker than the sky, particularly on windy days. Fortunately the albedo to skylight is not markedly affected by any of these assumptions. For $\sigma = 0.2$ Burt obtains $R = .058$ (clear sky) and .048 (overcast), compared to our values of .050 − .055 (clear) and .043 − .045 (overcast).

20. Visibility of Slicks

A slick lying *within* the sun's glitter pattern has a larger luminosity near the glitter center and a smaller luminosity near the outer edges than the uncontaminated water surface (pl. 12). This is because of the reduction of r.m.s. slope σ, resulting in an increased probability of low slopes (glitter center) and decreased probability of high slopes (outer edges). The visibility of thin (natural) slicks *outside* the sun's glitter can be discussed with reference to figure 26 (sec. **19**). To an observer looking steeply downward, the slick (small μ) contrasts with uncontaminated water, appearing dark under a clear sky and light under an overcast sky. Near the horizon the slick is always light. The contrast required for the visibility of large slicks is of the order of 2 per cent ($\sim$0.01 on the logarithmic scale in fig. 26), and adequate contrast for visibility may be expected even when the winds are light. In searching for thin slicks one should concentrate on an area well toward the horizon.

The situation is different for freshly spread slicks of mineral oil. The presence of interference colors demonstrates a thickness larger than a wave length of light. According to section **4.3**, the reflection coefficient is appreciably greater than that of clear water. For light oil, the index of refraction is about 1.45 and the reflectivity of the surface is 1.6, 1.3, 1.0 times greater than clean water for angles of incidence 30°, 60°, and 90°.

These coefficients have been taken into account in drawing figure 27. The visibility of thick (artificial) slicks can be estimated by comparison with figure 26. Suppose the oily smooth surface (fig. 27, $\sigma = 0$) is compared with the uncontaminated rough surface (fig. 26, $\sigma = 0.2$). The slicks are brighter, and the contrast is most marked directly beneath the observer ($\mu = 0°$).

Some remarkable photographs of slick bands have been published by Ewing (1950). The surprising aspect is that these bands are due to *internal* waves. These are made visible by a curious chain of events: The orbital motion of the internal waves converges at the troughs, and the oils resulting from biological activity are squeezed into a surface-active film under tension, as shown by Ewing. This film by

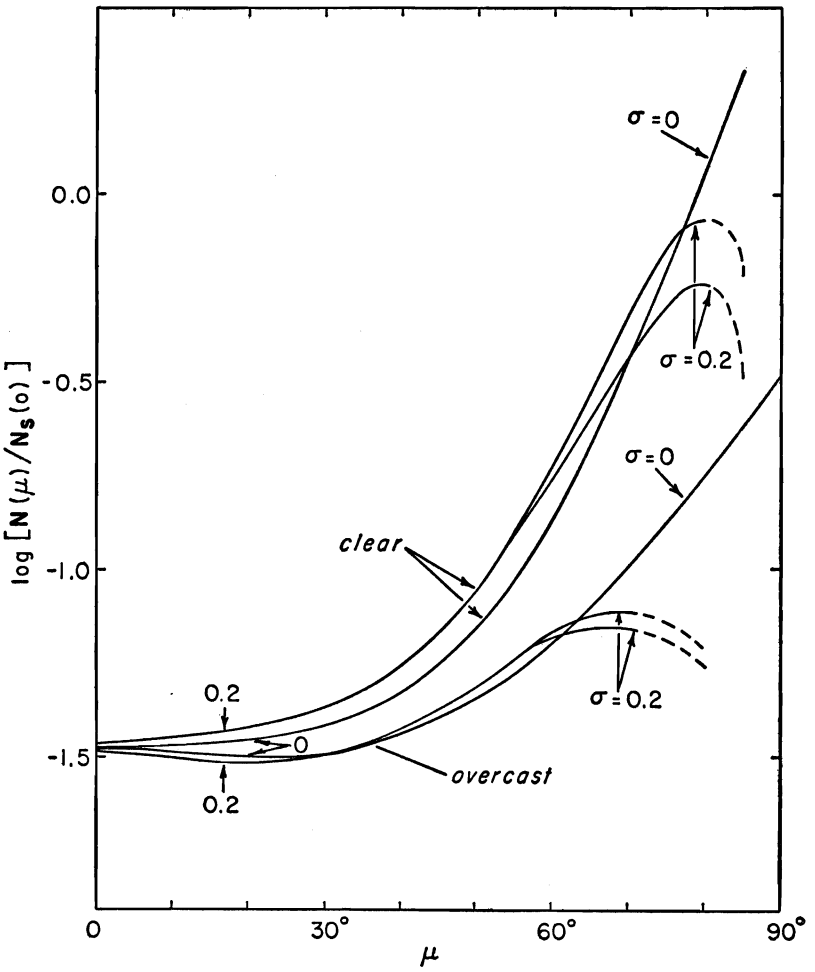

Fig. 27. The radiance of a slick sea surface (see legend of fig. 26).

virtue of its resistance to stretching imposes a horizontally quasi-rigid boundary against which short wavelets generated by local winds dissipate most of their energy. The resulting decrease in mean square slope affects the average reflectivity and also the segment of sky that is mirrored in the trough zones; both these effects produce a brightness contrast between the slicks and the surrounding ruffled water. It seems virtually impossible to predict the devious means by which nature chooses to reveal herself to the astute observer!

LITERATURE CITED

BURT, W. V.
1953. A note on the reflection of diffuse radiation by the sea surface. Trans. Am. Geophys. Union, vol. 34, pp. 199–200.
1954. Albedo over wind roughened water. J. Met., vol. 11, pp. 283–290.
CHANDRASEKHAR, S.
1943. Stochastic problems in physics and astronomy. Rev. Mod. Phy., vol. 15, pp. 1–89.
COX, C., and W. MUNK
1954*a*. Measurement of the roughness of the sea surface from photographs of the sun's glitter. J. Opt. Soc. Am., vol. 44, pp. 838–850.
1954*b*. Statistics of the sea surface derived from sun glitter. J. Mar. Res., vol. 13, pp. 198-227.
1955. Some problems in optical oceanography. J. Mar. Res., vol. 14, pp. 63–78.
CRAMER, H.
1946. Mathematical methods of statistics. Princeton, Princeton University Press. 575 pp.
DARBYSHIRE, J.
1952. The generation of waves by wind. Proc. Roy. Soc. A., vol. 215, pp. 299–328.
DUNTLEY, S. Q.
1950. The visibility of submerged objects. I: Optical effects of water waves. Visibility Laboratory, Mass. Inst. Tech. Report, or U.S. Office of Naval Research Report No. N5 ori-07831.
ECKART, C.
1946. The sea surface and its effect on the reflection of sound and light. Univ. of Cal. Div. of War Research No. M407 (unpublished).
1953. The scattering of sound from the sea surface. J. Acoust. Soc. Am., vol. 25, pp. 566–570.
EWING, G.
1950. Slicks, surface films, and internal waves. J. Mar. Res., vol. 9, pp. 161–187.
HENNICKER, J. C.
1949. The depth of the surface zone of a liquid. Rev. Mod. Phy., vol. 21, pp. 322–341.
HULBURT, E. O.
1934. The polarization of light at sea. J. Opt. Soc. Am., vol. 24, pp. 35–42.
JUDD, D. B.
1942. Fresnel reflection of diffusely incident light. J. Res. Nat. Bur. Standards, Research Paper 1504, vol. 29, pp. 329–332.
LAMB, H.
1945. Hydrodynamics. 6th ed. New York, Dover. 738 pp.
LONGUET-HIGGINS, M. S.
1950. A theory of the origin of microseisms. Phil. Trans., vol. 243, pp. 1–35.
MINNAERT, M.
1940. Light and colour in the upper air. London, Bell and Sons. 362 pp.
1942. The reflection of light in rippled surfaces. Physica, vol. 9, pp. 925–935.
MOON, P., and D. E. SPENCER
1942. Illumination from a nonuniform sky. Trans. Ill. Eng., pp. 707–726.
NEIBURGER, M.
1948. The reflection of diffuse radiation by the sea surface. Trans. Am. Geophys. Union, vol. 29, pp. 647–652.
1954. A note on the reflection of diffuse radiation by the sea surface. Trans. Am. Geophys. Union, vol. 35, pp. 729–732.
NEUMANN, G.
1953. On ocean wave spectra and a new way of forecasting wind generated sea. Technical Memoirs, Beach Erosion Board.
PIERSON, W. J., JR., and W. MARKS
1952. The power spectrum analysis of ocean wave records. Trans. Am. Geophys. Union, vol. 33, pp. 834–844.

POWELL, W. M., and G. L. CLARKE
1936. The reflection and absorption of daylight at the surface of the ocean. J. Opt. Soc. Am., vol. 26, pp. 111–120.
RICE, S. O.
1944. Mathematical analysis of random noise. Bell System Tech. J., vol. 23, pp. 282–332.
RICHARDSON, R. A., and E. O. HULBURT
1949. Sky brightness measurements near Bocaiuva, Brazil. J. Geophys. Res., vol. 54, pp. 215–227.
SCHMIDT, W.
1915. Strahlung und Verdunstung an freien Wasserflächen; ein Beitrag zum Warmeshaushalt des Weltmeers und zum Wasserhaushalt der Erde. Ann. d. Hydrogr. u. Mar. Meteor., vol. 43,pp. 111–124.
SCHOOLEY, A. H.
1954. A simple optical method for measuring the statistical distribution of water surface slopes. J. Opt. Soc. Am., vol. 44, pp. 37–40.
SHULEIKIN, V. V.
1941. Fizika Moria (Physics of the sea). Moscow, Izdatelstvo Akad. Nauk. USSR. 833 pp.
SPOONER, J.
1822. Sur la lumière des ondes de la mer. Corresp. Astronomique du Baron de Zach, vol. 6, p. 331.
TITCHMARSH, E. C.
1937. Introduction to the theory of Fourier integrals. Oxford, The Clarendon Press. 390 pp.
VAN WIERINGEN, J. S.
1947. Reflection of light by rippled water surfaces. Proc. Kon. Ned. Akad. Van Wetenschappen, vol. 50, pp. 952–958.
WIENER, N.
1933. The Fourier integral and certain of its applications. London, Cambridge University Press. 201 pp.

PLATES

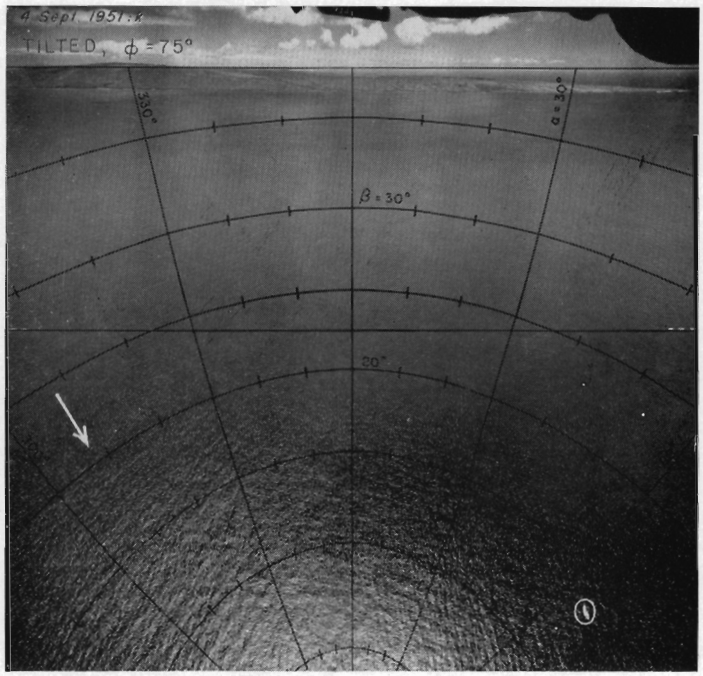

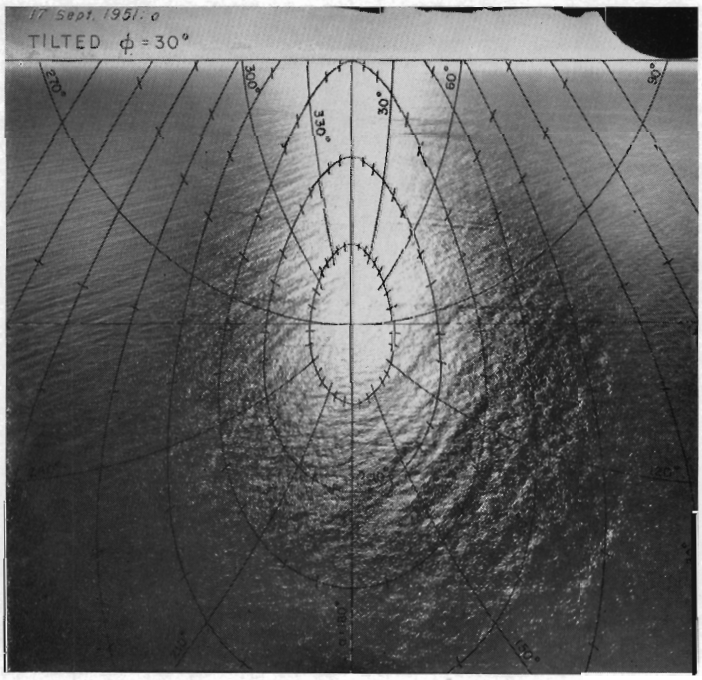

The glitter pattern at solar elevations of ϕ = 75°, 50°, 30°, and 10°. Wind speed was approximately 4 m. sec.$^{-1}$ The superimposed grids consist of lines of constant slope azimuth α (radial)

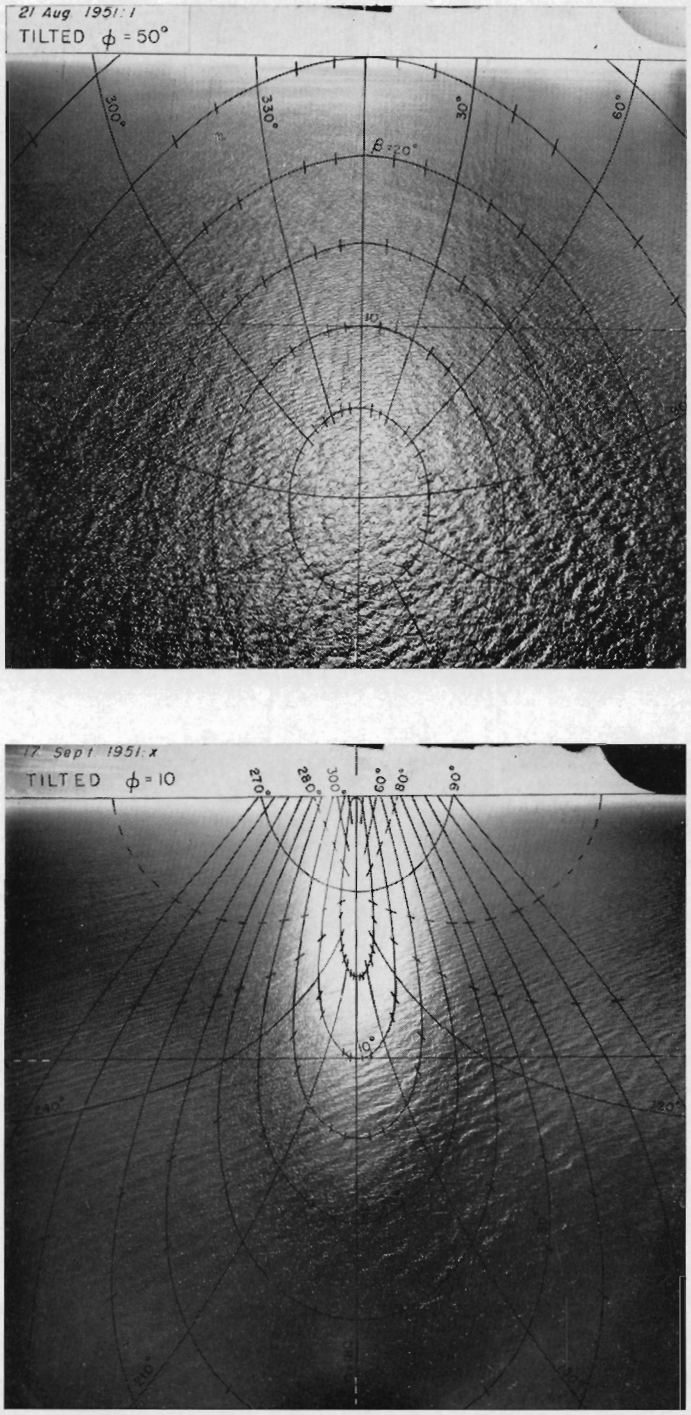

drawn for every 30°, and of constant tilt β (closed) for every 5°. The vessel *Reverie* is encircled in upper left photograph. The white arrow indicates wind direction in this photograph.

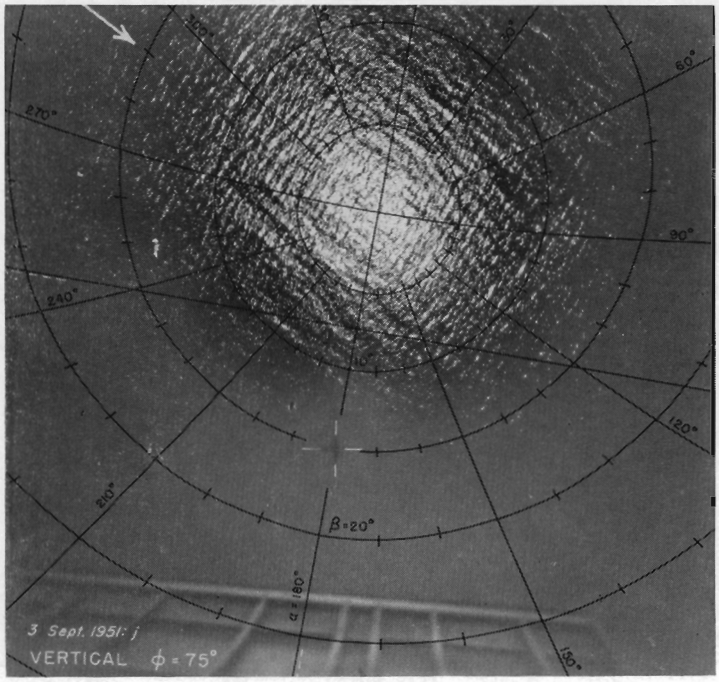

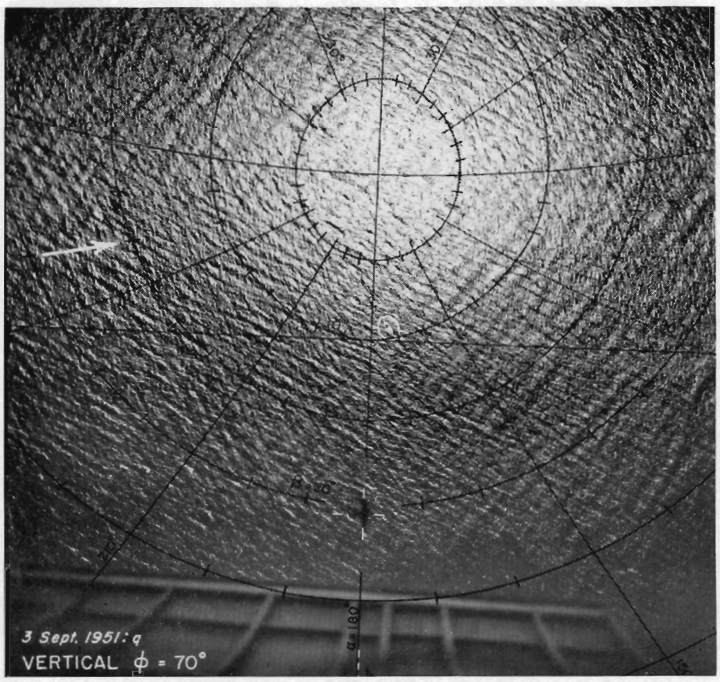

The glitter pattern at wind speeds of 0.7, 3.9, 8.6, and 14 m. sec.$^{-1}$ The plane's shadow can barely be seen along $\alpha = 180$, within the white cross. The grids have been translated and rotated

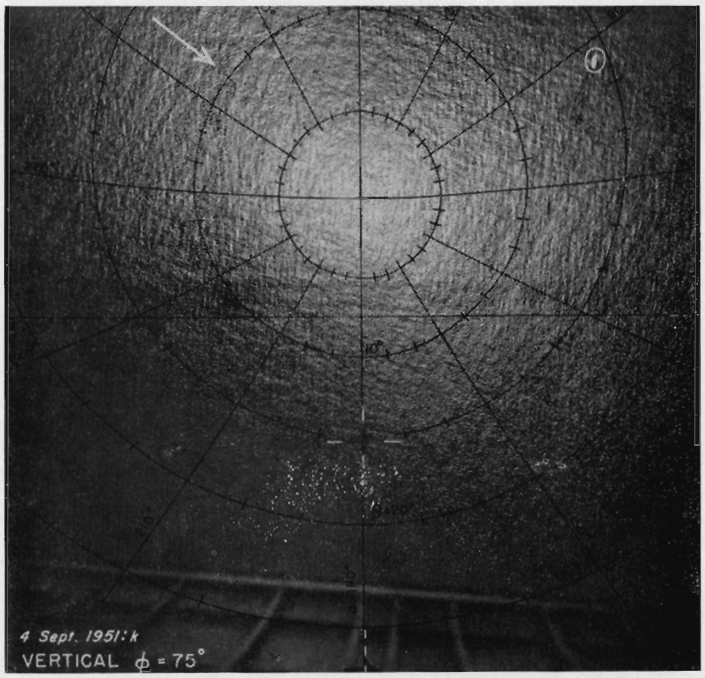

to allow for roll, pitch, and yaw of plane. Large rotation in upper left photograph is due to bad yaw. Notice overlap of 4 Sept. k on plates 10 and 11.

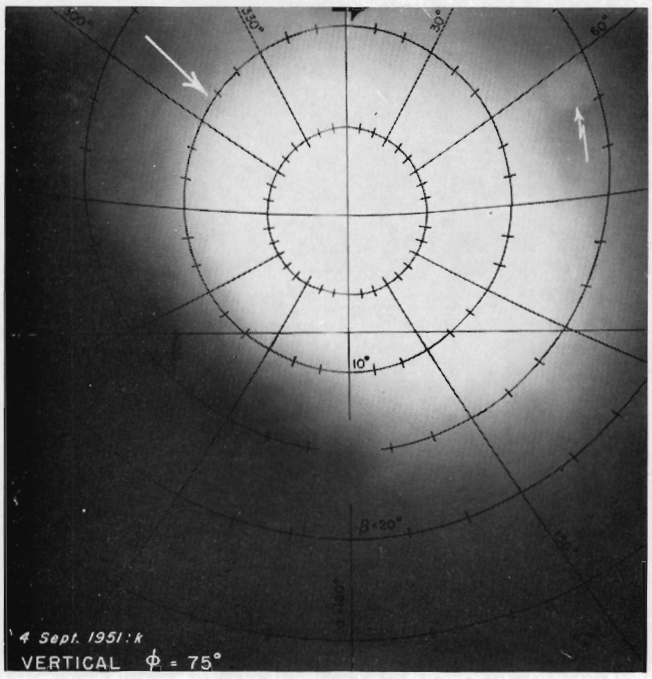

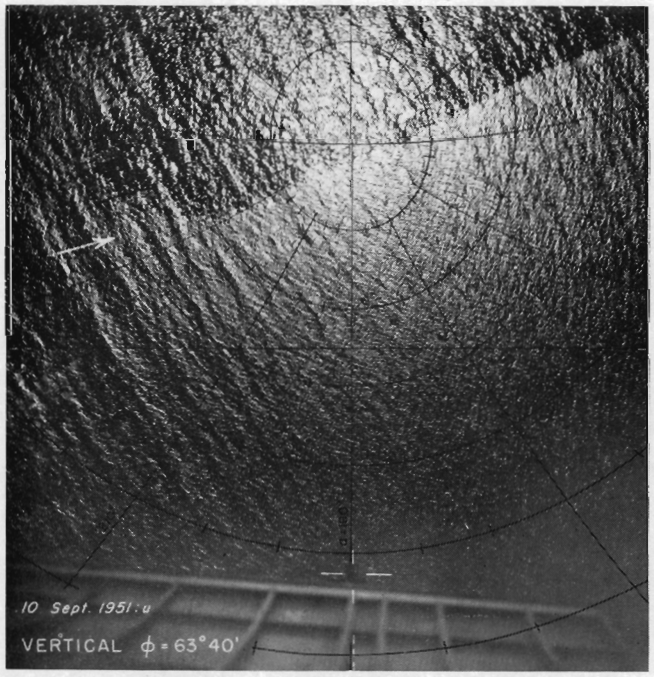

Upper left: Photometric photograph corresponding to image photograph on upper right, plate 11. Light circle due to *Reverie* is indicated by broken arrow. *Upper right*: Natural slick, wind 1.8 m. sec.$^{-1}$ *Lower left and right*: Vertical and tilted photographs of rectangular artificial slick, with near

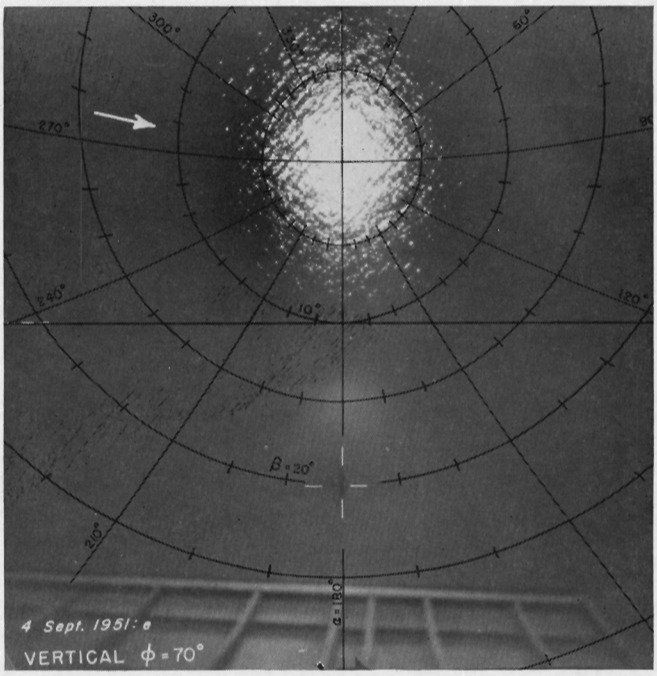

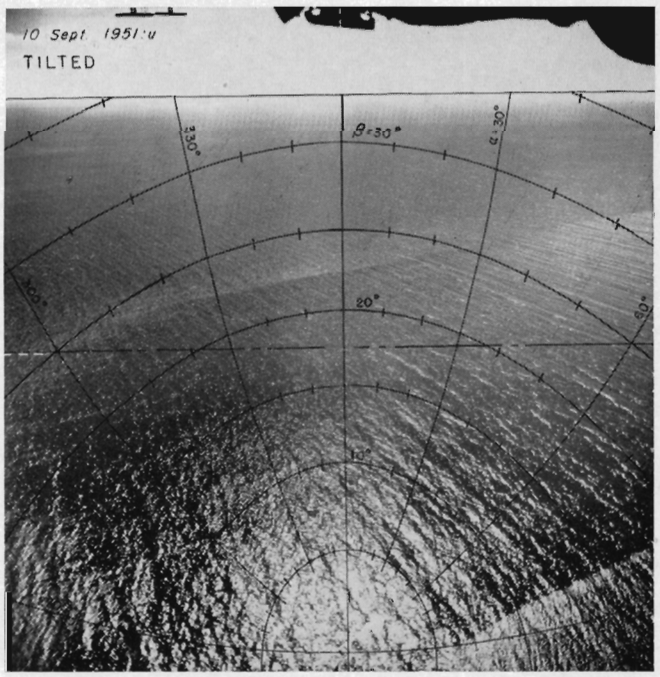

boundary almost through specular point. Brightness of slicked sea surface is reduced for large β and enhanced for small β.